UNIVERSITY OF TECHNOLOGY SYDNEY
Faculty of Mathematical and Physical Sciences

Applied Nanophotonics with Two-Dimensional Materials

by

Ngoc My Hanh DUONG

A Thesis Submitted
in Partial Fulfillment of the
Requirements for the Degree

Doctor of Philosophy

Supervisors:

Professor Milos Toth

Professor Igor Aharonovich

Sydney, Australia

July 2020

Certificate of Authorship/Originality

I certify that the work in this thesis has not been previously submitted for a degree nor has it been submitted as a part of the requirements for other degree except as fully acknowledged within the text.

I also certify that this thesis has been written by me. Any help that I have received in my research and in the preparation of the thesis itself has been fully acknowledged. In addition, I certify that all information sources and literature used are quoted in the thesis.

This research is supported by an Australian Government Research Training Program Scholarship

Signature of Student

Production Note:
Signature removed prior to publication.

Date: 07 July 2020

ABSTRACT

Applied Nanophotonics with Two-Dimensional Materials

by

Ngoc My Hanh DUONG

Silicon semiconductor technology has revolutionized electronics beyond the imagination of pioneering scientists. This technology's rate of progress since 1947 has been enormous, with the number of transistors on a single chip growing from a few thousand in the earliest transistors to more than two billion today. However, there seems to be a limit to the miniaturization of electronics chips, when the size of individual transistors can no longer be reduced, or they become unstable when quantum tunneling starts to kick in at a few atoms limit. Therefore, there is an urgent need to complement Si CMOS technology and to fulfil future computing requirements as well as the need for diversification of applications with new materials. In that context, two-dimensional (2D) materials emerge as a promising alternative. They demonstrate a range of superior optical and electronic properties, which are essential for future optoelectronic applications. In the crystal form, thin layers of these materials are stacked and held together by relatively weak van der Waals forces. Consequently, it is easier to exfoliate and transfer them to a target substrate by a simple tape exfoliation and stamping method. This is a substantial advantage of 2D materials over their three-dimensional (3D) counterparts for incorporation in devices.

2D materials promise a heterogeneous platform that is particularly appealing for on-chip integration, owing to their small footprints and compatibility with semiconductor technology. In this thesis, we investigate the engineering of hexagonal boron nitride (hBN) at the nanoscale to generate single photon emitters in hBN flakes and nanoparticles. Next, we discuss the effort to develop novel nanophotonic platforms

by integrating hBN quantum emitters in dielectric waveguides; we successfully coupled and propagated quantum light in hBN through the waveguides. Finally, we present the work on the incorporation of transition metal dichalcogenide (TMDC) material in a circular Bragg's grating structure to improve the directionality of the emitted photon stream and light extraction efficiency.

Dissertation directed by Professor Milos Toth, Professor Igor Aharonovich
School of Mathematical and Physical Sciences

Dedication

To my loved ones

Acknowledgements

I would like to thank my supervisors Professor Milos Toth and Professor Igor Aharonovich, who have sparked my interest in nano-science and offered me the opportunity to explore the exciting field of nanophotonics. I am grateful to have their guidance and for the freedom in research that I immensely enjoyed. It is because of their endless support, understanding, and patience that I can advance in my research. The experience that I have obtained by working in their group will be of priceless importance for my future career.

I would like to acknowledge the collaborators, and constructive comments I have received from Professor James Edgar, Professor Alexandra Radenovic, Professor Shigeki Takeuchi, and Professor Takeshi Ohshima for the projects in my thesis.

I would like to express my gratitude to academic staffs – Dr. Toan Trong Tran, Dr. Mehran Kianinia, Dr. Alexander Solntsev, Dr. Sejeong Kim, Dr. Zai-quan Xu, Dr. James Bishop, and Dr. Carlo Bradac – who get involved in my research, help me with experiment designs and share their invaluable experience. Without their mentorship, I could not have been able to finish the projects promptly.

Special thanks are due to the technical staff of the Microstructure Analysis Unit (MAU) – Mr. Geoff McCredie, Ms. Katie McBean, Mr. Mark Berkahnand and Mr. Herbert Yuan. They have been providing me induction to the laboratory facility. They are also maintaining, troubleshooting, and upgrading to keep the facilities at their top performances so that I can finish my experiments.

Throughout my education, I was fortunate to have excellent fellow students who have helped me through technical problems and given me useful advice. It has been a great pleasure to know you and work with you guys - Minh Nguyen, Johannes Froech, Alexandra Trycz, Chi Li, Blake Reagan, Tung Huynh, Anh Ly, Thinh Tran,

Noah Mendelson and Connor Stewart.

I would like to extend my gratitude towards the Research Training Program (RTP) scheme from the Department of Education and Training for funding my stipend.

Finally, I am grateful for the constant love and support that I have been receiving from my brother Nhut Minh, my parents Nhut Long and Ngoc Thuy and my family in Vietnam. My parents have developed my interest in science and technology. They are my greatest inspiration and my first teachers. Especially, I am grateful for love, devotion and support from my beloved husband Tien Thong, who has always put up with me and be by my side through difficult times and helped me reach my dream. This thesis is for them.

Ngoc My Hanh Duong

Sydney, Australia, 2020.

List of Publications

Journal Papers

Articles with results included in this thesis

J-1. **NGOC MY DUONG, H.**, NGUYEN, M. A. P., KIANINIA, M., OHSHIMA, T., ABE, H., WATANABE, K., TANIGUCHI, T., EDGAR, J. H., AHARONOVICH, I. & TOTH, M. 2018. Effects of High-Energy Electron Irradiation on Quantum Emitters in Hexagonal Boron Nitride. *ACS Applied Materials & Interfaces*, 10, 24886-24891.

J-2. **NGOC MY DUONG, H.**, XU, Z.-Q., KIANINIA, M., SU, R., LIU, Z., KIM, S., BRADAC, C., TRAN, T. T., WAN, Y., LI, L.-J., SOLNTSEV, A., LIU, J. & AHARONOVICH, I. 2018. Enhanced Emission from WSe2 Monolayers Coupled to Circular Bragg Gratings. *ACS Photonics*, 5, 3950-3955.

J-3. KIM, S., **NGOC MY DUONG, H.**, NGUYEN, M., LU, T.-J., KIANINIA, M., MENDELSON, N., SOLNTSEV, A., BRADAC, C., ENGLUND, D. R. & AHARONOVICH, I. 2019. Integrated on Chip Platform with Quantum Emitters in Layered Materials. *Advanced Optical Materials*, 7, 1901132.

J-4. **NGOC MY DUONG, H.**, GLUSHKOV, E., CHERNEV, A., NAVIKAS, V., COMTET, J., NGUYEN, M. A. P., TOTH, M., RADENOVIC, A., TRAN, T. T. & AHARONOVICH, I. 2019. Facile Production of Hexagonal Boron Nitride Nanoparticles by Cryogenic Exfoliation. *Nano Letters*, 19, 5417-5422.

Articles with results not included in this thesis

J-5. **NGOC MY DUONG, H.**, REGAN, B., TOTH, M., AHARONOVICH, I. & DAWES, J. 2019b. A Random Laser Based on Hybrid Fluorescent Dye and

Diamond Nanoneedles. *physica status solidi (RRL) – Rapid Research Letters*, 13, 1800513.

J-6. BISHOP, J., FRONZI, M., ELBADAWI, C., NIKAM, V., PRITCHARD, J., FRÖCH, J. E., **NGOC MY DUONG, H.**, FORD, M. J., AHARONOVICH, I., LOBO, C. J. & TOTH, M. 2018. Deterministic Nanopatterning of Diamond Using Electron Beams. *ACS Nano*, 12, 2873-2882.

Contents

List of Figures

Abbreviation

2D: Two-Dimensional

3D: Three-Dimensional

TMDCs - Transition Metal Dichalcgenides

hBN - Hexagonal Boron Nitride

WSe_2 - Tungsten Diselenide

PL - Photoluminescence

RWA: Rotating Wave Approximation

SPE: Single Photon Emitter

CVD: Chemical Vapour Deposition

PMMA - Polymethyl Metacrylate

CW - Continuous Wave

AFM - Atomic Force Microscopy

ZPL - Zero Phonon Line

FWHM - Full Width at Half Maximum

PDMS - Polydimethylsiloxane

QD - Quantum Dot

FDTD - Finite-Difference Time-Domain

NA - Numerical Aperture

PSB - Phonon SideBand

AlN - Aluminum Nitride

FFT - Fast Fourier Transform

HBT - Hanbury Brown and Twiss

EMCCD - Electron Multipying CCD

SMLM - Single Molecules Localization Microscopy

CBG - Circular Bragg Grating

Si_3N_4 - Circular Bragg Grating

SEM - Scanning Electron Microscopy

CL - Cathodoluminescence

Nomenclature and Notation

Capital letters denote matrices.

Lower-case alphabets denote column vectors.

k denotes modulus of the wave vector.

E is the electric field.

h is the Planck constant $n \times n$.

v denote the photon velocity.

$\vec{\epsilon}$ defines the direction of the electric field.

V is the quantization volume.

$\hbar\omega_0$ is the energy difference between the two levels.

F_P denote the Purcell factor.

Q is the quality factor.

V_0 is the mode volume.

I(σ^+) and I(σ^-) are right and left circularly polarized emission, respectively.

ρ denote the degree of PL polarization.

Chapter 1

Introduction

1.1 Background

Nanophotonics has emerged as a booming research area and is anticipated to have a particularly disruptive impact over the next decade. This area of nanoscience is defined as the science and engineering of light-matter interactions at the nanoscale. However, photons (individual packets of light) do not interact with each other. This means that the designs and structural properties of nanostructures control the interaction with light through their interaction with electrons. By that definition, different materials, compounds, and their nanostructured combinations give rise to novel ways of controlling and manipulating photons. The development of nanophotonics will benefit many other disciplines and technologies such as quantum optics, telecommunications, data storage, medical therapies and diagnostics, and nanoscale imaging. Recently, two-dimensional (2D) materials have received much attention from the research community, owing to their outstanding electronic, optical, mechanical, and chemical properties. The successful isolation of graphene in the past decade has led to tremendous growth in the number of 2D material families, leading to the inclusion of insulating hexagonal boron nitride (hBN) and transition metal dichalcogenides (TMDCs). Until recently, graphene was the most widely studied material among 2D material families, owing to its zero-bandgap nature at the limit of 2D quantum confinement. Graphene has enabled many exciting applications in nanophotonics and nanoelectronics. However, its semi-metallic nature hinders the realization of efficient light-emitting devices. Monolayer TMDCs are direct-

bandgap semiconductors that demonstrate strong excitonic effects when interacting with light. These exceptional optical properties support their use in many optoelectronic applications, including atomic-scale single photon emitters, transistors, novel light-emitting diodes, and so on. However, the light-extraction efficiency of monolayer TMDCs is much lower than expected for direct-bandgap semiconductors, mainly due to the subnanometer light matter interaction length, thus prohibiting them from extensive usage in applications. Therefore, novel methods of enhancing light-emitting efficiency and improving other emission properties are required.

Another emerging 2D material is hBN, whose honeycomb lattice structure resembles that of graphene. hBN possesses a large bandgap of 6 eV, making it an outstanding insulator for 2D material-based devices; it helps to enhance the electronic and optoelectronic performance of these devices. hBN was also found to host polarized and ultra-bright single photon emission at room temperature. A single photon emitter is considered a central building block for many scalable quantum technologies. Since these emitters are embedded in thin layers, they ease the transfer process and improve the spatial matching of quantum light sources to optical cavities or waveguides, compared to other solid-state hosted emitters. Despite the enormous potential, as far as we know, the interaction of quantum emitters in hBN with nanophotonic structures is still not widely studied.

1.2 Research Objectives

The plethora of 2D materials and their heterostructures, together with the availability of photonics platforms for light-matter interaction enhancement, promise enormous scientific discoveries and nanophotonics technologies across a wide range of the electromagnetic spectrum. In that context, this thesis presents the development of novel nanophotonics platforms to further broaden the current knowledge of light-matter interaction of quantum emitters in hBN. This study also explores a

new strategy to enhance light extraction from monolayer TMDCs and further improve the optically induced valley contrast readout in WSe_2. Following this logic, chapter 2 consists of a brief introduction to the discovery of new classes of 2D materials and the physical and optical properties of 2D materials. In chapter 3, we present a new approach to generating quantum emitters using high-energy electron beam irradiation (MeV). This method can create quantum emitters on flat land, which is important for the integration of emitters with nanophotonics structures. Following this, chapter 4 analyses single photon emitters in hBN coupled with AlN photonic waveguides. This heterogeneous system is an appealing platform for use as an on-chip quantum light source essential for various applications in quantum communication and information processing. In chapter 5, we present hBN nanoparticles produced by cryogenic mediated exfoliation. The photophysical and photodynamic properties, together with chemical and thermal stability, make them a promising candidate for a range of applications in super-resolution imaging, sensing, and drug delivery. Chapter 6 introduces a practical strategy to improve the light-matter interaction of 2D TMDC materials by using the circular Bragg's grating structure. In Chapter 7, we summarize the work done and discuss possible future directions and outlooks.

1.3 Thesis Organization

This thesis is organised as follows:

- *Chapter 2*: This chapter presents the introduction and scope of the thesis. It also goes through some background about the definition and classification of single photon sources, 2D materials, the physical and optical properties of hBN, and TMDCs.

- *Chapter 3*: Chapter 3 investigates the generation of single photon emission from hBN by using high energy electron beam irradiation. The optical and photodynamic properties of the generated emitters are also studied. This method offers a promising avenue to deterministically create single photon emitters in hBN, which are useful for various potential quantum applications. Significant portions of this chapter are copied verbatim from the peer-reviewed article "Effects of High-Energy Electron Irradiation on Quantum Emitters in Hexagonal Boron Nitride." Ngoc My Duong, H., et al. (2018). ACS Applied Materials & Interfaces 10(29): 24886-24891 [118].

- *Chapter 4*: This chapter demonstrates the integration of single photon emitters in hBN in dielectric waveguides. The successful coupling of a single photon emitter to the on-chip waveguide is a fundamental step towards the realization of on-chip photonic integrated circuits. Significant portions of this chapter are copied verbatim from the peer-reviewed articles "Integrated on Chip Platform with Quantum Emitters in Layered Materials." Kim, S., et al. (2019). Advanced Optical Materials 7(23): 1901132 [80].

- *Chapter 5*: This chapter introduces the fabrication of hBN nanoparticles using cryogenic mediated exfoliation. Furthermore, we study the photophysical and photodynamic properties of these particles using the Single Molecule Localization Microscopy (SMLM). We figure out that hBN nanoparticles are indeed suitable to be used as labels in biomedical imaging. Significant portions of this chapter are copied verbatim from the peer-reviewedd article "Facile Production of Hexagonal Boron Nitride Nanoparticles by Cryogenic Exfoliation." Duong, N. M. H., et al. (2019). Nano Letters 19(8): 5417-5422 [36].

- *Chapter 6*: The control of directionality and enhancement of light extraction from TMDCs coupled to Circular Braggs Grating structure is explored in this

chapter. The system was tested at cryogenic temperature to understand the temperature dependence photoluminescence properties of TMDCs coupled to the photonic structure. Significant portions of this chapter are copied verbatim from the peer-reviewed articles "Enhanced Emission from WSe2 Monolayers Coupled to Circular Bragg Gratings." Duong, N. M. H., et al. (2018). ACS Photonics 5(10): 3950-3955 [37].

- *Chapter 7*: A brief summary of the thesis contents and its contributions are given in the final chapter. Recommendation for future works is given as well.

Chapter 2

Literature Survey

2.1 Introduction

2.2 Photons and Single Photons

2.2.1 Definition of Photons

Gilbert Lewis [89] invented the term photon in 1926, and the conventional definition of a photon is a quantum of an excited quantised electromagnetic field with an energy E:

$$E = hv \tag{2.1}$$

where h is the Planck's constant and v is the photon velocity. Almost all known optical phenomena of optics can be described using the framework of classical electromagnetism, which means thats light can be described as a classical electromagnetic wave, obeying Maxwell's equation, without any reference to the notion of the photon. Starting in the 1970s, however, a single-photon package or pair of entangled photons was no longer described using a classical model. Single and entangled photons are used to encode, transmit and process information in totally new ways in the domain of quantum information - a central theme in the coming quantum revolution. So do we need to quantise light? The answer is yes.

2.2.2 Quantisation of Electromagnetic Fields

From a non-classical view, a photon is the quantisation of an electromagetic field. An electromagnetic field is composed of an electrical and a magnetic field, which obey Maxwell's equations. Such an electromagnetic field can exist even in the

absence of charges and currents. The approach to quantising the electromagnetic field is described in more detail in reference [108] and [49]. Here is the corresponding Maxwell's equations of radiation in a volume without sources

$$\nabla.E(r,t) = 0 \tag{2.2}$$

$$\nabla.B(r,t) = 0 \tag{2.3}$$

$$\nabla \times B(r,t) = \frac{1}{c^2}.\frac{\partial E}{\partial t} \tag{2.4}$$

$$\nabla \times E(r,t) = -\frac{\partial B}{\partial t} \tag{2.5}$$

To define the field in the volume of interest, we only need to know the field value at the boundary of that volume. The elementary element of Maxwell's equation is called a mode - a field that oscillates at a well-defined frequency. Since it oscillates, it can be quantised as a harmonic oscillator. There are different kinds of modes, but here we will consider the simplest possible mode - a traveling plane wave that describes a freely propagating field. The energy confined in an electromagnetic field written here is a solution of Maxwell's equations given that some conditions are fulfilled:

$$E(r,t) = \overrightarrow{\epsilon}\varepsilon(t)e^{i(k.r)} + c.c \tag{2.6}$$

where k is the modulus of wave vector $\vec{k}$ and *c.c.* means complex conjugate so that the field E is real, $\vec{\epsilon}$ defines the direction of the electric field. The conditions for this field to obey Maxwell's equations are $\vec{\epsilon} \perp \vec{k}$ and $\varepsilon(t) = \varepsilon(0)e^{-i\omega.t}$ with $\omega = c.k$, where ω is the angular frequency at which the amplitude of the field ε oscillates. The ensemble of vector $\vec{k}$ that determines the direction of field propagation and frequency of field with a unit vector $\vec{\epsilon}$ perpendicular to $\vec{k}$, characterises a mode referred to as a polarised travelling monochromatic plane wave. However, the characteristics of the mode $\vec{k}$ and $\vec{\epsilon}$ only determine the structure of the field. One should consider the complex amplitude ε which characterises the state of the field in the mode. The

complex number ε is fully determined by two variables: its real and imaginary parts or its modulus and phase. These variables are denoted as Q and P. Our goal is to prove that they are canonical conjugate variables, so that quantisation will be a consequence. By using Maxwell's fourth equation 2.5 we find that B has a form with the same complex exponential as E:

$$B(r,t) = \frac{i}{\omega^2} k \times \overrightarrow{\epsilon} \frac{d\varepsilon(t)}{dt} e^{i(k.r)} + c.c \tag{2.7}$$

Taking time derivative of 2.7 and using Maxwell's second equation 2.5 we obtain a second-order differential equation for the complex amplitude ε:

$$\frac{d^2\varepsilon(t)}{dt^2} = -\omega^2 \varepsilon(t) \tag{2.8}$$

As we choose the mode travelling along k, the complex amplitude ε describes the state of the field since it allows us to express E as well as B:

$$E(r,t) = \overrightarrow{\epsilon}\varepsilon(0) e^{i(k.r-\omega t)} + c.c \tag{2.9}$$

$$B(r,t) = \frac{k \times \overrightarrow{\epsilon}}{\omega} \varepsilon(t) e^{i(k.r)} + c.c \tag{2.10}$$

The dynamics is given by a first-order differential equation derived from 2.8:

$$\frac{d\varepsilon(t)}{dt} = -i\omega\varepsilon(t) \tag{2.11}$$

As a complex number, E is determined by two real variables; its modulus and its phase or its real and imaginary parts. A normal variable α is introduced:

$$\varepsilon(t) = i\mathcal{E}\alpha(t) \tag{2.12}$$

The evolution of $\alpha(t)$ is obviously the same as the complex amplitude $\varepsilon(t)$

$$\frac{d\alpha(t)}{dt} = -i\omega\alpha(t) \tag{2.13}$$

Real and imaginary parts of $\alpha(t)$ are now introduced and denoted as Q and P:

$$\alpha(t) = \frac{1}{\sqrt{2\hbar}}(Q + iP) \tag{2.14}$$

$$Q = \sqrt{\frac{\hbar}{2}}(\alpha(t) + \alpha^*(t)) \tag{2.15}$$

$$P = -i\sqrt{\frac{\hbar}{2}}(\alpha(t) - \alpha^*(t)) \tag{2.16}$$

The energy of the electromagnetic field knowing the structure of the mode and the amplitude $\varepsilon(t)$ is:

$$H = \frac{\varepsilon_0}{2}\int_0^V d^3r(E^2 + c^2B^2) \tag{2.17}$$

By solving the intergration we obtain:

$$H = 2\varepsilon_0 V[\mathcal{E}^2]|\alpha(t)|^2 \tag{2.18}$$

where V is the quantisation volume. We now make a choice that constant $\mathcal{E} = \sqrt{\frac{\hbar\omega}{2\varepsilon_0 V}}$. The constant $\mathcal{E}$ is called the photon amplitude of a single mode. With this notation, a remarkable expression for energy is established:

$$H = \hbar\omega|\alpha(t)|^2 = \frac{\omega}{2}(Q^2 + P^2) \tag{2.19}$$

where the canonical variables Q and P fulfill the Hamiltonian equations that yield an evolution equation for $\alpha(t)$. Thus,it can be concluded that Q and P are canonically conjugate variables and one can proceed with a canonical quantisation with these two operators with the commutation relation

$$[\hat{Q}, \hat{P}] = i\hbar \tag{2.20}$$

Introduction of ladder operators $\hat{a}$ and $\hat{a\dagger}$ following

$$\hat{a} = \frac{1}{\sqrt{2\hbar}}(\hat{Q} + i\hat{P}); \hat{a}^\dagger = \frac{1}{\sqrt{2\hbar}}(\hat{Q} - i\hat{P}) \tag{2.21}$$

leads to a new representation of the Hamiltonian:

$$\hat{H} = \hbar\omega(\hat{a}^\dagger\hat{a} + \frac{1}{2}) \tag{2.22}$$

It is apparent that the Hamiltonian of quantised electromagnetic fields is equivalent to a quantum mechanical harmonic oscillator [137] and all of its consequences can be applied.

2.2.3 Light-Matter Interaction

In the previous section, the quantised electromagnetic field is described in terms of the vector potential and electric field operators. We now use these operators to attain a complete understanding of quantum mechanics of the coupling between a single light emitter, described by a simplified two-level system with associated dipole moment u and a continuum of light field modes.

Jaynes-Cummings model

A two level system can be described as two states of a spin $\frac{1}{2}$ particle in a magnetic field [173]. Thus, it can be described using the Pauli spin matrices:

$$\hat{\sigma}_x = \begin{pmatrix} 0 & 1 \\ 1 & 0 \end{pmatrix}, \hat{\sigma}_y = \begin{pmatrix} 0 & -i \\ i & 0 \end{pmatrix}, \hat{\sigma}_z = \begin{pmatrix} 1 & 0 \\ 0 & -1 \end{pmatrix} \tag{2.23}$$

, which introduces the canonically conjugated operators $\hat{\sigma}^+$ and $\hat{\sigma}^-$ defined by:

$$\hat{\sigma}^+ = \hat{\sigma}_x + i\hat{\sigma}_y, \hat{\sigma}^- = \hat{\sigma}_x - i\hat{\sigma}_y \tag{2.24}$$

The Hamiltonian equation of the two level syste is given by [173]

$$\hat{H} = \frac{1}{2}\hbar\omega_0\hat{\sigma}_z \tag{2.25}$$

where $\hbar\omega_0$ is the energy difference between the two levels. The interaction between an emitter and a light field is treated as an interaction between a two level system and a quantum mechanical harmonic oscilltor 2.22. The interaction is given by [49]:

$$\hat{H}_I = \hbar\lambda(\hat{\sigma}^+ + \hat{\sigma}^-)(\hat{a} + \hat{a}^\dagger) \tag{2.26}$$

where λ is the coupling constant. When coupled to a light field oscillating at angular frequency ω, we have the Hamiltonian equation:

$$\hat{H} = \frac{1}{2}\hbar\omega_0\hat{\sigma}_z + \hbar\omega\hat{\sigma}_z + \hbar\lambda(\hat{\sigma}^+ + \hat{\sigma}^-)(\hat{a} + \hat{a}^\dagger) \tag{2.27}$$

In the case where the field mode and emitter are near resonance (ω ω_0) the terms containing slowly varying time exponentials will dominate. The so-called Rotating Wave Approximation (RWA) ignores the fast-varying time exponential terms and only keeps the different terms. The interaction in the RWA can be displayed as:

$$\hat{H}_{JC} = \frac{1}{2}\hbar\omega_0\hat{\sigma}_z + \hbar\omega\hat{\sigma}_z + \hbar\lambda(\hat{\sigma}^+\hat{a} + \hat{\sigma}^-\hat{a}^\dagger) \tag{2.28}$$

This model provides the tools for the study of single-photon emission interacting with various configurations.

Quantum Emitter Coupling to a Radiation Continuum

The Jaynes-Cummings mode is applied to describe the coupling of a quantum emitter of frequency ω to a continuum of electromagnetic field modes labelled by variable β with corresponding frequency ω_β. Considering the case of one-dimensiona continuum, for example, a single (transverse) mode waveguide, β will label the longitudinal momentum of the mode, and ω_β is the dispersion curve. Denote β^i as the value of β for which $\omega(\beta^i) = \omega$ and v_g^i which is referred as group velocity of the waveguide, can be expressed as:

$$v_g^i = (\frac{\partial\omega}{\partial\beta})_{\beta=\beta^i} \tag{2.29}$$

The decay rate of an emitter in the waveguide mode can be defined as:

$$k = \sum_i \frac{2\pi}{v_g^i}|C_{\beta^i}|^2 \tag{2.30}$$

where C_{β^i} is the coupling constant between the quantum emitter and mode β. If ω is in the gap of the waveguide mode dispersion, then k becomes zero. This means there are no modes in which the emitter can decay. If ω and dispersion curve cross at one point, the emitter decays at an inverse rate with the group velocity of the waveguide.

$$k = \frac{2\pi}{v_g^*}|C_{\beta^*}|^2 \tag{2.31}$$

Based on equation 2.31, if the waveguide has small group velocity, emitters will decay fast into that mode. This is an example of the Purcell effect - which explains the decay rate of an emitter depends on intrinsic properties of the emitter (e.g., dipole moment) and the electromagnetic field surrounding the emitter - the mode into which emitter decays.

Spontaneous emission in a single-mode cavity: the Purcell effect

Considering a two-level system coupled to a single-mode resonant cavity in the weak coupling regime, the change of spontaneous emission rate is called the Purcell effect, which was first considered by E. M. Purcell in 1946 [130]. The Purcell factor, which compares the decay rate at exact resonance between the atom and the cavity (with quality factor Q and mode volume V_0) to the free space value is defined as:

$$F_P = \frac{W^{cav}}{W^{free}} = \frac{\tau_R^{free}}{\tau_R^{cav}} = \frac{3Q(\lambda/n)^3}{4\pi^2 V_0} \tag{2.32}$$

where λ is the free-space wavelength of the light and n refers to the refractive index of the medium inside the cavity.

The Purcell factor is a convenient parameter to characterise the enhancement effect of a cavity, when the Purcell factor is greater than one, implying that the spontaneous emission rate is enhanced by the environment or cavity effect.Obtaining large Purcell factors requires high Q cavities with small mode volumes. Furthermore, we need to have close spectral matching between the cavity mode and the atomic transition in terms of wavelength and linewidth. We must also ensure that the orientation of the dipole is parallel to the mode field. The emission rate enhancement is related to the large density of states at the cavity mode frequency, while the inhibition of emission when off-resonance is because of the lack of modes into which the atom can emit. Equation 2.32 also indicates that the Purcell factor can be obtained by comparing the lifetime of emission on resonance and off-resonance of

the atom in a cavity.

2.2.4 Photon Statistics

There are three types of photon sources: namely, thermal light (e.g., incandescent light bulb) coherent light (e.g., laser) and single-photon source. A single-photon source is different from a classical light source in terms of photon statistics. Thermal lights follow the super Poissonian distribution where the number of photons or photon pairs produced per pulse can be multiple or vary randomly while coherent light shows a Poissonian distribution. For a given average photon number $\overline{n}$, the probabilities P_n to find n photons in the measurement are:

$$P_n = \begin{cases} \frac{\overline{n}^n}{1+\overline{n}^{n+1}} & \text{for thermal light} \\ e\frac{-\overline{n}\overline{n}^n}{n!} & \text{for coherent light} \\ 0 \text{ for } n \neq \overline{n} & \text{for a number state} \\ 1 \text{ for } n = \overline{n} & \end{cases} \tag{2.33}$$

However, single-photon source presents a non-classical behavior: a sub-Poissonian distribution or photon antibunching characteristic where only one photon is produced at a time. Nevertheless, in reality, a single-photon source will never be perfect and will occasionally emit zero or multiple photons. The photon statistics of thermal light sources and coherent light sources can both be described using classical models. However, there is no-classical derivation available for single photon sources, hence a non-classical approach is necessary. One approach that has been applied to distinguish the photon statistics of a quantum light source is to evaluate the second-order autocorrelation function of the electric field $g^{(2)}(\tau)$. The function is derived as:

$$g^{(2)}(\tau) := \frac{\left\langle : \hat{I}(t)\hat{I}(t+\tau) : \right\rangle}{\left\langle \hat{I}(t) \right\rangle^2} = \frac{\left\langle \hat{a}^\dagger(t)\hat{a}^\dagger(t+\tau)\hat{a}(t+\tau)\hat{a}(t) \right\rangle}{\left\langle \hat{a}^\dagger(t)\hat{a}(t) \right\rangle^2} \tag{2.34}$$

with $\hat{I}(t)$ being the intensity operator, time difference τ, :: indicating normal ordering of the operators, $\langle ... \rangle$ is time averaging.

At time difference $\tau = 0$, equation 2.34 becomes:

$$g^{(2)}(0) = \begin{cases} 2, & \text{for thermal light} \\ 1, & \text{for coherent light} \\ 1 - \frac{1}{n}, & \text{for a n-photon number state} \end{cases} \tag{2.35}$$

This is the criterion to determine the photon source type. It can be interpreted

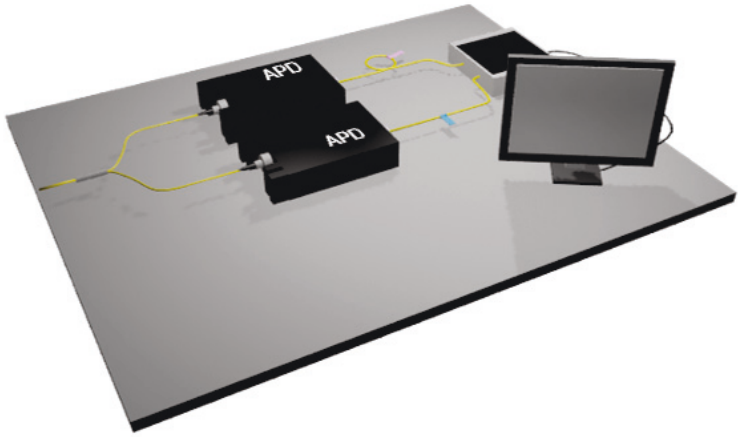

Figure 2.1 : Hanbury Brown and Twiss setup

from this value that if $g^{(2)}(0) > 1$, the probability of detecting a second photon after the first detection event is increased, so-called photon bunching. When $g^{(2)}(0) = 1$, the probability of having a second photon is independent with the time difference

to previous events and if $g^{(2)}(0) < 1$ we have antibunching behaviour, which means the probability of observing another photon coming after the first event, is reduced.

Measurement of $g^{(2)}(\tau)$

Hanbury Brown and Twiss setup [17] is used for the experimental determination of the second-order correlation function $g^{(2)}(\tau)$. Figure 2.1 demonstrates 3D schematic of the setup. In this setup, the beam is split by a 50:50 fibre beam splitter and sent to two avalanche photodiodes (APD). One APD is used to start and the other is used to stop the time measurement with a delay in the electronic signal to compensate the electronic dead time.

2.3 Single Photon Sources

Theoretical aspects of an ideal single-photon source have been considered in section 2.2.4, we now describe some actual material systems that host quantum emitters. As outlined in the introduction section, on-demand single-photon generation has been realised in numerous systems including atoms, ions, molecules, solid-state quantum dots, impurities, and defects in materials. In this section, we overview different solid-state single-photon sources that are promising for applications in quantum cryptography and spin-based computation.

2.3.1 Semiconductor Quantum Dots

A quantum dot is a nanometre-scale structure embedded in a semiconductor. Quantum dots (QDs) are a promising candidate for applications as quantum light sources owing to their capability to emit single [109, 113, 139], indistinguishable [51, 140], and entangled photons [6, 34] on demand. The quantisation of the electromagnetic field in QDs is observed due to their discrete energy levels formed by quantum confinement effects on single-particle wavefunctions. In this structure, the

conduction band electron, valence band holes, or both can be confined tightly in all three dimensions, which give rise to quantum light emissions.

A common type of solid stated QDs is epitaxially grown large bandgap semiconductors consist of tiny regions of smaller bandgap semiconductors. Some semiconductors pairs that can make optically active QDs include InGaAs/GaAs, InP/ GaInP, GaN/AlGaN (iii – v), and CdSe/ ZnS (ii-vi). The most commonly used system for quantum optics experiments is self-assembled InGaAs QDs in GaAs [132]. Owing to their high stability, high brightness, and indistinguishability, QDs have been used to demonstrate entangled photon pairs, which are key elements for many quantum information processing applications such as quantum repeaters [146] and quantum key distribution [2].

However, QDs still suffer from spectral intermittency or spectral blinking as a result of the non-radiative Auger recombination. Also, depending on the growth method, the as-produced QDs will emit a considerable variation in optical emission wavelength due to size fluctuation. The most common approach to cope with this issue is to incorporate a fair amount of QDs into optical devices, and thus to increase the probability that one of them will emit into the resonant wavelength. Therefore, many efforts have been made to develop an appropriate pick and place method to precisely position the QDs [38, 39, 79]. An alternative approach is to identify the location of a QD and then fabricate photonic structures around it [114, 151].

2.3.2 Nitrogen Vacancy Centres in Diamond

Defect centers in diamonds are of great interest among solid-state host systems and nitrogen-vacancy centre (NV centre) is the best-studied color center[86]. NV^0 and negatively charged NV^- are the most common charge states of the NV colour centre, which show the zero phonon line at 575 nm and 637 nm, respectively. The emission from NV centre suffers from a broad phonon sideband, which is indicated by

a small Debye-Waller factor [32] of 0.04 [3]. This factor presents the ratio of the ZPL emission intensity over the phonon sideband intensity. In the NV centre, because of its symmetry, there are two perpendicular dipoles giving rise to the emission. The resulting emission pattern of two dipoles, thus, is less directional than that of one dipole and therefore may lead to reduced coupling efficiency to cavities. We can also tune the emission wavelength of the NV centre to spectrally match with cavity resonances by using the random Stark effect[155].

The NV^- centre also possesses electron spin properties, which make it a promising system to study single spin behavior for applications in quantum computing. It is possible to read the spin of the ground-state of a single-photon emitter even at room temperature [66, 170] through an optical process called optically detected magnetic resonance (ODMR). In this process, we use microwave radiation resonating with ground-state level splitting to manipulate the electronic spin of the colour centere. By comparing the photoluminescence intensities, the spin state can be readout.

NV centre also possesses a long coherence time of 10ns, which is the longest coherence time achieved in a solid-state system [110]. This long coherence time, together with the excellent spin properties, are the major driving forces for the interest of the community in NV centres.

2.3.3 Silicon Vacancy Centres in Diamond

The Si-V centre is formed by replacing two neighboring carbon atoms in the diamond lattice with an interstitial silicon atom. The defect is negatively charged and has a configuration of D3d point group symmetry. There are four transitions between two ground and two excited states located within the diamond bandgap [33]. Two orbital states in the ground and excited states are split by spin-orbit coupling. Having an inversion symmetry with no static electric dipole moment, the SiV centre is insensitive to the Stark effect that causes inhomogeneous electric field

oscillations within the diamond lattice. This factor, together with the weak electron-phonon coupling leads to a narrow ZPL, which is mostly limited by the emission lifetime. The Si-V centre also has a high Debye-Waller factor of 0.7, with 70% of the photons emitted into the ZPL [117]. However, due to the rapid phonon induced mixing between SiV orbital states causes short spin coherence time of $\sim$ 40 ns at cryogenic temperatures [134].

2.3.4 Two-dimensional Materials

Among 2D materials, TMDCs achieved great interest owing to their excellent optical properties. They have also been found to host quantum emitters. In particular, WSe_2 possesses isolated defects that can emit single photons at cryogenic temperatures [59, 82]. The proposed model for these SPEs is the recombination of neutral excitons trapped in the confining the potentials of the defects in the monolayer.

Quantum emitters were also discovered in the layered semiconductor GaSe [161]. These SPEs are photo-stable without any blinking and spectral jump. The nature of the optically active centres in GaSe stems from the local strain fields from lattice deformations, creating confinement to trap the excitons and form a localised exciton and biexciton, when biexcitons decay to exciton resulting a single photon emission [161].

Being a layered material with a wide bandgap, hexagonal boron nitride (hBN) is also a promising candidate for new generation single-photon sources. hBN hosted single-photon emitters have been associated with deep energy level defect states nested within the large bandgap that bears a bright, stable, and broadband SPE at room temperature.

2.4 Hexagonal Boron Nitride Emitters

2.4.1 Single Photon Sources in hBN

hBN is a van der Waals crystal having the structure similar to that of graphene, where the out-of-plane bonds are much weaker than the in plane-bonds [48]. Having a honeycomb structure, hBN is also referred to as white graphene (figure 2.2). hBN

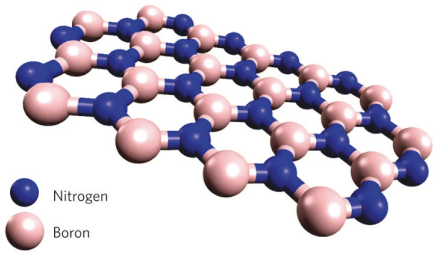

Figure 2.2 : Schematic illustration of hBN crystalline hexagonal structure with alternating boron (pink) and nitrogen (violet) atoms.

has a wide transparent window from ultraviolet to visible due to large bandgap of ∼6 eV. High-quality crystal hBN is used for various electronics devices owing to its superior chemical and thermal stability [85]. Bulk hBN also possess excellent thermal conductivity and bright fluorescent centre in the deep ultraviolet (UV) region combined with band-edge transitions [177].

Recently, our group has demonstrated SPEs in bulk hBN [163] and from localised defects in multilayer and monolayer hBN [163]. Figure 2.3 introduces supreme optical properties of SPEs in hBN. These emitters are optically active even at room temperature with high purity single photon emission and a high proportion of photons emitting into ZPLs. They are thermally stable up to 800K, fully polarised, and exhibit an ultrahigh brightness i.e. 4×10^6 counts/s in the absence of cavities. Recently, an ODMR signal is achieved from optically active defects in neutron irradiated hBN flakes, leading the way to control the electron spin signal [52]. The prop-

erties mentioned above make hBN SPEs particularly appealing for transformational applications in quantum information technology. Several theoretical works based on other ensembles emitting light in the same spectral range suggest the atomic structure of the defect to be substitutional C on a nitrogen site (C_N). [26, 115]

2.4.2 The ZPL Energy and Temperature-dependent Lineshape

SPEs in hBN were first observed with common ZPL wavelength range of $\sim$ 580 - 600 nm, and $V_N N_B$ was the proposed model for the defect [163]. Afterwards, SPEs were categorised in two groups – Group 1 and Group 2 – based on ZPL energies. Emitters in group 1 tend to be broad and asymmetric with ZPL energy ranging from 1.8 to 2.2 eV. In contrast, group 2 emitters have ZPLs with narrower linewidth, and their energy levels are within 1.6 and 1.8 eV [164]. Another study reported that SPEs at 2.16 eV could be excited directly, while group 2 SPE was excited indirectly [69].

The emitters of the two groups were also studied for temperature-dependent PL properties. The natural linewidth of these two SPE groups is 0.352 and 0.148 μeV, respectively, and are independent of temperature, whereas the PL intensity of group 1 SPEs decreases more rapidly compared to that of group 2 emitters [69]. The existence of two types of emitters was also observed in another study [91]. A study on suspended hBN was also performed to mitigate possible effects of substrate on SPE emission, showing emitters in the range 1.77 – 2.25 eV [41]. The line shape of the ZPL is typically fitted with a Lorentzian model. The asymmetric line shape indicates the involvement of multiple processes determining the excited state lifetime. The inhomogeneous broadening of the linewidth is assumed to be a combination of ultra-fast spectral diffusion [149], thermal phonon population [175], or interference from nearby emitters and impurities.

Quantum emitters in h-BN are stable at elevated temperatures [77]. A red-shift

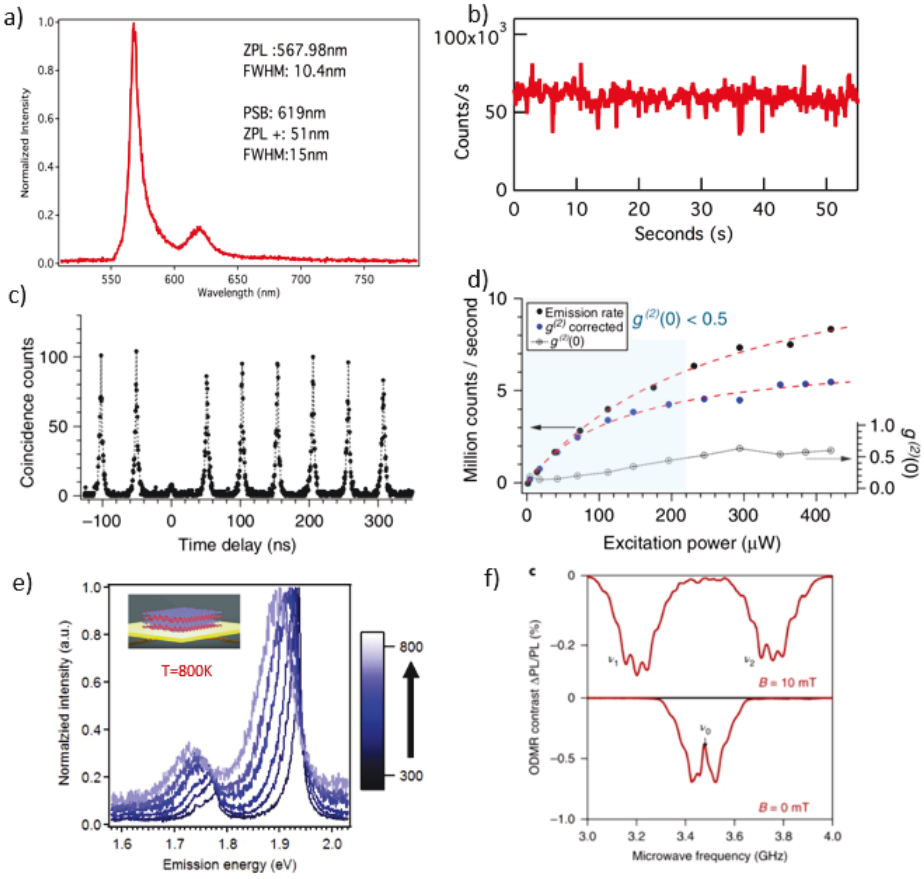

Figure 2.3 : Optical properties of SPEs in hBN. (a) Typical emission from a SPE in hBN with high ratio ZPL PSB [106]; (b) Emission intensity from an emitter acquired as APD counts in 50s [106]; (c) Second-order autocorrelation measurement with pulsed excitation of repetition rate of an emitter, fitting the function yields the value of $g^{(2)}(0) = 0.07$ [54]; (d) Emission rate as a function of excitation power, fitting the function $\mathrm{I} = \mathrm{I}_{inf} * P/(P + P_{sat})$ yield a saturation intensity of 13.8±0.6 x 10^6 counts/s [54]; (e) normalized PL spectra of an emitter by ramping up the temperature from 300 to 800 K with 100 K intervals [77], f) ODMR spectra measured at zero magnetic field (bottom) and at magnetic field $B = 10mT$ [52]. Adapted with permission from: (a) – [106], (b) – [106], (c) – [54], (d) – [54], (e) - [77], (f) - [52]. Copyright (2020) American Chemical Society.

of the ZPL wavelength and linewidth broadening was observed when the temperature was raised to 800K, and this effect is reversible when cooling down to room temperature. The spectral shift in ZPL wavelength upon heating and cooling was due to thermal phonon and lattice contraction. The interaction with low energy acoustic phonons was also proposed to be responsible for the linewidth broadening of the emitter ZPLs in regard to temperature.

2.4.3 SPE Intensities, Quantum Yields, Radiative Lifetimes, and Interaction with Phonons

There is a variation of emitter intensities arising from weak absorption of the host material and the proximity of defects to hBN surface, through the loss of quantum yield through non-radiative channels, or by energy transfer to neighboring defects. However, a recent study on direct measurement of quantum efficiency of SPEs in hBN showed record high QEs of up to $(87 \pm 7)\%$ at a wavelength of ~ 580 nm. Two SPE families were also identified in the above study with well-separated average QEs. Family 1 whose ZPLs were concentrated around 580 nm demonstrated an average QE of $(62 \pm 9)\%$, whereas Family 2 with ZPLs at 660 nm showed a value of $(36 \pm 8)\%$ for average QE. These results indicate that there could be two distinct electronic structures involved in defect structure.

Emission lifetime is determined by the intrinsic oscillator strength of the SPE. Emitters in Families 1 and 2 exhibit different radiative and non-radiative lifetime, implying differences in the electronic state of the defects or their interaction with impurities and trap charges in the surrounding environment, possibly due to the proximity of these defects to the surface of the flakes.

The PL spectra probed from defects in h-BN show consistent phonon sideband with energies in the range 60 –160 meV for Group 1, and 15 –30 meV for Group 2 across different studies. The magnitude of PSB is varied with a Debye-Waller factor

of 15–40 % for Group 1 and a higher percentage of 50 –80 % for Group 2. Phonons also cause ZPL broadening through associated inhomogeneous broadening effects at high temperatures [149].

2.4.4 Absorption and Emission Dipole Polarisation

Spin-preserved optical transitions may occur through interaction between the electric transition dipole of the defect and the electric field of excitation light. The dipole of the emitter is defined as $d_{if} = \langle \psi_i | \hat{d} | \psi_f \rangle$, where ψ_i and ψ_f are the wavefunctions of initial and final states, respectively. The transition dipole is a vector that is aligned respectively to the defect orientation. Consequently, the orientation of hBN plane, the incident angles, and the polarisation of light will cause the transition dipole to respond in different ways. The fundamental mechanism governing these behaviors in point defects is known as the Huang-Rhys model [64]. In the Huang-Rhys model of two electronic states, direct absorption must have the absorption and emission dipoles well aligned. Jungwirth et al., [69] reported that Huang-Rhys model succeeded in explaining polarisation properties of the single defect transitions in hBN when the energy difference between the excitation light and the ZPL is less than the maximum energy of one phonon in HBN. Nevertheless, when this energy surpasses one phonon energy, this results in the misalignment of the absorption and emission dipoles [41]. A mechanism is proposed to explain these observations, in which an optical transition might happen upon indirectly exciting a defect through a third intermediate electronic state. The presence of fast-decaying intermediate and a long-lived metastable state has also been reported in another work [76].

2.4.5 Wavelength Tunability

Various methods have been developed to tune the ZPL wavelength of hBN emitters. The most convenient approach is to use the mechanical strain method, and this strategy has been applied successfully to achieve a tunning magnitude up to 65

meV; a record for 2D material based quantum emitters [105]. Due to the reversibility and non-invasion, this method is appealing for the control and manipulation of quantum emissions.

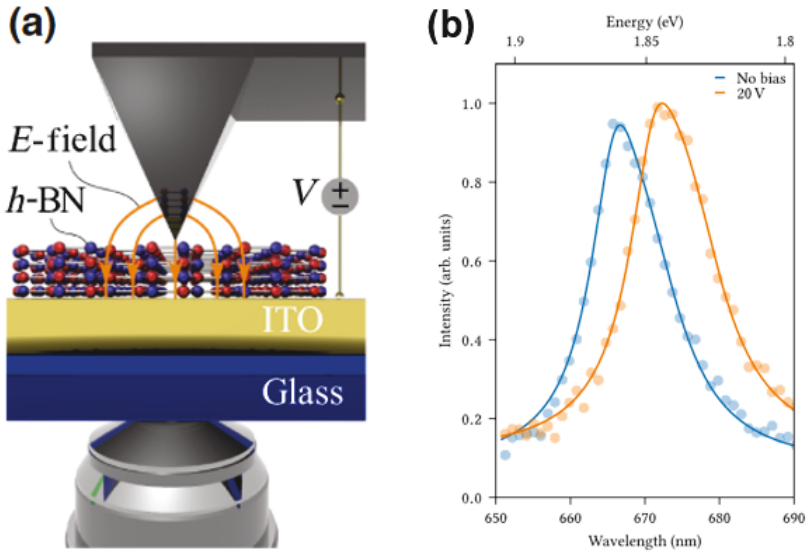

Figure 2.4 : (a) Schematic representation of the experiment using an AFM tip to deliver an electrostatic field causing a Stark shift of the ZPL of hBN emitters; (b) Spectra of the Stark-shifted h-BN SPE fluorescence [119]. Reprinted with permission from [119].

Single-photon emission from h-BN can be electrically controlled via the Stark effect [120]. A large and reversible Stark shift (as shown in figure 2.4) of 5.5±0.3 nm at a zero-field wavelength of 670 nm was induced by applying 20 V electric field perpendicular to the substrate [119]. The emission of SPEs can be tuned via a local in-plane electric field that gives rise to Stark effect [184]. Angled resolved Stark effect unveiled the broken inversion and rotation symmetries of the point defects. Another report in spectral tuning of hBN emitters achieved a shift in the wavelength over a spectral range of up to 15 nm, using the photo-doping effect of ionic liquid-based devices [106]. In this study, two different conductive polymers were used as

the electrolytes. When the voltage was applied, no spontaneous spectral jumps were observed; however, upon gradual applying bias, the ZPL blue-shifted in the positive bias of +6V, whereas it red-shifted when switching the voltage to -6V. However, there is no distinguishable trend observed between the ZPL energy of emitters and their corresponding shifting behaviours, indicating the involvement of different types of defects and high sensitivity of the defects towards the host environment.

2.4.6 Interaction with magnetic field of SPEs in hBN

Quantum emitter in hBN was first assumed to have magnetic-independent ground states [83, 91]. However, recent advances have brought important observations of optically addressable spin-dependent defects in hBN [23, 42, 52, 158]. By applying an 890G magnetic field from parallel or perpendicular direction to the plane of hBN flakes, the single-photon emission in hBN was modulated, depending upon the light incident directions. A singlet-ground-state configuration with intersystem crossing to the triplet manifold was identified as a possible path for the absorption and emission. However, field-dependent emission appears to be relatively rare for hBN's visible emitter, and a large number of similar emitters show field-insensitivity. The change in the brightness of some emitters in h-BN upon applying the magnetic field is indicative of the presence of optically addressable spin [42].

Very recent ODMR studies probing hBN defects proposed a particular defect - the negatively charged boron vacancy ($V_B{}^-$), showing fluorescence lines associated with the triplet (S=1) ground state and zero-field splitting of $\sim 3.5GHz$. The characterised emitters belong to group 2 with an unprecedented broad emission. The defect configuration was proposed to be carbon impurities related defects. [52].

2.4.7 Engineering hBN to Generate Single Photon Emitters

Hexagonal boron nitride is an emerging platform for ambient temperature quantum photonics by possessing room temperature-single-photon emitters at atomic defects. Recently, various methods have been applied to generate fluorescent defects in hBN. Tran et al. used an annealing method (850^0C in inert gas) and gas mediated electron beam irradiation to realize single photon emitters in hBN [24, 164] (Fig. 2.5) Chemical etching in the presence of phosphoric (H_3PO_4) and sulfuric acids

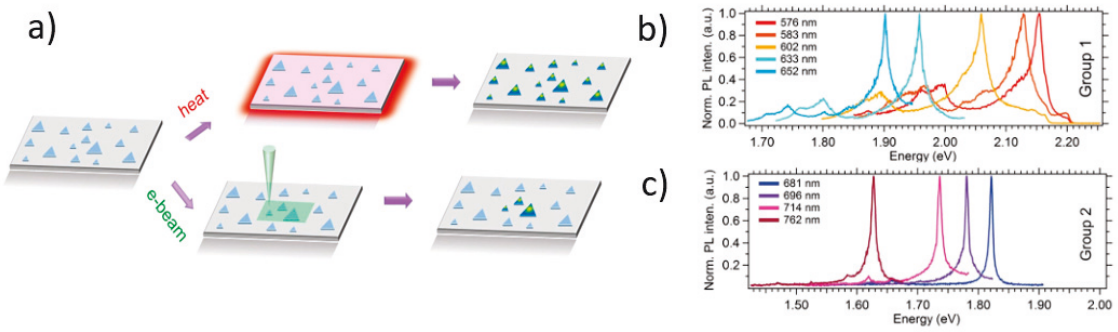

Figure 2.5 : Generation of emitters in hBN. (a) Schematic illustration of two independent processes that generate emitters: annealing and electronbeam irradiation. As-grown, dropcast hBN flakes are either annealed in an argon environment or irradiated by an electron beam in a lowvacuum H2O environment; (b) Five examples of emitters in Group 1 with ZPLs range from 1.90 - 2.20 eV; (c) Four examples of emitters in Group 2 with ZPLs from 1.65 - 1.85 eV [164].

(H_2SO_4), and ion irradiation are also demonstrated to generate emitters in h-BN [24], and the interaction of electronic transition and single Raman active mode of h-BN is supposed to dominate the emitters' spectral characteristics.

Moreover, Choi et al. demonstrated the formation of quantum emitters in large hBN flakes by ion implantation or focused laser irradiation and the emitters are found to localise at the edges or grain-boundaries of the flakes [27]. Single-photon

emitters are also generated under plasma treatment using argon gas [185] or oxygen gas [172]. These emitters are always close to the crystal surface; meanwhile emitters formed by electron irradiation are created randomly throughout the entire crystal. This can be explained by the lower kinetic energy of the ions in the plasma compared to the kinetic energy of electrons in the accelerator.

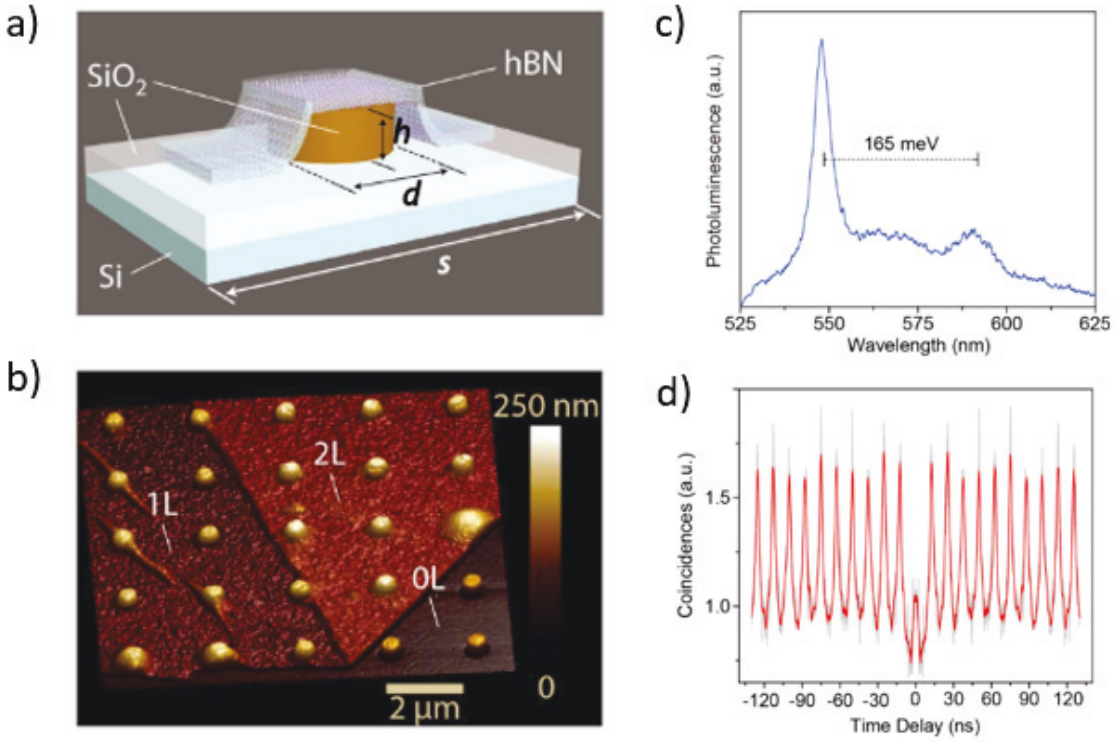

Figure 2.6 : Strain-induced activaion of single photon emitters in hBN. (a) Schematic illustration of $\sim$ 20 nm thick flake of hBN transfered on silica nanopillars; (b) 3D reconstruction AFM image of hBN flakes; (c) Photoluminescence spectrum from an active pillar site showing a relatively sharp ZPL indicating the single photon nature of the emission; (d) Second order autocorrelation function with $g^{(2)}(0) = 0.27 \pm 0.02$ [129].

Another effort [129] to near−deterministically activate quantum emitters in hBN is nanoscale strain engineering of a few atomic -layer hBN film on top of a large array

of nanopillars as illustrated in Figure 2.6. Due to van der Waals forces, the hBN thin film takes on the shape of pillars, creating a localised strain near the edges. The optically active defects in hBN can be activated via charge trapping at these highly strained areas. Quantum emitters in hBN are obtained during the fabrication of hBN cavities employing two approaches based on focused ion beam and electron beam induced etching techniques [81]. Various growth methods have been involved in generating fluorescence centres in hBN. Large area chemical vapor deposition (CVD) growth of hBN [106] achieved a much narrower ZPL energy distribution compared with hBN film grown by molecular beam epitaxy techniques. Ziegler et al. also reported the discovery of SPEs in a zero-dimensional boron nitride allotrope (boron nitride nanococoon, BNNC) with emission at visible wavelength [200].

2.5 Transition Metal Dichalcogenides

2.5.1 Compositions and Structures

TMDCs refer to a family of layered materials with the compound MX_2, where M is a transition metal from group IV B, VB, or VIB, and X is one of the chalcogens, sulphur, selenium or tellurium. In this compound formula, the metal atoms are sandwiched by two layers of chalcogen atoms in the form X-M-X resulting in a trigonal prismatic structure [103]. These compounds are strongly bonded in X-T-X layers, whereas 2D layers are stacked and held together by relatively weak van der Waals forces. In monolayer form, the M and X atoms are arranged in two-dimensional hexagonal arrays.

2.5.2 Electronic and Optical Properties

2D TMDCs such as MoS_2, $MoSe_2$, WS_2, WSe_2 are semiconductors and have bandgaps of amplitudes comparable to those of conventional groups III–V [99, 101]. In particular, when down to a single layer, the bandgap of TMDCs becomes direct

while it is indirect in multilayer; The cross-over gap located at the K and K' points of the electronic spectrum [99, 150]. The change from indirect to direct bandgap is due to the quantum confinement effect in the out-of-plane direction that increases the indirect gap size. In a direct bandgap, absorption is more efficient as it is easier for photons to have equal energy to the bandgap. Meanwhile, in the indirect bandgap, absorption is less efficient due to the requirement of additional photon absorption and emission to compensate for the difference in momentum. The electronic structure of layered TMDCs gives rise to their extraordinary optical properties. Their direct bandgap enables enhanced interactions of transition dipole with excitation light. Strongly bound excitons (with binding energy up to 1eV) [58, 168], charged excitons (trions) [98, 136], and excitonic molecules (biexcitons) are generated owing to strong Coulomb interactions and reduced dielectric screening in these materials. Owing to large exciton binding energy, these 2D materials exhibit strong excitonic emissions.

2.5.3 Valley Index in TMDC monolayers

2D TMDCs possess strong spin-orbit coupling due to the d orbitals of the heavy metal atoms [199]. Strong spin-orbit coupling together with inversion symmetry breaking generates two inequivalent energy valleys at the K and K' points in the Brillouin zone (Figure 2.7). Energy differences in these two valleys can be addressed using circularly polarised light [19, 68, 100].

Circularly polarised light (e.g. left handed polarised light σ^-) can actually preferentially populates excitons or trions in one particular valley (e.g. the K valley). The degree of valley polarization can be quantitatively evaluated using the equation:

$$\rho = \frac{I(\sigma^+) - I(\sigma^-)}{I(\sigma^+) + I(\sigma^-)} \tag{2.36}$$

where I(σ^+) and I(σ^-) are right and left circularly polarised emission intensity, respectively.

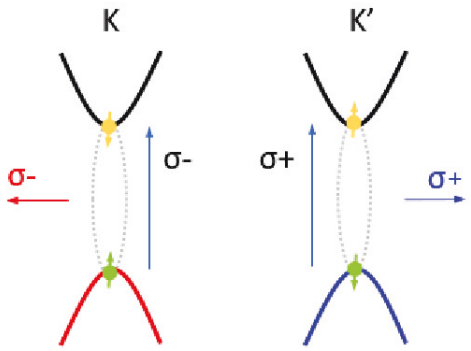

Figure 2.7 : (a) Cartoon illustrating optical selection rule for excitons in the K and K' valleys (green circles correspond to electrons in the conduction band and yellow circles correspond to holes in the valence band). σ^+ circularly polarised light leads to σ^+ emission from the K valley, while σ^- circularly polarised light leads to σ^- emission from the K' valley

This binary degree of freedom is thus promising for applications in communication and information storage, where the information can be encoded by manipulating the valley pseudo-spins [141]. A recent theoretical work suggested that polarised meta-surface could increase valley polarisation contrast achieved by modifying the vacuum field at the TMD location, without the need of a circularly polarised excitation beam [67].

2.5.4 Challenges facing 2D TMDCs for photonic applications

Although 2D TMDCs possess distinct optoelectronics properties, there remain some challenges to realise practical TMDCs based devices. First, the photoluminescence quantum yield of TMDCs is much lower than the value of direct band gap semiconductors, especially at multilayer thickness; for instance, the PL quantum yield of monolayer WS_2 decreases by more than 100-fold upon increasing to

bilayer and gradually annihilates with a further increase in thickness [197]. Second, the atomic thickness of such 2D TMDCs constraint their interaction length with light that hinders their light absorption efficiency. To meet the challenge of the limited emission efficiency in 2D TMDCs especially in monolayer form, the solution is to integrate 2D TMDCs with photonic nanostructures to boost their emission efficiency.

2.5.5 Integration of TMDCs with Photonic Nanostructures

Plasmonic and photonic crystal cavities are the two most common photonic structures used for enhancing the emission properties of 2D TMDCs.

Plasmonic enhancement

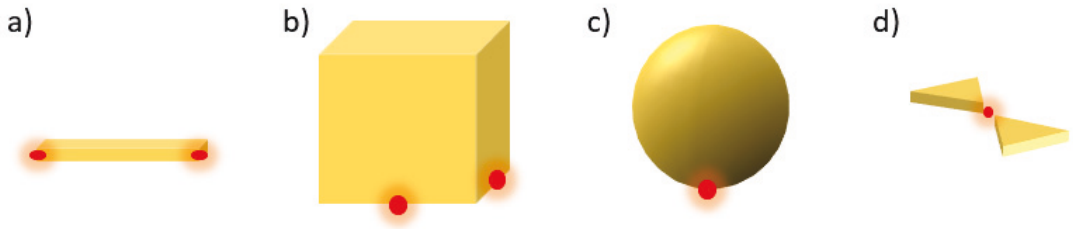

Figure 2.8 : Examples of plasmonic cavities. Schematic designs of plasmonic nanoparticles of different geometries: (a) bar ,(b) cube,(c) sphere and (d) bowtie.

The simplest form of plasmonic cavities is metal nanoparticles [7, 73], where the light field can be confined through coupling to electron oscillation or plasmons to give rise to strongly localised 'hot-spots'. With the advance in nanofabrication techniques, nanoparticles can be tailored to the localised surface plasmon polariton by precisely adjusting the size and shape [55] to obtain better concentration of light. Figure 2.8 shows some examples of metal nanoparticles with different shapes. Particularly, bowtie nanoantennas have been shown to provide extraordinarily high

field enhancements [121, 125], directionality [87, 196]. However, the cost needed to pay for such strong confinement is the high damping loss from metals. The quality factor of the plasmonic structures is typically in the order of ten [75].

Dielectric cavities

Photonic crystal cavities, however , have been realised to achieve high-Q factors up to 2 millions, while maintaining small mode volumes. The atomically thick 2D TMDCs have naturally passivated surfaces without any dangling bonds, that favour their integration in devices (Figure 2.9a-c), including planar photonic crystal cavities [47, 181, 182], optical microcavities [35, 95], and optical ring resonators [189]. Strong coupling between 2D TMDCs and cavity modes has also been observed in various systems, showing Rabi splitting of $\sim 46 \pm 3meV$ (Figure 2.9d) [95].

These examples mentioned above are evidence for the enhancement of light-matter interaction in 2D TMDCs and their emission manipulation through integration with photonic nanostructures. Considering the synergetic potential and flexibility offered by this heterogeneous platforms, it is imperative to seek for novel designs to control and manipulate light emitting properties of 2D TMDCs.

2.5.6 WSe_2 Nanophotonics

Much efforts have been predominantly invested to study monolayer WSe_2 (Figure 2.10) in terms of applications as well as dynamics of exciton formation and valley depolarisation.

This material has received much attention as it enables the realisation of strong coupling regimes of light-matter interaction, which is considered weak in 2D materials. All the properties of TMDCs materials which are mentioned in 2.5.2, can be applied in this case. Figure 2.11 describes the energy structure of single-layer WSe_2 with the band structure in figure 2.11a showing the direct bandgap of 1.6 eV

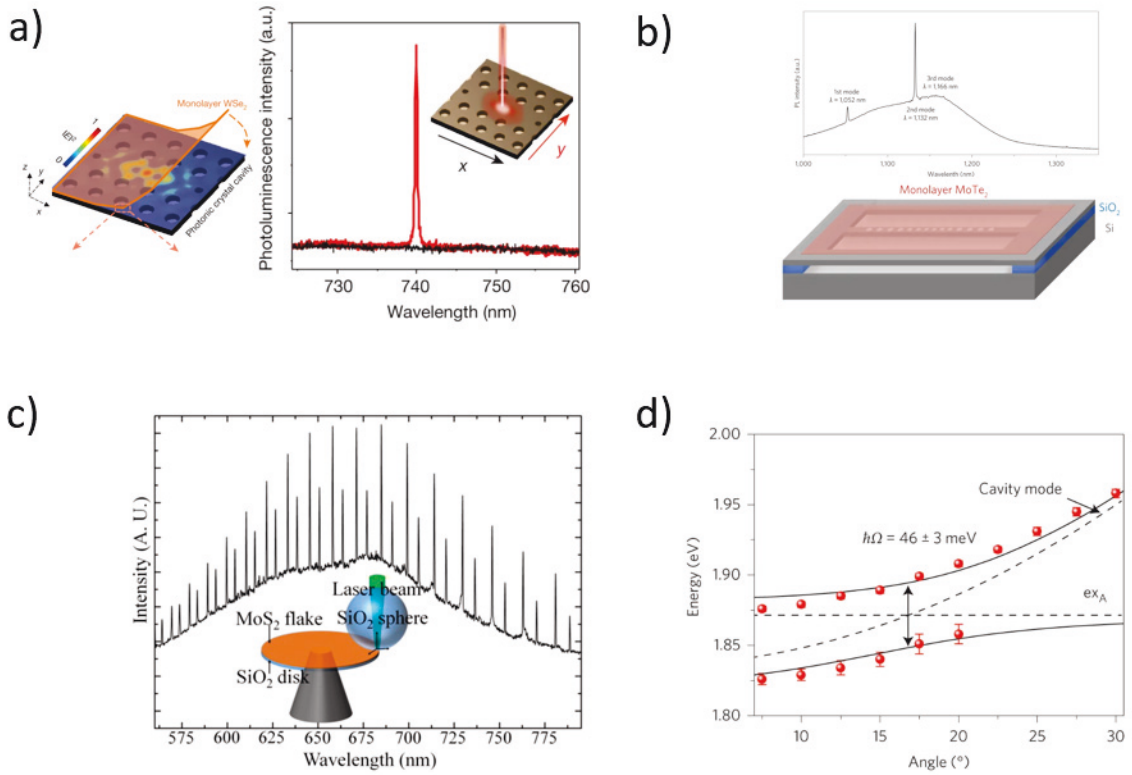

Figure 2.9 : (a) Cartoon depiction of a nanoscale laser system showing electric field profile (in-plane, x-y) of the fundamental cavity mode before WSe_2 transfer and polarisation-resolved photoluminescence spectrum of the device showing a completely polarised narrow emission at $\sim$ 740 nm, Black (red) line corresponds to detected linear polarisation in the x (y) direction [182]; (b) Top image is the PL spectrum of the nanolaser at room temperature under the pump power above the lasing threshold and schematic of our device including a silicon photonic crystal nanobeam laser structure suspended in air with a monolayer $MoTe_2$ on top (bottom image) [92]; (c) PL spectra of the laser device (top) and schematic configuration of the coupled microsphere/microdisk optical cavity with 2D MoS_2 (inset) [138]; (d) The energy versus angle dispersion, extracted from the angle-resolved photoluminescence spectra, showing Rabi splitting of $\sim 46 \pm 3$ meV [95]. Adapted with permission from [92, 95, 138, 182].

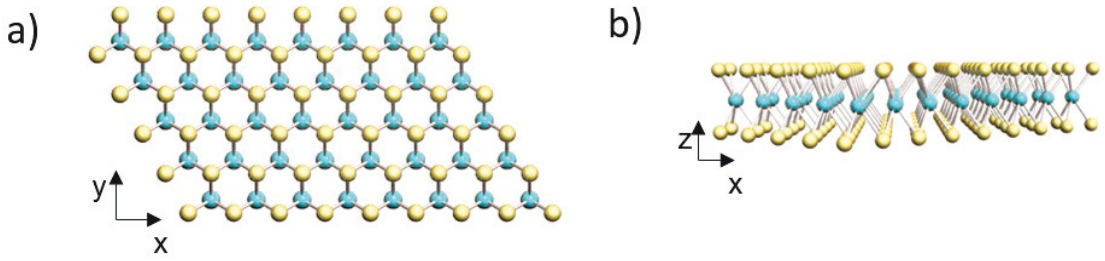

Figure 2.10 : Crystal structure of monolayer WSe_2. a) Top-view presents a single layer WSe_2 forming a two-dimensional hexagonal lattice,; b) Side-view shows a single-layer WSe_2 consisting of W layer embedded between two Se layers.

and the corresponding absorption spectrum (orange curve) and photoluminescence (blue curve) in Figure 2.11b. The direct bandgap is measured to be $\sim 1.6eV$. There are two optical transitions in WSe_2; namely, X_A and X_B associated with transitions from the upper and lower valence band to the conduction band. Charged excitons or trions were also discovered in monolayer WSe_2. PL spectra in monolayer WSe_2 can be tuned by various methods including electrical doping, magnetic field, changing laser intensity, or modifying the surrounding dielectric environment and interaction with optical cavities.

The exciton and coherence lifetimes are two characteristics to describe the temporal behavior of single layer WSe_2. The exciton lifetime presents the average time during which an exciton exists. In contrast, coherence lifetime defines the period when the state of excitation of an exciton (i.e., polarisation) remained unchanged. The exciton lifetime usually is longer than the coherence time.

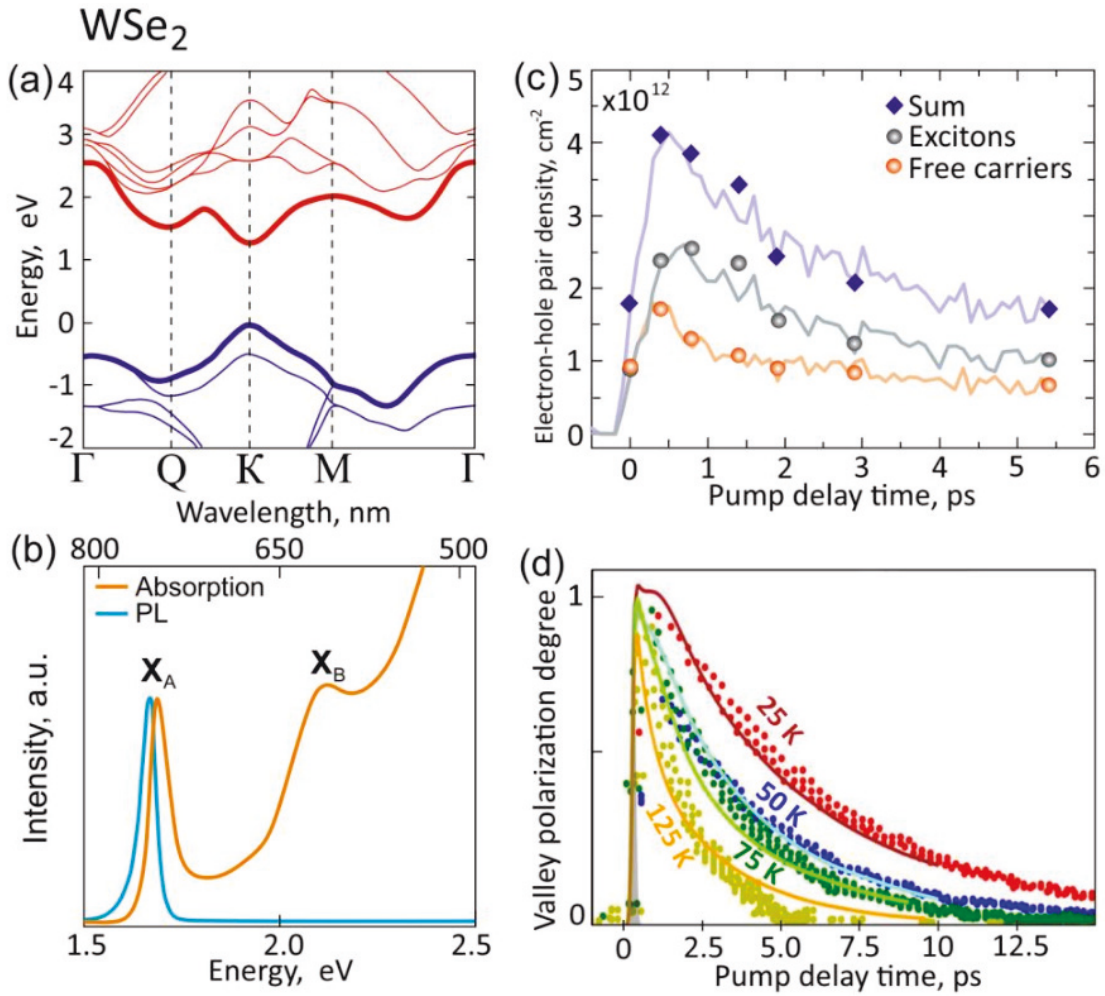

Figure 2.11 : Optical properties of monolayer WSe_2. (a) Electronic band structure, blue and red curves are valence and conduction band, respectively [152]; (b) Absorption (orange curve) and emission spectra (blue curve) of monolayer WSe_2 at room temperature [197]; (c) Absolute electron-hole pair densities for excitons (black spheres), free excitons (red spheres), and total density of the two contributions (blue diamonds) [152]; (d) The valley polarisation degree as a function of pump delay time at different temperatures [112]. Adapted with permission from: (a) – [152], (b) – [197], (c) – [152], (d) – [112]. Copyright (2020) American Chemical Society.

Chapter 3

Effects of high energy electron irradiation on quantum emitters in hexagonal boron nitride

Owing to superior optical properties as described in Chapter 2, section 2.4 , hBN quantum emitters are of crucial importance to study. Therefore, in this chapter we first explores the generation of single- photon emission from hBN by using high energy electron beam irradiation. The optical and photodynamic properties of the generated emitters are also investigated. This work was conceived by Igor Aharonovich and Milos Toth. The hBN samples were received from by Takashi Taniguchi and Kenji Watanabe (NIMS, Japan), and James H Edgar (Kansas State University). The electron irradiation was performed by Takeshi Ohshima, Hiroshi Abe (QST, Japan). Optical measurements, AFM, Raman measurements and analysis were performed by Ngoc My Hanh Duong and Minh Nguyen, with some assistance from Mehran Kianinia. All the authors discussed and wrote the manuscript.

3.1 Abstract

Hexagonal Boron Nitride (hBN) mono and multilayers are promising hosts for room temperature single photon emitters (SPEs). In this work we explore high energy (MeV) electron irradiation as a means to generate stable SPEs in hBN. We investigate four types of exfoliated hBN flakes - namely, high purity multilayers, isotopically pure hBN, carbon rich hBN multilayers and monolayered material - and find that electron irradiation increases emitter concentrations dramatically in all samples. Furthermore, the engineered emitters are located throughout hBN flakes (not only at flake edges or grain boundaries), and do not require activation by high

temperature annealing of the host material after electron exposure. Our results provide important insights into controlled formation of hBN SPEs and may aid in identification of their crystallographic origin.

3.2 Introduction

Solid state materials capable of hosting optically active single photon emitters (SPEs) are highly sought after for applications in quantum nanophotonics and quantum information processing [4, 10, 144]. To this extent, defects in diamond, silicon carbide and gallium nitride have been studied as promising candidates for SPEs [14, 20, 65, 116, 157]. The main advantage of this class of SPEs is their optically-stable room-temperature operation. Recently, hexagonal boron nitride (hBN) has been identified as a host of ultra-bright, room-temperature SPEs [16, 27, 41, 69, 76, 77, 91, 142, 145, 163, 164]. A significant advantage of hBN is its layered nature, which enables convenient preparation of very thin single crystal layers with thickness of below 50 nm and monolayers. hBN also possesses a wide bandgap of 6 eV, which is advantageous for creating stable, isolated, deep-trap defect states.

SPEs in hBN have so far been observed in a range of materials, including bulk crystals [102, 166], mechanically-exfoliated multilayers [27, 41], liquid-exfoliated flakes [164], nanotubes and other nanostructures [22, 200]. hBN samples often require high-temperature post-growth annealing in order for stable emitters to be observed, and it is not clear whether the annealing treatments create emitters or activate pre-existing defects. Recent efforts showed that plasma treatment [172, 185], ion implantation [27] or strain [129] can potentially be used to create/activate emitters. However, emitters in hBN possess a broad range of photophysical properties, and the atomic structure of the defects is a matter of debate [1, 115, 133, 156]. In addition, emitters in large-area mechanically-exfoliated flakes are often located

at grain boundaries or interfaces and emitters in large-area monolayers are sparse [27, 41, 185].

In this work, we investigate the effects of high energy (2 MeV) electron irradiation [71, 192] on a range of hBN samples. The electron exposure generates SPEs, via either the generation of new defects or optical activation of existing defects, and the generated emitters were characterized using photoluminescence (PL), time-resolved measurements and photon correlation analysis. Our results suggest that the electron irradiation process can be used to engineer optically-active defects without the need for high temperature annealing and the emitters can be located within the hBN flakes rather than just flake edges or grain boundaries. Finally we show that upon MeV electron irradiation, single emitters can be created in large area hBN monolayers - a task that has previously been elusive. Our results provide important insights into controlled generation of SPEs in hBN and will aid future studies of the atomic structure of the defects.

3.3 Experimental Section

3.3.1 hBN Sample Preparation

Four different types of samples were prepared; multilayer hBN flakes from high purity hBN (purchased from HQ Graphene), multilayer flakes from carbon-enriched hBN, multilayer flakes made from isotopically-enriched Boron-10 (99.2 ^{10}B) is and hBN monolayers (purchased from Graphene Supermarket) that were grown by chemical vapour deposition (CVD). High-purity flakes purchased from HQ graphene were synthesised by reacting fused boric acid with urea to form B2O3.xNH3 and then heated further in ammonia to 900^oC. The product was further heated in a nitrogen atmosphere at 1500^oC, allowing it to crystallize on a substrate surface.

The isotopically-enriched ^{10}B flakes were grown with a high purity Ni-Cr metal

mix with enriched ^{10}B powder in an alumina boat at 1550^oC for 24 hrs under an atmosphere of forming gas and nitrogen in a 1:4 ratio. It was subsequently cooled at a rate of 1^oC/hr until 1500^oC, whereby it was quenched to room temperature. This sample is referred to as B10 in the manuscript.

The multilayer samples were mechanically exfoliated with scotch tape onto silicon substrates and baked at 450^oC in air to remove residual adhesives and other unwanted carbonaceous material.

Monolayer hBN grown on Cu foil by CVD was cut into small squares and transferred onto Si substrates. The foils were then coated with PMMA to provide a platform to facilitate adhesion of the sample. The PMMA film containing the monolayer was then undercut by chemical etching of the Cu substrate with iron nitrate, leaving the polymer layer floating above. The film was transferred to a silicon substrate and heated to 120^oC for 20 minutes to promote adhesion, before being washed with acetone to dissociate the polymer.

3.3.2 Electron Irradiation

Electron irradiation was performed with a Cockcroft-Walton 2 MV 60 kW electron accelerator. The samples were wrapped in Al foil and placed on a water-cooled Cu plate for the irradiation process. The cooling ensured that the sample temperature was kept fixed at approximately room temperature (25^oC) during electron processing. Irradiation was performed at atmospheric conditions. The as-prepared samples were irradiated at 2 MeV with a fluence of $1 \times 10^{15}/cm^2$ for all hBN samples.

3.3.3 Optical Characterization

The irradiated samples were characterized using a home-built confocal PL setup with a 532 nm excitation laser. Details of the apparatus have been provided elsewhere [164]. Cryogenic measurements were performed at 10 K using a Janis ST500

cryostat system integrated with a high numerical aperture objective and 3-axis piezo sample positioning system.

3.4 Results and Discussions

Figure 3.1 details PL characterisation of emitters in a high-purity, single-crystal, multilayer flake of hBN. Figure 3.1a shows a confocal PL scan of a flake after electron irradiation. This flake did not contain any single luminescent centers before electron exposure. After electron irradiation, there was a high density of single luminescent emitters within the flake. A representative spectrum is shown in Figure 1b, with a sharp zero-phonon line (ZPL) at ~ 590 nm and distinct phonon-sideband (PSB), red-shifted by $\sim$54 nm. The quantum nature of the emission is confirmed by measuring the second-order autocorrelation function, $g^{(2)}(\tau)$, as shown in the inset. The dip at zero delay time, $g^{(2)}(0) \sim 0.26$, is indicative of a single-photon emitter.

Figure 3.1c shows a confocal PL scan of (a different region of) the same irradiated flake after an additional annealing step performed at 750^oC under 1 torr of argon for 30 minutes. Figure 3.1d shows a representative spectrum of an emitter obtained after annealing (performed after electron irradiation). The quantum nature of the defect is once again confirmed by the $g^{(2)}(\tau)$ function (Figure 3.1d inset). Overall, the electron irradiation process created a distribution of ZPL energies, with preferential creation of luminescent defects emitting at ≈ 600 nm when excited with a 532 nm laser. There are no substantial, systematic differences between the properties of emitters created by electron irradiation only, annealing only, or a combination of irradiation and annealing. The annealing treatment can both create and destroy emitters, as has been reported previously [185].

To date, attempts to deterministically engineer single emitters in hBN have resulted with emitters located predominantly at edges and grain boundaries [41, 129, 185]. In contrast, the MeV electron irradiation can produce emitters both at edges,

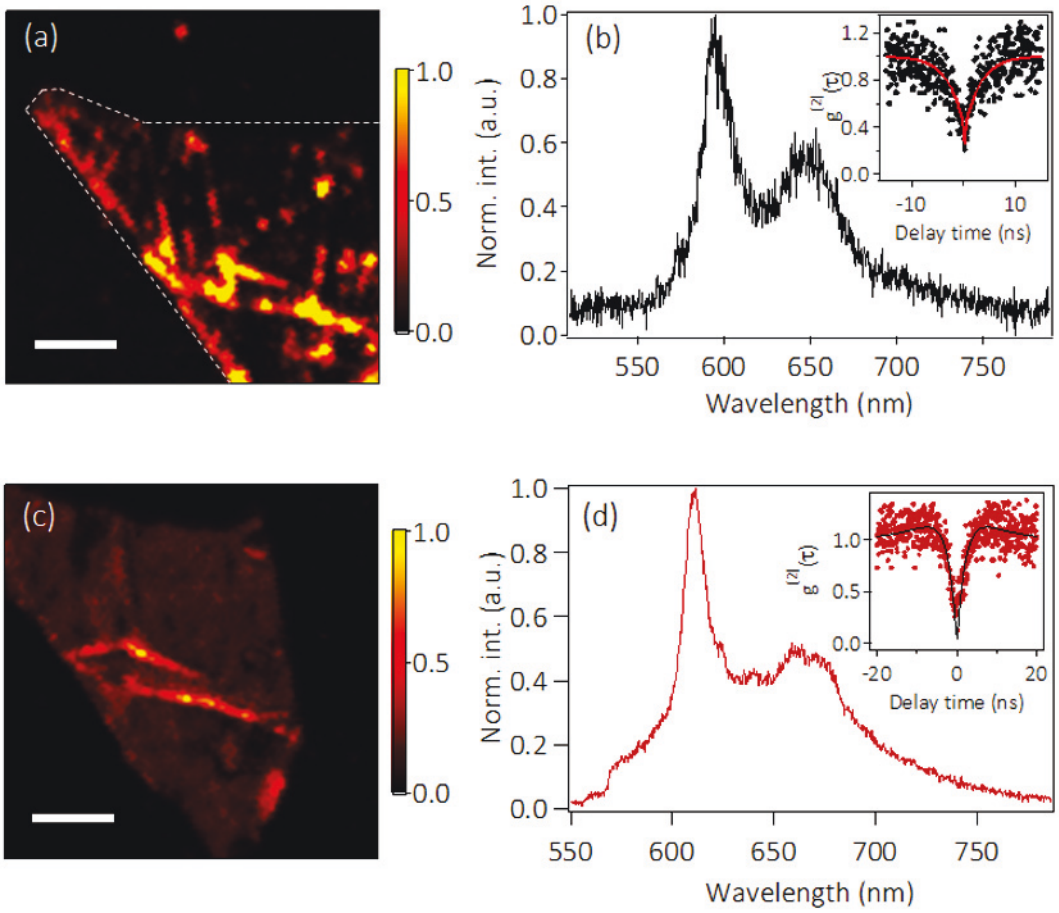

Figure 3.1 : Effects of electron irradiation and on high purity, single crystal, multilayer flakes of hBN. (a) Confocal PL map of an irradiated flake. (b) Typical PL spectrum of an emitter formed in irradiated flakes. The inset shows the corresponding second-order autocorrelation function. (c) PL map of a different region of the flake obtained after high temperature annealing. (d) Typical PL spectrum of an emitter obtained after electron irradiation and thermal annealing. The inset shows the second-order autocorrelation function. Both spectra were collected at 0.3 mW for 10 seconds at room temperature. All scale bars are 5 μm.

boundaries, and in the central, flat areas of flakes. Figure 3.2a shows an optical image of a large multilayered hBN flake that was subject to MeV electron irradiation. The thickness of the flake is 28.4±0.4 nm as confirmed by atomic force microscopy (AFM)

(see inset). Confocal PL maps of the same flake reveal emitters localized within the flake (white circles in Figure 3.2b). No grain boundaries or edges are visible near the emitters. The morphology of the flake is further confirmed by a high resolution AFM scan, as shown in figure 3.2c. Figure 3.2d shows a representative spectrum from one of the formed emitters, labeled '1' on the confocal map. The inset is a corresponding second order autocorrelation function, confirming the quantum nature of the emitter ($g^{(2)}(0) = 0.12$). We note that a subsequent annealing treatment destroyed all of the emitters shown in figure 3.2, and generated new emitters located at flake edges and grain boundaries.

To further investigate the effects of high energy electron irradiation, we compared hBN samples grown in the presence of carbon (i.e. BN doped to a C concentration of $\sim 10^{19} cm^{-3}$) and samples grown under standard conditions but using the ^{10}B isotope. The isotope is not important for our experiments as we do not study spin or phononic effects. However, this sample serves as a useful reference material to the high purity hBN, since the atomic structures of the emitters and the roles of impurities are uncertain. PL spectra of emitters found in these flakes exhibit characteristics that are similar to the ones in the high purity hBN. Figure 3.3(a, d) show three PL spectra recorded from emitters in ^{10}B and carbon-doped hBN, respectively. Most of the emitters have zero phonon line energies in the range of 580 - 600 nm, and a clear phonon sideband. The sharp edge around 565 nm is due to a bandpass filter used in our measurements. Figure 3.3 (b,e) confirm the antibunched nature of the emitters. Only one example is shown for clarity, however, most emitters found in the samples showed antibunching. Fig 3.3 (c, f) show the stability curves that confirm the emission is photostable and does not exhibit blinking or bleaching. Note that there was no annealing step involved in generating these emitters.

It has been suggested that carbon may play a role in these emitters. Our results do not support this assumption as we have not found any significant, systematic

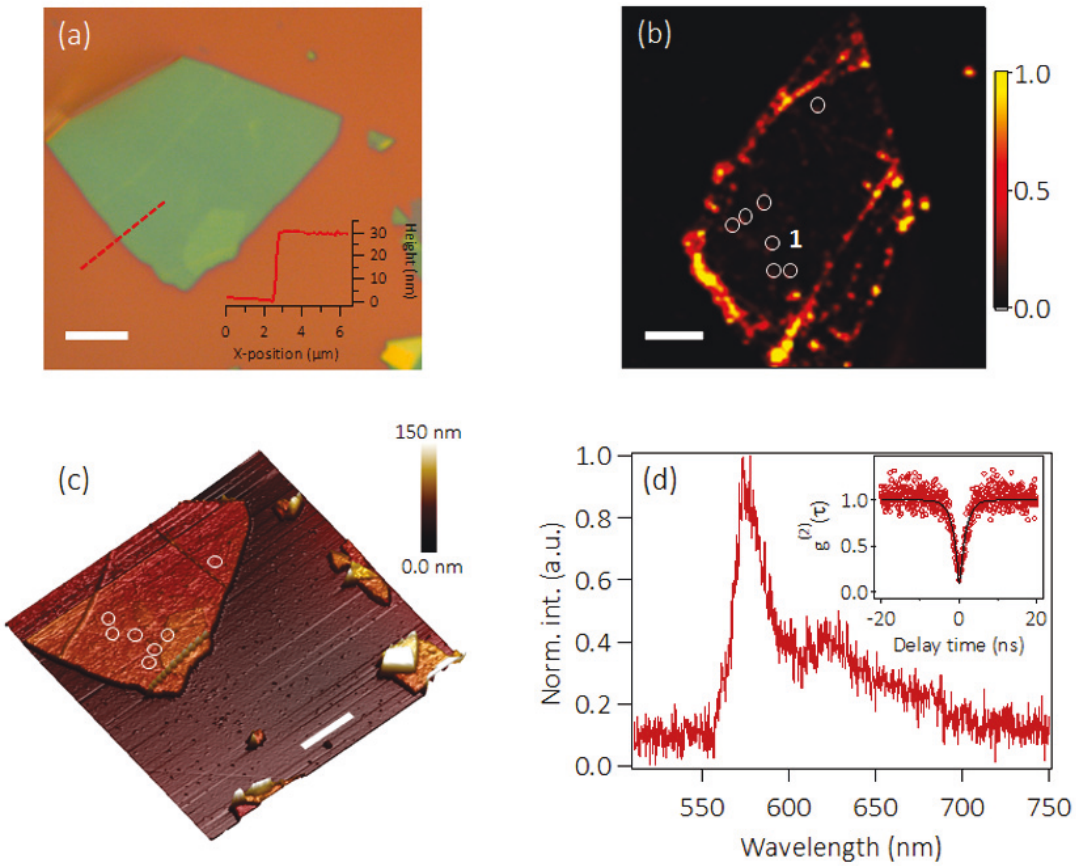

Figure 3.2 : Spatial characterisation of emitters in electron-irradiated, high purity multilayer flakes of single-crystal hBN. (a) Optical microscope image of a flake. The inset is an AFM line scan showing that the average thickness is ≈30 nm. (b) Confocal PL scan showing emitters created by electron irradiation. The emitter positions are shown by white circles on the confocal map. (c) AFM image of the same flake showing the positions of the emitters in b (white circles). It is noted that all emitters shown here are on the flat region of the flake. (d) PL spectrum of emitter 1. The inset shows the corresponding $g^{(2)}(\tau)$ autocorrelation function. All scale bars are 5 μm.

differences between the quantity and optical characteristics of emitters in the carbon-doped material and the other flakes investigated in this study.

Cryogenic PL measurements were performed on emitters in electron-irradiated

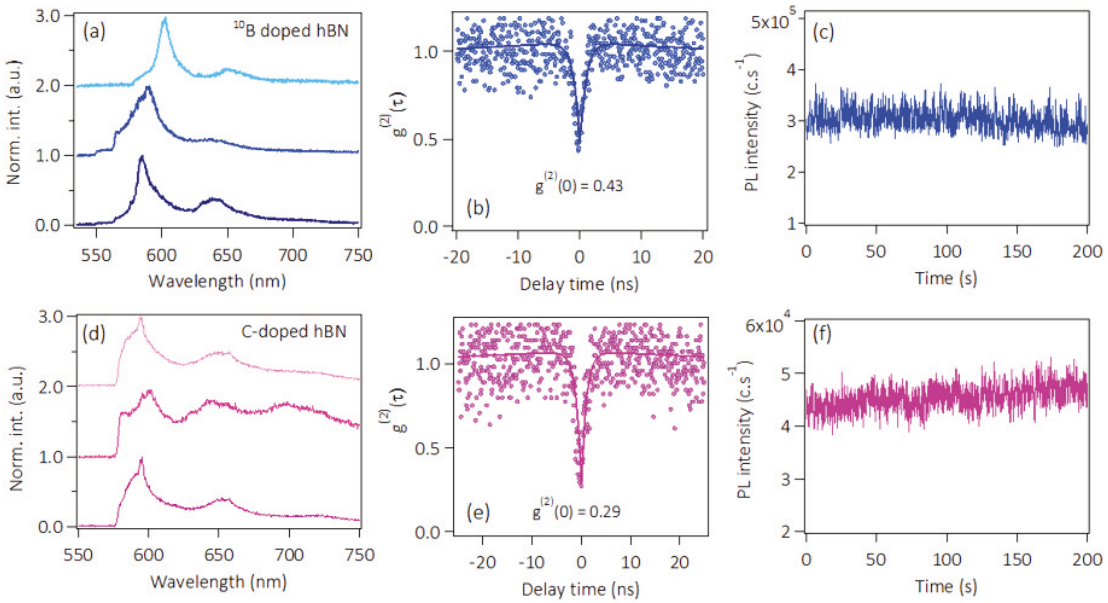

Figure 3.3 : Optical characterisation of emitters in electron-irradiated B10 and C-doped hBN samples. (a) Typical luminescence spectra of emitters in B10. (b) Second-order autocorrelation function of an emitter with $g^{(2)}(0) = 0.43$. A $g^{(2)}(0)$ value of less than 0.5 is indicative of single-photon emission (c) Corresponding stability curve of the aforementioned emitter. (d) Typical luminescence spectra of emitters in C-doped hBN. (e) An example of the second-order autocorrelation function of an emitter, with $g^{(2)}(0) = 0.29$. (f) Corresponding stability curve of the emitter. All optical characterisation was performed at room temperature with 532 nm CW excitation. All spectra were collected at 0.2 mW for 10 seconds.

flakes to see whether the ZPLs approach spectrometer-limited resolution and have the potential to be used for advanced quantum optics experiments [148, 149]. These PL measurements were taken at 10 K using a 707 nm excitation source. Figure 3.4a and 3.4b show two examples of ZPLs from the emitters, with a FWHM of 0.18 ± 0.05 nm and 0.35 ± 0.05 nm, respectively. Most of the studied emitters exhibit spectral fluctuations on the time scale of seconds, as shown in figures 3.4 (c, d), respectively. These results are consistent with emitters studied in samples that were not processed

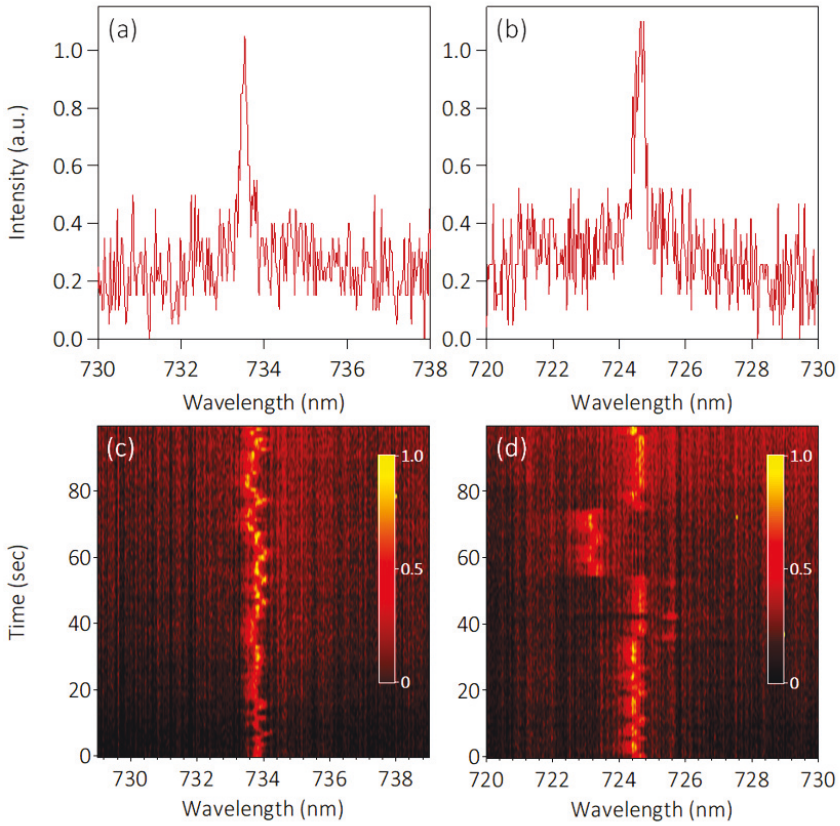

Figure 3.4 : Low temperature measurements of emitters found in electron-irradiated, high purity, single-crystal multilayer flakes. (a, b) Typical PL spectra recorded from two SPEs. (c, d) Spectra from the same emitters measured as a function of time. The emitters exhibit spectral diffusion. All measurements were performed at 10K.

by electron irradiation and in commercially-available multilayers [69, 149].

Finally, we studied CVD-grown monolayers of hBN. The monolayers were transferred from copper onto a silicon substrate (see Experimental Section). Figure 3.5a shows an atomic force microscope (AFM) image with a step of $\sim$ 0.79 nm corresponding to a hBN monolayer. The white spots on the monolayer are PMMA residue from the transfer process. PL scans reveal a relatively high density of emitters after electron-irradiation (see Table 1). Figures 3.5 (b, c) show a typical example of a confocal map and a spectrum from a single emitter within the monolayers. The

emitters have similar characteristics to those in large multi-layered flakes in terms of their emission wavelengths, FWHMs and phonon sidebands. Annealing for 1 hour at 750^oC under 1 torr of Ar results in the formation of new emitters within the monolayers. Figure 3.5(d, e) show a confocal map and PL from single emitters observed in an annealed monolayer, respectively. The annealing process destroyed the previously-characterised emitters, while simultaneously creating new ones. In general, emitters in monolayer hBN are less stable, more susceptible to being destroyed/deactivated by annealing, and exhibit more blinking and photobleaching under laser excitation than emitters in multilayer flakes of hBN - all likely due to a lack of encapsulation by the host material.

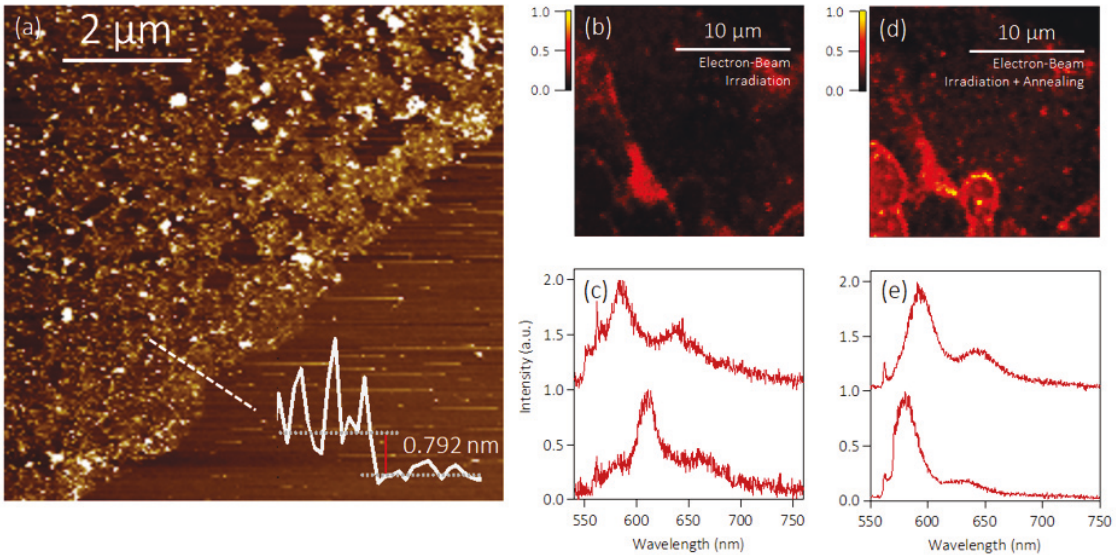

Figure 3.5 : Effects of electron irradiation on hBN monolayers. (a) AFM line scan showing an average monolayer thickness of 0.8 ± 0.40nm. (b) PL scan of an area where a hBN monolayer was deposited. (c) Typical PL spectra of emitters formed by electron irradiation. (d) PL scan of the same region of the monolayer after high-temperature annealing. (e) Typical PL spectra of emitters formed after annealing of the irradiated samples.

Table 1 summarizes the quantities of emitters found in all samples after MeV

Table 1. Statistics of emitter formation after MeV electron irradiation

	MeV irradiated	Annealed only
High purity hBN multilayers	∼9 emitters per flake	1-2 emitters per flake
B-10 enriched hBN multilayers	∼8 emitters per flake	1-2 emitters per flake
Carbon enriched hBN multilayers	∼5 emitters per flake	1-2 emitters per flake
CVD-grown hBN monolayers	∼5 emitters per flake	3 emitters per flake

*All flakes (and areas) were chosen to have a similar size of ∼20 μm

electron irradiation, and in control samples that were not irradiated but were instead subjected to the annealing treatment (1 hour at 750^oC under 1 torr of Ar). Clearly, electron irradiation is a promising method to create emitters without the need for annealing. The irradiation treatment consistently produced more emitters than the annealing process, and has the potential to generate emitters away from hBN flakes edges and grain boundaries. The samples that we investigated include C-enriched hBN, and our results do not support the hypothesis that C plays a role in the atomic structure of the emitters [156]. Another important observation is that only one 'class' of emitters was observed in all of our samples, all of which were either large flakes of mechanically-exfoliated multilayers, or large monolayers of CVD-grown hBN. Conversely, emitters in small, liquid-exfoliated flakes of hBN (supplied by Graphene Supermarket) can be broadly classified into two groups, the second of which is characterised by longer ZPL wavelengths and weak/negligible phonon sidebands. The absence of such emitters from all samples investigated in the present study suggests that they have a different atomic structure. On a practical level, the promising high energy electron irradiation technique presented here will likely accelerate understanding of the nature of single emitters in hBN, and their deployment in devices.

3.5 Conclusions

To conclude, we studied the effect of MeV electron irradiation on SPEs in hBN. Our results conclusively show that MeV irradiation can greatly enhance the formation of SPEs in hBN, without the necessity for a further annealing step. We also showed that upon irradiation, the emitters can form in the flat areas of the hBN flake. Finally, our work showed a similar distribution of emitters in carbon rich hBN and high purity hBN, therefore suggesting carbon may not be involved in the crystallographic structure of the defects. Our results are promising to develop a reliable procedure for engineering SPEs in hBN and unveiling their crystallographic structure.

Chapter 4

Integrated on Chip Platform with Quantum Emitters in Layered Materials

After successfully engineering single photon emitters in hBN, we then integrated these emitters in photonic waveguides. This is a crucial step towards the realization of multi-functional photonic integrated circuits. The project was conceived by Igor Aharonovich and Sejeong Kim. The AlN waveguides were fabricated and pre-characterized by Tsung-Ju Lu and Dirk Englund (MIT). hBN thin-film was obtained from Noah Mendelson. Coupling experiments, analysis and data visualization were performed by Sejeong Kim and Ngoc My Hanh Duong, with some assistance from Minh Nguyen for AFM measurements. All the authors discussed and wrote the manuscript.

4.1 Introduction

Implementation of quantum networks and photonic processors require interfacing multiple single photons on a chip [174, 178]. For this purpose, efficient integration of quantum light sources and photonic nanostructures, such as waveguides and cavities, is needed [15, 45]. To this end, photonic integrated quantum circuits have become an attractive research direction that is poised to deliver compact yet complex solid-state photonic quantum circuitry.

So far, efforts have been predominantly invested in 3D solid state systems, such as gallium arsenide[11, 78, 147] or diamond [40, 57], where the photon source is directly embedded in the material, which the resonator is consequently fabricated out

of. However, the fabrication of these structures is nontrivial, and alternative hybrid approaches are thus being pursued. One of these hybrid strategies involves transferring the photon source onto premade structures fabricated from a different material [13, 74, 167].This has been demonstrated for instance with epitaxially grown quantum dots (QDs). In this case the QD can be pre-characterized and subsequently lifted off and positioned onto a resonator fabricated from conventional semiconductors such as silicon or silicon nitride [31, 39, 79]. This pick-and-place approach is laborious and requires sophisticated nanomanipulators within scanning electron microscope. It also suffers from limited precision of alignment and positioning of the source with respect to the resonator. In a complementary methodology, stamping techniques with polydimethylsiloxane (PDMS) rubber stamps or similar materials have also been demonstrated [70, 122]. However, on balance, single-photon emission from the epitaxially grown QDs can only operate at cryogenic temperatures.

A promising approach to the above issues is the use of emerging single-photon emitters in 2D materials [4, 162]. Due to the 2D nature of the host, they can be transferred onto photonic structures via exfoliation and stamping, reproducibly and in ambient conditions [46]. Indeed, the first work on the coupling of quantum dots in 2D materials containing emitters–namely layered GaSe [160] or WSe_2, [128, 179] to photonic resonators have successfully been realized. However, due to the nature of the emission from these sources, their operation was limited to cryogenic temperatures. Quantum emitters in layered hBN are an ideal alternative. These sources are ultrabright and operate at room temperature [41, 69, 106, 129, 142, 163]. Taking the advantage of these features, in this work we report the integration of room-temperature hBN quantum emitters with aluminum nitride (AlN) waveguides. We demonstrate transmission of nonclassical light through the waveguide, hence paving the way for future and more complex realizations including photon multiplexing and photonic circuitry on chip.

4.2 Experimental Section

4.2.1 Sample preparation

Hexagonal boron nitride (hBN) nanoparticles in solution (Graphene Supermarket) were transferred onto the waveguides. The whole sample was subsequently annealed at 850 ^{o}C for 30 minutes in Argon atmosphere to avoid contamination. After annealing, the system was characterized via confocal microscopy.

4.2.2 Optical characterization

The optical characterization of the structures was carried out with a lab-built scanning confocal microscope. A continuous wave (CW) 532 nm laser was used for excitation. The laser was directed and focused onto the sample using a high-numerical-aperture objective lens (NA = 0.9, TU Plan Flour 100X, Nikon). The laser was scanned across the sample using a x-y piezo stage. The collected light was filtered using a 532-nm dichroic mirror (532 nm laser BrightLine, Semrock) and an additional 568-nm long pass filter (LP Filter 568 nm, Semrock). The signal was then coupled into a graded-index fiber, where the fiber aperture served as a pinhole. A fiber splitter was used to direct the light to a spectrometer (Acton SpectraPro, Princeton Instrument Inc.) equipped with a 300 lines per mm grating and a charge-coupled device detector with a resolution of 0.14 nm and to two avalanche photodiodes (SPCM-AQRH-14-FC, Excelitas Technologies, photon detection efficiency greater than 70 % at 700 nm, dead time of below 35 ns, and timing resolution of 350 ps) in a Hanbury Brown and Twiss configuration with a time-correlated single photon counting (PicoHarp 300, time precision $<$ 12 ps). In the non-local collection scheme, the excitation was fixed at a specific point and the collection was scanned using a scanning mirror (FSM-300, Newport).

4.2.3 Numerical calculations

Photonic simulations were performed by solving Maxwell's equations using the 3D FDTD method (Lumerical software). The size of the simulation domain is 16 × 5 × 2 μm^3 divided by a 20-nm mesh size. The emitter-waveguide coupling efficiency was simulated with an electric dipole as a light source while the grating coupler's efficiency was simulated using 'Mode' as a light source.

4.3 Results and Discussions

Figure 4.1a depicts schematically the integrated quantum photonic device consisting of the quantum light source and the ridge waveguide terminated with the grating coupler. The inset shows the cross-sectional view of the layered hBN crystalline structure formed by boron and nitride atoms (blue and red spheres respectively). The waveguide is fabricated from aluminum-nitride and optimized for single-mode propagation of light with 600 nm wavelength. The width and height of the waveguide are 1 μm and 200 nm, respectively. We chose nanocrystalline AlN for the waveguide as it has a transparent window in the spectral range from the ultraviolet to the infrared due to its large bandgap (6.2 eV). It also possesses low autofluorescence,good thermal conductivity and it is an electrooptic material [94, 96]. Additionally, the refractive index of AlN (n = 2.08) is very close to that of hBN (n = 2.1) [88, 131], which desirably minimize light reflection at the AlN/hBN interface. The single photons from the hBN flake placed onto the waveguide (purple solid in Figure 4.1a) are coupled and guided through the waveguide itself and detected at its end from the grating coupler. Figure 1b is the atomic force microscopy (AFM) image of the sample showing hBN flakes dispersed on the waveguide. The hBN flake indicated by the yellow arrow is the one characterized in this study. The height profile of the hBN flakes (Figure 4.1c) indicates partial agglomeration of the hBN flakes over the waveguide resulting in a total height of $\sim$ 200 nm.

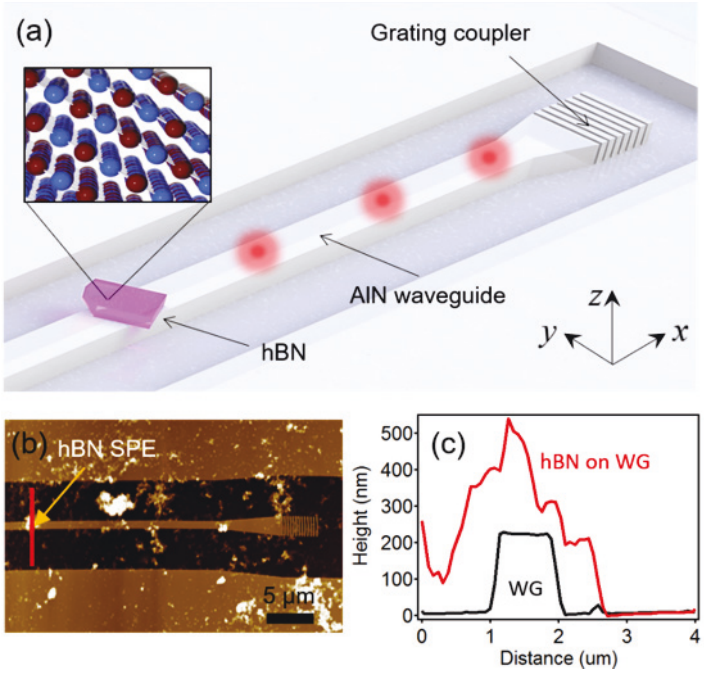

Figure 4.1 : Coupling of the hBN emitter to the AlN waveguide. a) Schematic view of the hybrid quantum photonic system showing a hBN flake (purple) positioned onto an AlN ridge waveguide (grey). The inset shows the layered van der Waals crystal. b) Atomic force microscopy (AFM) image of the hBN-waveguide structure. The position of the hBN emitter onto the waveguide is indicated (yellow arrow). c) AFM height measurement of the hBN emitter on the waveguide along the profile following the red line in (b); the ridge measured for the pristine waveguide is also shown (black trace).

The confocal photoluminescence (PL) map of the sample is shown in Figure 4.2a, where the optical excitation was performed with a continuous-wave green laser (wavelength of 532 nm) through a 0.9 NA objective. In this standard confocal map, the excitation and collection are from the same spot as the sample is scanned using a piezo stage: we refer to this scheme as local excitation. The hBN single-photon emitters (SPEs) on the waveguide were identified and subsequently characterized via this local excitation scheme. Figure 4.2b shows the zero-phonon line (ZPL) of

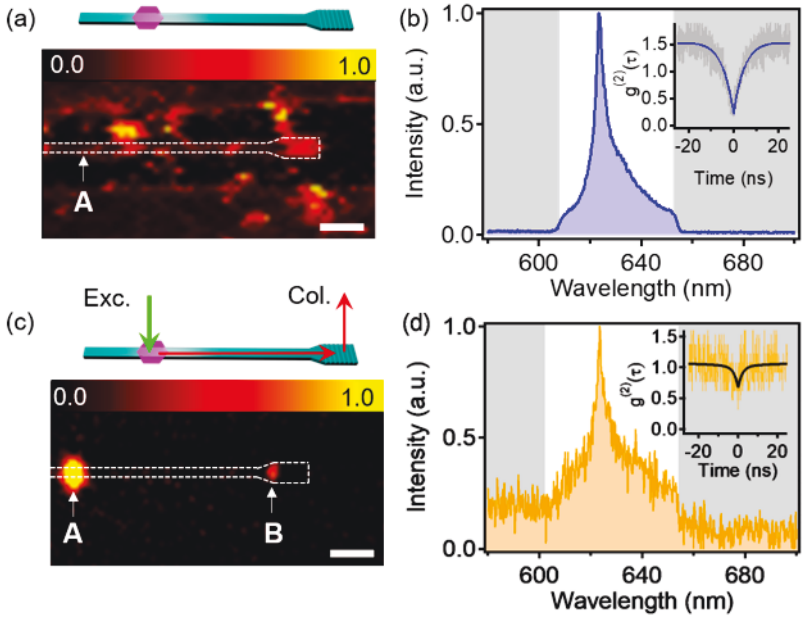

Figure 4.2 : Optical characterisation of the hBN-waveguide hybrid structure. a) Confocal map of the hybrid system under 532 nm CW laser excitation. Note, the emitter at point A is dimmer compared to the overall intensity within the map, and therefore is not clearly visible in the map. b) PL spectrum of the hBN emitter and its second-order autocorrelation $g^{(2)}(\tau)$ curve (inset) indicating single-photon emission ($g^{(2)}(0) < 0.5$). c) Confocal map where the 532-nm laser excitation is fixed on the emitter (spot A) and the collection is scanned over the sample; in collection the 532-nm laser is filtered out. The map shows that photons from the emitter couple to the waveguide and are detected at the grating coupler (spot B). d) PL spectrum and $g^{(2)}(\tau)$ curves (inset) are collected from the grating coupler (spot B) with excitation fixed at the emitter (spot A). Scale bars are 5 μm in both (a) and (c). The collection spectral window is indicated by the unshaded areas in (b), (d). The $g^{(2)}(\tau)$ curves are corrected for background and time jitter.

the hBN SPE at 623 nm with a linewidth of 4.24 nm (full width at half maximum of the fitted Lorentzian). Note, this corresponds to the hBN flake indicated in Figure 1b,c. The spectrum was integrated for 60 s at an excitation power of 2 mW. The

spectrum and second-order autocorrelation $g^{(2)}(\tau)$ measurements in Figure 2b were filtered using a bandpass filter (Semrock, (630 $\pm$ 28) nm) to spectrally reject the chromium luminescence peak from sapphire and to isolate the emitter's ZPL—the regions shaded in gray in Figure 2b,d display the spectral regions, which were filtered out. The insets in Figure 4.2b,d show the second order autocorrelation measurement $g^{(2)}(0)$ performed using a Hanbury Brown and Twiss interferometer and corrected for background and time jitter. A zero delay time value of $g^{(2)}(0) = 0.12$, indicates the single-photon nature of the emitter.

Next, the emitter was analysed with a modified collection technique which we refer to as non-local collection—the schematic of which, is shown in Figure 4.2c. In this scheme, the excitation laser (532 nm) is kept fixed at the location of the hBN SPE (spot A), while collection is acquired over a 30 x 30 μm^2 area using a scanning mirror; the 532-nm excitation laser is filtered out. Figure 2c shows the resulting confocal scan reveals luminescence both from the emitter, locally (spot A), and—at lower intensity—from the outcoupling grating (spot B). This demonstrates successful coupling and propagation of single photons from the hBN emitter through the waveguide structure. The bright emission from the spot B in Figure 4.2c is further analyzed with a spectrometer, revealing the same ZPL (623 nm) as from a spot A as shown in Figure 2d. Finally, to rule out the potential of an alternative SPE positioned on the waveguide and collected from spot B, we performed additional characterization of this area using the local excitation scheme, and found no other optically-active SPEs on the waveguide, further confirming that the PL from spot B originates from the hBN SPE at spot A.

The intensity of the PL signal measured at the grating coupler (spot B) is 1.2% of the total PL intensity collected from spot A. In figure 4.2d, the inset shows the resulting autocorrelation function, which has a significantly higher $g^{(2)}(0)$ value—most likely due to the increased background compared to that obtained in the local col-

lection configuration (i.e. directly from spot A; Figure 4.2b, inset). Note, that the propagation loss is negligible as AlN is transparent in the visible region and the propagation length is relatively short ($\sim$25 μm). Additionally, the waveguide is straight, so no bending losses are considered.

The extraction efficiency of the grating coupler is determined using finite-difference time-domain (FDTD) simulations. Here, we use the term extraction efficiency to refer to the portion of light that escapes the structure, and is collected through the high numerical aperture objective in the optical setup. For the single mode ($\lambda = 623$ nm) propagating light, the grating coupler used in our experiment has a calculated extraction efficiency of 9.8% through the grating coupler (spot B) and 11% through the objective (spot A). This is calculated considering that most of the extracted light is within 20^o in the far-field intensity pattern and we used an objective lens with NA = 0.9. The low extraction efficiency is attributed to the high refractive index (n = 1.8) of the sapphire substrate.

The maximum coupling efficiency from the simulation is 15.5% for 623 nm. Note that this coupling efficiency counts for the light coupled to both propagation direction, i.e., propagating left and right in Figure 4.3a. Therefore, the coupling efficiency from the emitter for a single propagating direction in the waveguide is half this value, 7.75%. Note that in our measurement, of all the light we collect directly from the emitter (spot A) through the 0.9 NA objective, only 11% couples into the waveguide—based on finite-difference time-domain (FDTD) simulations.

To complete the analysis on the system efficiency, we analyze numerically the coupling efficiency between the emitter and the waveguide. The hBN flake is simplified using a cuboid with dimensions corresponding to 1000 (width) $\times$ 1000 (length) $\times$ 200 (height) nm^3 and refractive index of 2.1 (in-plane). A dipole emitter with λ = 623 nm is at the center of the flake with polarization along the y-axis, orthogo-

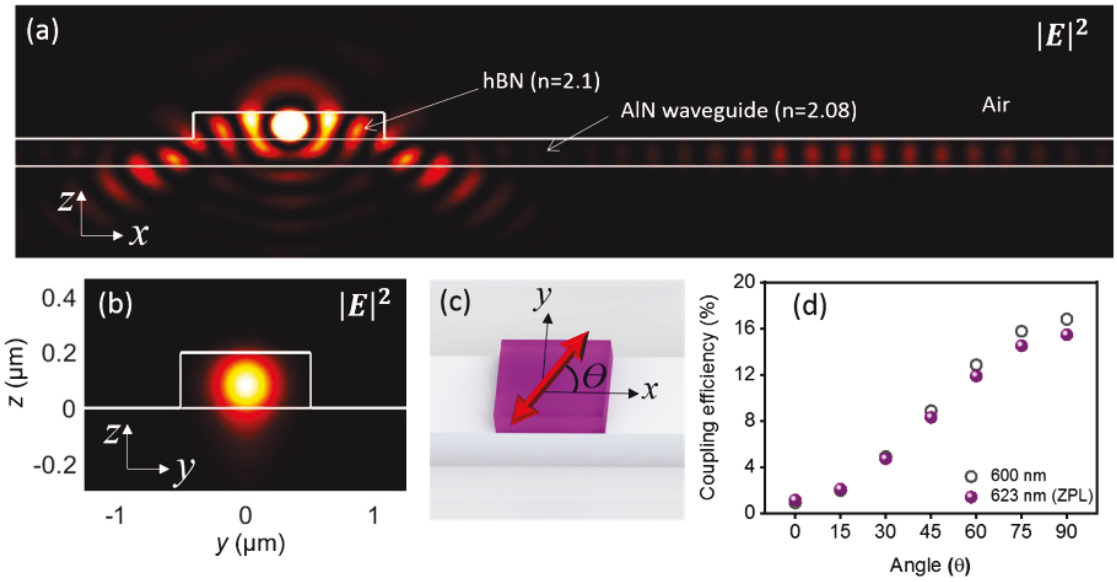

Figure 4.3 : a) Three-dimensional FDTD simulation showing the cross section (x-z plane) of the sample, where the emission from the dipole emitter couples to the waveguide. b) Mode profile of the waveguide at 623 nm. c) Three-dimensional schematic describing the angle of the hBN emitter (red arrow) with respect to the waveguide (the longitudinal axis of the waveguide is along the x-direction). d) Coupling efficiency of the light coupling to the waveguide with respect to the emitter's angle.

nal to the longitudinal axis of the waveguide. Figure 4.3a shows the crosssectional view of the electric field intensity indicating the light coupled to the AlN waveguide. The coupled light propagates as single Gaussian mode, as shown in Figure 4.3b. Additionally, the system is analyzed by varying the emission polarization of the SPE. We focus on the in-plane polarization as, due to the orientation of the flake with respect to the waveguide, this orientation is more relevant to our case. We therefore fix the polarizations in the simulation to the x-y plane while varying the angle θ with respect to the waveguide as displayed in Figure 4.3c. Figure 3d shows the coupling efficiency of the emitter to the waveguide when the wavelength of the

dipole emitters are 600 nm and 623 nm, respectively. These two wavelengths were chosen in the simulation because the AlN waveguide was designed and optimized for 600 nm, while the hBN SPE in the experiment has a ZPL of 623 nm. Figure 3d shows that when the emission polarization is along the waveguide direction ($\theta = 0^o$) the coupling is very weak while the efficiency is maximized when the polarization direction is orthogonal to the waveguide ($\theta = 90^o$).

The hBN SPE in the experiment has a measured emission polarization of $\theta \sim 90^o$; in our estimate of the total coupling efficiency we thus use this value. The total efficiency of the device can be estimated by multiplying all efficiencies listed above, which results in a total value of 6.3% through the grating coupler as compared to the collection via the objective, which matches well with the value measured experimentally.

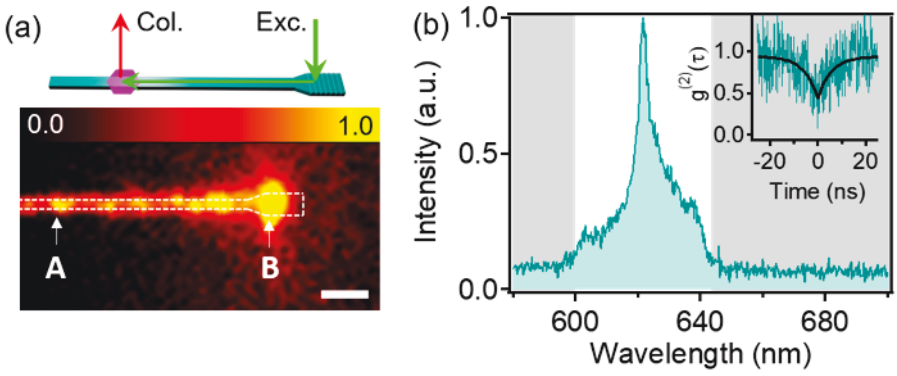

Figure 4.4 : Reversed excitation scheme of the system. a) Confocal map with excitation fixed on the grating coupler (spot B) and collection acquired from the emitter (spot A). Scale bar is 5 μm. b) PL spectrum and $g^{(2)}(\tau)$ function (inset) are collected from the emitter (spot B). The collection spectral window is indicated by the unshaded area in (b). The $g^{(2)}(\tau)$ curves are corrected for background and the time jitter.

Finally, the device was tested in what we refer to as reverse collection, i.e. with

the excitation spot fixed at the grating coupler and the collection scanned across the sample area (the laser excitation at 532 nm is filtered out)—the schematic is shown in Figure 4a together with the two-dimensional PL map. The green excitation laser is injected into the waveguide at the grating coupler (spot B) and guided through the waveguide to excite the same SPE that is characterized in Figures 1 and 2. The green laser also excites other photoluminescent defects along the waveguide, yet these reveal broad PL emission which is not related to the investigated SPE. Figure 4.4b shows the PL spectrum collected from spot A under this reverse collection scheme and displaying the same ZPL wavelength as in Figure 4.2. The corresponding autocorrelation measurement is shown in the inset of Figure 4.4b, with $g^{(2)}(0) = 0.42$. The different (higher) $g^{(2)}(0)$ single-photon purity for the reverse scheme in Figure 4.4b compared to that of the non-local scheme in Figure 4.2d is attributed to the different collection efficiency for the two different schemes. In Figure 4.4b, the emission is from a point defect source for which the collection spot size is determined by the NA of the lens. Conversely, in Figure 4.2d light is scattered by the grating coupler which inevitably has a larger, non-point-like emission. In addition, in the reverse configuration (Fig. 4.4b) the laser intensity can be increased at will to compensate for losses in the waveguide until we saturate the emitter. However, in the non-local scheme (Fig 4.2d) while we can still saturate the emitter, photons will be consequently lost while propagating along the waveguide.

4.4 Conclusions

To conclude, we demonstrated coupling of room-temperature SPEs in a 2D van der Waals crystal, specifically, hBN to an AlN waveguide. We achieved a coupling efficiency of 1.35% for the hybrid system, which matches—upon considering system non-idealities—the theoretical limit of $\sim 7.75\%$ estimated for the structure using FDTD simulations (compared to a direct collection via an objective lens from the

same spot). We also successfully demonstrated, efficient guiding of single photons in a variety of non-local excitation and collection schemes. The hybrid system constitutes the first step towards room-temperature, multi-functional photonic circuitry based on 2D material quantum light sources.

Further optimization can be achieved by improving the coupling efficiency, for instance by engineering the immediate dielectric environment of the emitter through capping with a third material. Better resonator geometries and couplers using the inverse-design principles [111] could also be engineered and fabricated, so that on chip operations can be realized. Finally, we note that research into strain engineered quantum emitters is accelerating rapidly [72, 97, 129], which may enable engineering the spectral characteristics of the emitter on demand, and in a precise location on the waveguide.

Chapter 5

Facile Production of Hexagonal Boron Nitride Nanoparticles by Cryogenic Exfoliation

The fluorescent properties of hBN nanoparticles are also drawing attention of scientific community as a promising label for single molecule localization microscopy [29]. This chapter, hence, discusses the fabrication of hBN nanoparticles using cryogenic mediated exfoliation. Furthermore, we study the photophysical and photodynamic properties of these particles using the wide-field imaging and Single molecule localization microscopy (SMLM). We prove that hBN nanoparticles are indeed suitable to be used as labels in a range of applications in biomedical imaging, drug delivery, and quantum sensing. Trong Toan Tran conceived the work. Evgenii Glushkov, Andrey Chernev, Vytautas Navikas, Jean Comtet and Aleksandra Radenovic (EPFL) performed the TEM and SLML measurements . The cryogenic fabrication, optical measurements and analysis were done by Ngoc My Hanh Duong, with some assistance from Toan Trong Tran, and Minh Nguyen. All the authors discussed and wrote the manuscript.

5.1 Introduction

Fluorescent nanoparticles are crucially important for a variety of applications, including imaging, sensing, drug delivery, energy and quantum nanophotonics [8, 56, 93, 126, 180, 193]. These applications impose a broad set of requirements on the nanoparticles, of which the physical and optical properties — particularly size, brightness and photostability — are amongst the most important. Sizes of or below 6 nm have been proven to enable live cell imaging, and shown to minimally perturb

biological systems. Moreover, nanoparticles smaller than 6 nm are usually eliminated from the body through the kidneys, whereas nanoparticles with sizes above 30 nm accumulate rapidly in the reticuloendothelial system [143].

Fluorescent colloidal quantum dots, which can have diameters below 5 nm, are an appealing candidate that satisfy the size prerequisite. These quantum dots, however, suffer from two major drawbacks: low photostability and biological toxicity, thus limiting their use in imaging and bio-marking applications [169]. Research of alternative platforms such as fluorescent nanodiamonds have therefore garnered significant attention in the last decade [60, 171]. While nanodiamonds can indeed host optically stable emitters in the form of color centres [5], mass production of particles with diameters below 40 nm is still challenging [21]. Furthermore, in order to achieve high fluorescence brightness requires cumbersome protocols of high energy irradiation and annealing that significantly increases price and limit broad widespread use of nanodiamonds.

An emerging material that can host ultra-bright fluorescent, optically stable defects is hexagonal boron nitride (hBN)-a layered van der Waals crystal with a wide bandgap of $\sim$6 eV. Similar to diamond, point defects in hBN can be isolated and exhibit single photon emission statistics which are necessary for on-demand single photon generation and associated quantum photonics applications [162, 163]. However, unlike diamond, hBN is a layered material and a facile production of nanoparticles from larger hBN flakes is therefore easier. In addition, hBN nanoparticles are biocompatible and display no cytotoxicity at concentrations of up to 0.4 mg/ml [61, 107]. This makes the material appealing for super-resolution imaging [28, 43, 76] in biological environments, and motivates fabrication of fluorescent hBN nanoparticles with diameters below 30 nm, particularly as the solutions discussed above are limited by low brightness or poor photostability. Far-field super-resolution fluorescence imaging techniques such as SMLM require self-blinking fluorescent probes

in the form of photo switchable nanoparticles or recently introduced self-blinking organic dyes [53]. Quantum emitters hosted by hBN have previously been shown to exhibit blinking [43, 153], and hBN nanoparticles may therefore also be suitable probes for SMLM applications.

In this work, we leverage a cryogenic-mediated exfoliation approach [176] to convert hBN powder into hBN nanoparticles with diameters below 10 nm, and as small as ∼3 nm. We characterise the photophysical and photodynamic properties of the particles and show that they can host isolated single photon emitters that are photostable and suitable for super-resolution imaging.

5.2 Experimental Section

5.2.1 Cryo-mediated exfoliation and fracturing process for QDs

Commercially available hBN nanopowder was purchased from Graphene Supermarket. All solvents were purchased from commercially available sources as a laboratory grade and used as supplied without purification. First, 60 mg of hBN powder was soaked in liquid nitrogen (77 Kelvin) for 1 hour, then the powder were immediately dispersed into 20 mL of IPA/H2O (the volume ratio of IPA/H2O is 1:1) to induce thermal shock. The hBN flakes solution was subsequently exfoliated by a commercially available bath-ultrasonication for 4 hours. The concentration of the dispersions were ∼2 mg/mL. After the cryo-mediated exfoliation and fracturing processing, the resultant solution was divided into three plastic vials with equal volume—each vial containing ∼6.5 mL. These solutions were then centrifuged (at 2000 rpm (rounds per minute), 6000 rpm and 12000 rpm, respectively for 30 min to remove big clusters. The supernatants of each sample were then centrifuged for another 30 min. To further separate the nanoparticles from the dispersions, the resulted supernatants were filtered through ultrafine membranes with the pore size of 200-nm.

5.2.2 AFM characterization

For the AFM characterization, the as-obtained nanoparticle solution was diluted and then directly dropped onto a new silicon with thermal oxide layer substrate. The samples were annealed at 850^{o}C in Argon atmosphere for 30 minutes to activate the single photon emitters in h-BN.

5.2.3 Characterization of quantum emitters in h-BN nanoparticles

Optical properties of h-BN nanoparticles were characterized using the lab-built confocal microscope. A continuous wave (CW) 532-nm laser (Gem 532, Laser Quantum Ltd.) was used for excitation. The laser was directed through a half-wave plate, and focused onto the sample using a high-numerical-aperture objective lens (NA = 0.9, TU Plan Fluor 100x, Nikon). The fluorescence of sample was collected by scanning laser across via an x-y piezo scanning mirror (FSM-300, Newport). The collected light was filtered using a 532-nm dichroic mirror (532-nm laser BrightLine, Semrock) and an additional 568-nm long pass filter (LP Filter 568 nm, Semrock). The signal was then coupled into a graded-index fiber, where the fiber aperture served as a pinhole. A fiber splitter was used to direct the light to a spectrometer (Acton SpectraPro, Princeton Instrument Inc.) and to an avalanche photodiodes (SPCM-AQRH-14-FC, Excelitas Technologies) for time-resolved measurement. The laser excitation power was maintained at 300 μW for all the sample characterizations. Correlation measurements were done using a time-correlated single photon counting module (PicoHarp300, PicoQuant). The autocorrelation measurements were not background corrected. Photodynamics of quantum emitters in h-BN nanoflakes was characterized using a widefield inverted microscope.

5.3 Results and Discussions

The original hBN powder was purchased commercially from Graphene Supermarket Inc. with a mean particle size of ∼100 nm. To fabricate smaller nanoparticles, we adopted a recently-developed cryogenic exfoliation technique [176]. The process is shown schematically in figure 1a. Briefly, hBN powder was soaked in liquid nitrogen for an hour and thermally shocked by dispersing it into a room temperature solvent of isopropanol:water (1:1). After the cryogenic treatment, peeling-off of the hBN flakes and small cracks in the intralayer were formed, facilitating the breakdown of hBN powder into small nanoparticles. The solution of hBN nanoparticles was then exposed to an ultrasonication bath for an extended period of time to induce full liquid-phase exfoliation (LPE). The obtained solution was subsequently centrifuged and filtered to remove large hBN clusters from smaller nanoparticles, thus resulting in a narrow size distributions of hBN nanoparticles. Specifically, we prepared three different sample batches with increasing centrifugation speeds: S1 - 2000 revolution per minute (rpm), S2 - 6000 rpm, and S3 - 12000 rpm. To obtain smaller hBN nanoparticles, we filtered S2 and S3 through 200-nm pore polymer membranes. In order to perform optical characterisation, a portion of each batch was dispersed onto a silicon substrate and annealed at 850 ^{o}C in an argon atmosphere to activate quantum emitters embedded within hBN nanoparticles. For convenience, throughout the paper we present the data for S1, S2 and S3 in green, blue and red color, respectively. Due to smaller particle sizes sample S2 and S3 are more transparent while S1 is more opaque because of light scattering from larger particles (fig 5.1).

To characterize the hBN nanoparticles structurally, we drop-casted them onto an ultrathin carbon film supported by a lacey carbon film on a copper grid and imaged them with a transmission electron microscope (TEM) operated using an accelerating voltage of 80 kV. Figure 1c – e show HRTEM images of samples S1, S2

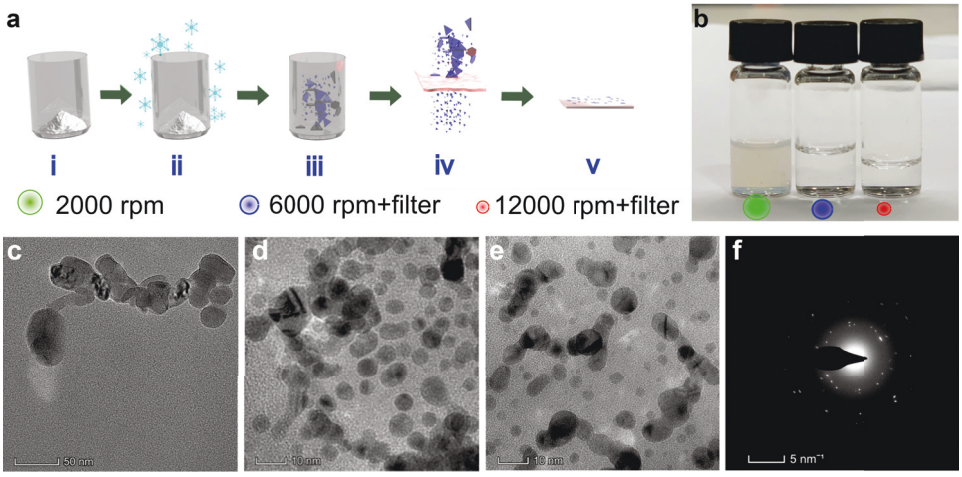

Figure 5.1 : Cryogenic exfoliation of hBN powder into nanoparticles and their characterization. (a) Schematic of the cryogenic exfoliation process. Commercial hBN powder (i) was soaked in liquid nitrogen (ii) for an hour before being dispersed into a room-temperature solvent of isopropanol:water (1:1) (iii) to induce peeling-off and breakdown of the hBN flakes. The resulting hBN nanoparticles were then separated from the larger clusters by centrifugation and filtration through a 200-nm pore membrane (iv). The solution containing small hBN nanoparticles was then spin-casted on marked silicon substrates and subsequently annealed at 850^{o}C in an argon atmosphere (v). (b) Photograph of samples obtained by centrifugation at 2000 rpm (S1), 6000 rpm + 200-nm power filtration (S2), and 12000 rpm + 200-nm power filtration (S3). (c – e) TEM images taken from hBN nanoparticles in samples S1, S2, and S3. The FFT images are in the supporting information, showing a match with hBN lattice parameter of 2.54 $\mathring{A}$. For consistency throughout the main text, the green, blue and red dots are used to represent sample S1, S2 and S3, respectively, unless otherwise stated.

and S3, respectively. With higher centrifugation speeds and the use of a 200-nm pore filter, sample S2 (5.3 $\pm$ 0.8 nm) and sample S3 (3.0 $\pm$ 0.7 nm) exhibit significantly smaller hBN nanoparticle sizes than sample S1 (23.5 $\pm$ 4.6 nm). To confirm the

nanoparticle symmetry and composition, diffraction patterns of the same samples were studied in different spots across the grid (Fig. 1f). In addition, by analyzing the fast Fourier transform (FFT) of the most representative particles (Fig. S1) and based on the distance in the reciprocal space, we found their lattice parameter to be equal to 2.54 $\mathring{A}$, which matches that of hBN [127].

After spin-casting of the hBN nanoparticles onto marked silicon substrates, we used atomic force microscope (AFM) to check their size distributions. Since the lateral size measured by AFM is largely overestimated by tip convolution artifacts, we chose to measure the nanoparticle thickness instead of the lateral size. Figure 2d - f show the nanoparticle thickness histograms. The average nanoparticle size is 120 $\pm$ 46 nm, 21 $\pm$ 11 nm, and 5 $\pm$ 1 nm for samples S1, S2, and S3, respectively. The decrease in the nanoparticle size obtained from AFM measurements is in good agreement with that from the TEM measurements—confirming the effectiveness of the centrifugation and filtration processes.

Next, we turn to optical properties of the nanoparticles. We start with their spectral properties and the presence of quantum emitters, and then characterise their temporal photodynamics. Optical measurements were performed using a 532 nm excitation laser. The fluorescence signal was then analyzed by a spectrometer, and a Hanbury Brown and Twiss (HBT) setup to confirm the presence of quantum emitters.

Figure 5.3 (a – c) show five representative spectra taken from each of the three samples. All spectra exhibit sharp lines—attributed to the zero-phonon lines (ZPL), and some broader peaks red-shifted from the ZPLs—regarded as phonon sideband (PSB) transitions. As expected, spectra taken from sample S1 show, in some cases, multiple ZPLs and PSBs, due to the larger particle sizes and larger quantities of material probed by the excitation laser. On the other hand, spectra from samples S2

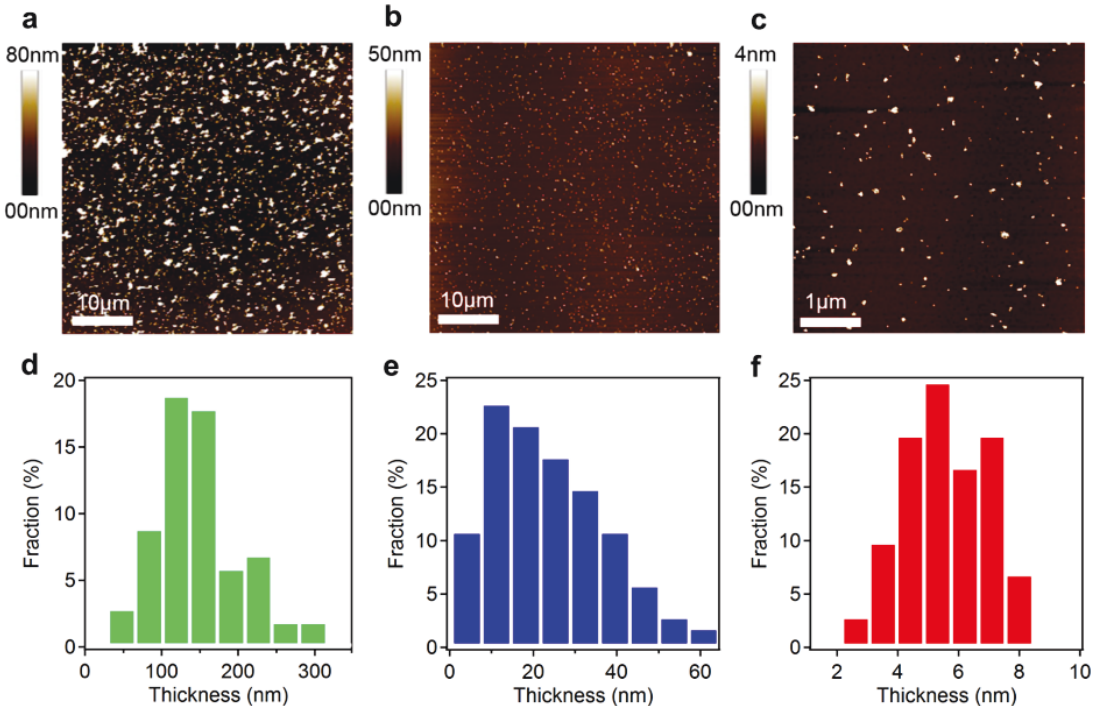

Figure 5.2 : Size distributions of hBN nanoparticles. (a – c) AFM images taken from samples S1, S2, and S3, respectively. (d - f) Thickness histograms of hBN particles in samples S1, S2, and S3, respectively.

and S3, obtained with higher centrifugation speeds and a filter, typically contain a single ZPL with a correlated PSB. Additional statistics on the emission wavelengths is shown in Fig. S2.

Figure 5.3 show the corresponding second order autocorrelation measurements, $g^{(2)}(\tau)$, that can confirm whether the probed luminescence originates from single emitters. An antibunching dip at zero delay time, $g^{(2)}(0)$, of less than 0.5 is indicative of single photon emission characteristics. For sample S1, that is larger in size and hence likely to include multiple emitters in any single measurement, only a few true single emitters were observed, with an average $g^{(2)}(0)$ value of $\sim 0.5 \pm 0.21$. However, most of the emitters probed in samples S2 and S3 were in fact single point defects. Sample S3 exhibited only single emitters with an average value of $g^{(2)}(0)$

$\sim 0.26 \pm 0.10$ with no background correction. The histograms of the dip values (Fig. 3g – i) further confirm this observation, with sample S3 showing highest single photon purity.

To analyze the photodynamic properties of the hBN nanoparticles prepared by cryogenic exfoliation, we use a wide-field SMLM approach that was recently applied to characterization of dense optically-active defects in hBN monolayers [28, 43, 153]. Such wide-field SMLM analysis enables rapid analysis of much larger numbers of particle than scanning confocal imaging. A successful demonstration of an SMLM-based technique on hBN nanoparticles also validates their potential use as fluorescent markers for biological applications.

Given this motivation, we focus on samples S2 and S3 as they possess particle sizes that are appealing for fluorescence probes. The solutions of hBN nanoparticles were first drop-casted/spin-coated onto glass coverslips and dried on a hotplate. The samples were then imaged using a 561 nm excitation laser in a widefield illumination mode (with an illumination power of $\sim$150 W/cm^2). Emission from optically-active defects in hBN nanoparticles is collected by a 100x oil-immersion microscope (Numerical Aperture $\sim$ 1.4) and projected onto an EMCCD camera with a projected pixel size of 105 nm. We observed localized blinking photoluminescece emission from individual diffraction-limited spots on the coverslip, which we attribute to the emission from individual hBN nanoparticles (sample S2) as shown in fig. 4a (widefield). Tuning the particle concentrations during drop-casting, we optimize the density of emitters on coverslips, to achieve large coverage while allowing straightforward localization of single hBN nanoparticles within diffraction-limited spots. Fitting the emission intensity from individual emitters on successive frames by 2D gaussian profiles allows the reconstruction of a super-resolved image (see Fig. 4a, SMLM).

To obtain the emission dynamics of individual emitters, we analyse localization

events throughout successive frames. The intensity of individual emitters is traced through the whole image stack, assuming that emitter is OFF (non-emitting) when it is not detected by the localization algorithm and ON when it is detected within the radius of its localization precision. A typical intensity trace for one of the localized emitters is shown in Fig. 4b, showing successive ON-OFF events.

Analyzing such events for every localized emitter, we obtain the distribution of ON and OFF times for the emitters in samples S2 and S3 (plotted on a log-log scale in Fig. 3c). The distribution follows a well-defined power-law scaling with $P(t_{ON/OFF}) \sim t^{\alpha-ON/OFF}$), consistent with recent characterization of blinking kinetics of emitters in hBN monolayers [28]. We do not observe any significant differences between samples S2 and S3, but the power-law differs for ON and OFF times, with $\alpha_{ON} \approx$ -2.0 and $\alpha_{OFF} \approx$ -1.5.

Finally, we plot in Fig. 4d the histogram of the number of blinking events per particle detected during the whole acquisition period (2.5 minutes) for both samples. We observe a broad distribution in the number of blinks. A significant proportion of emitters blinking only few times, possibly due to irreversible photobleaching, while some emitters demonstrate repeatable and consistent blinking throughout the acquired image stack. This implies that the produced hBN nanoparticles are indeed suitable as labels for SMLM.

5.4 Conclusions

In conclusion, we demonstrated the fabrication of hBN nanoparticles as small as 3.0 ± 0.7 nm. The particles contain fluorescent point defects that act as photostable single photon emitters. The emitter photodynamics were analysed by SMLM, which demonstrates their potential use as fluorescent markers for bio-imaging applications. The facile nanoparticle production method, together with their favorable optical properties and the established biocompatibility of hBN make this system a promising

platform for super-resolution imaging and quantum sensing applications.

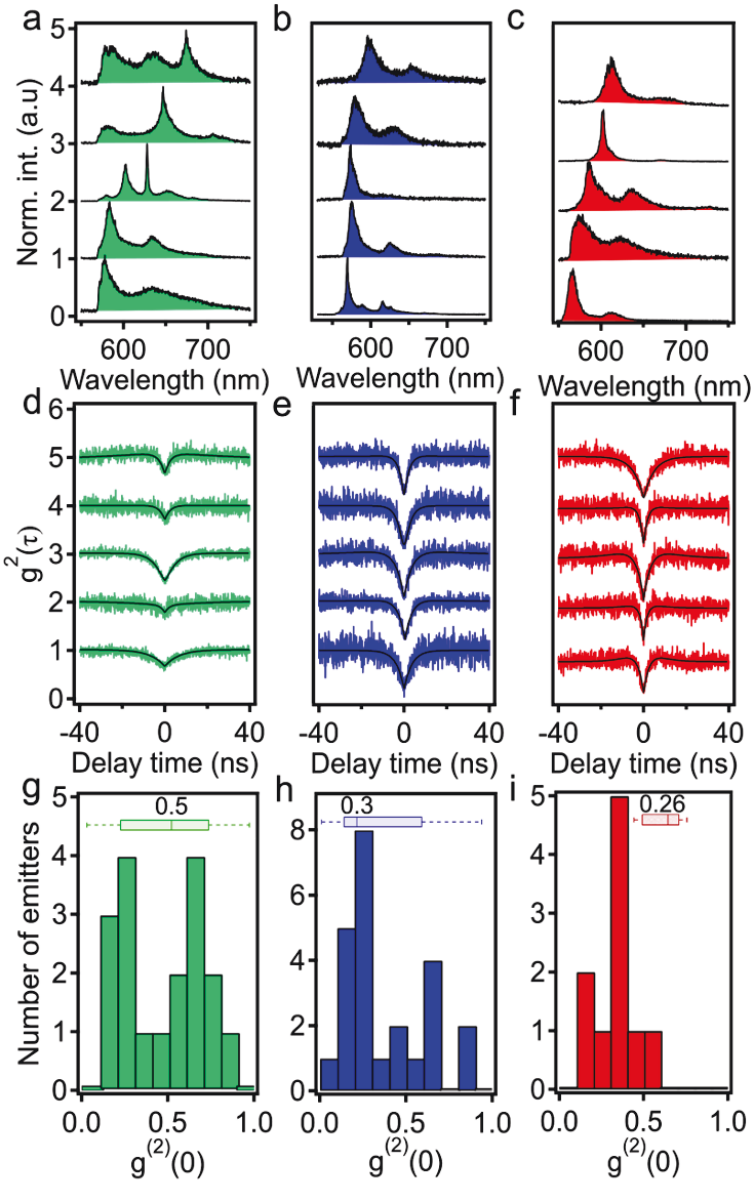

Figure 5.3 : Optical properties of quantum emitters in hBN nanoparticles. (a – c) Three sets of five representative spectra, each set taken from samples S1, S2, and S3, respectively. (d – f) Three sets of five representative second-order autocorrelation functions, each set recorded from samples S1, S2, and S3, respectively. (g – i) Histograms of antibunching dip values extracted from 18 spots in sample S1, 24 spots in sample S2, and 10 spots in sample S3. A value below 0.5 indicating a quantum emitter. All the measurements were taken with a 568-nm long-pass filter in the collection path at room-temperature. Insets represent the median values and standard deviations of antibunching dips measured from samples S1, S2 and S3, respectively.

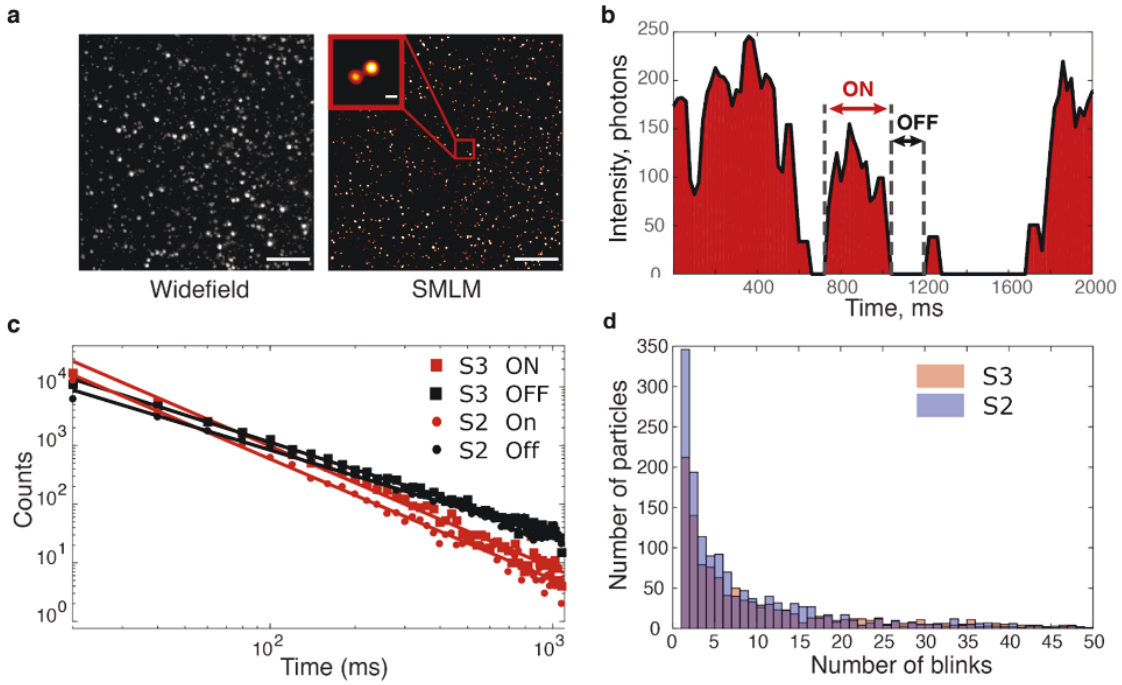

Figure 5.4 : Photodynamics of quantum emitters obtained using Single-Molecule Localization Microscopy (SMLM) on samples S2 and S3. (a) Widefield (max intensity projection) and reconstructed image of an area in sample S2, based on 6000 frames, processed using Thunderstorm. Scale bar: 5um. The inset shows a zoom of two emitters in the super-resolved image (Scale bar: 100 nm) (b) Timetrace of a localized emitter, derived from the localization table from (a), and an example of the detected ON and OFF times. Exposure time: 20ms. (c) Distribution of ON/OFF times in the localized emitters, calculated from the analysis of their timetraces, as shown in (b). (d) Histogram of the number of blinks (transitions from OFF to ON state and back) per emitter, detected throughout the entire acquisition.

Chapter 6

Enhanced Emission from WSe_2 Monolayers Coupled to Circular Bragg Gratings

As discussed in Chapter 2 section 2.5 , 2D TMDCs possess superior properties and are of great promise for future optoelectronic applications. Especially in photonics, these atomic materials are promising to be used as a versatile light-emitting source. However, the PL emission efficiency of such 2D materials is much lower than expected value of direct gap materials, limiting the widespread applications of TMDC based devices. Novel hybrid approaches have been devised to take advantage of properties of TMDCs and their compatibility with CMOS technology, including ultra-sensitive photodetectors and low threshold lasers. Therefore, in this chapter, we present the integration between TMDC and an optical grating structure to achieve a hybrid device with seven folds of PL enhancement, which could help to bridge the gap between Lab and the Real World.

The idea of the work was from Zai-Quan Xu and Jin Liu (SYSU). The photonic structures were designed and fabricated by Rongbin Su, Zhuojun Liu, and Jin Liu (SYSU). Monolayer WSe2 was obtained from Yi Wan and Lain-Jong Li (KAUST). The optical measurements and analysis were done by Ngoc My Hanh Duong, with some assistance from Mehran Kianinia, Zai-quan Xu, Sejeong Kim, Carlo Bradac, and Alexander Solntsev. The schematic illustration was designed by Toan Trong Tran. All the authors discussed and wrote the manuscript.

6.1 Introduction

Atomically-thin transition-metal dichalcogenides (TMDCs) are an emerging class of materials with unique optoelectronic properties [44]. They possess a direct bandgap [194], exhibit very large exciton binding energies [58] and strong spin orbit coupling [84]. In addition, a very unique aspect of these materials, is a strong spin valley polarization (due to their natural inversion symmetry breaking), that allows optical readout [68, 190, 191] and electrical modulation even at room temperature [136, 183, 195].These properties elevate TMDCs as promising candidates for applications in nanophotonics, quantum optics, magneto-optics and valleytronics.

Most of the promising applications of TMDCs—such as ultra-low-threshold lasers [182], light emitting diodes (LEDs) [135, 195], photodetectors [187] and spin valley readout rely on efficient extraction (or absorption) of photons by the TMDCs. Given the monolayer nature of the material, light absorption can be challenging, and an emerging topic of research relies on a hybrid integration of TMDCs with photonic [25, 181, 182], or plasmonic cavities [18] to enhance light-matter interaction.

Circular bragg grating (CBG) cavities, are structures which are rather simple to fabricate and produce high photon extraction rates and efficient Purcell enhancement [12, 154]. The CBG is therefore particularly attractive and promising for integration with 2D materials. The basic structure consists of a wavelength-scale center disk surrounded by periodic concentric rings, that together act like an antenna. It collects and couples the incident light into the wavelength determined by the cavity resonance which itself can be spectrally tuned. The circular grating operates under the second-order Bragg condition, and provides reflective feedback to the cavity and near-vertical upwards scattering. The emitted photons are firstly captured by the low-Q cavity formed by the central disk and the concentric circular grating, and are then scattered out of the plane by the circular grating with a

convergent, far-field pattern for efficient photon collection by the objective.21

Here, we demonstrate efficient coupling between a monolayer of tungsten diselenide (WSe_2), and a CBG. A monolayer WSe_2 is transferred and spatially aligned with the photonic CBG cavity. When coupled, we observe an enhancement of sevenfold in the excitonic emission from the hybrid WSe_2–CBG device. We also observe a Purcell enhancement of ~ 4, as deduced from measuring the time-resolved photoluminescence (PL).

6.2 Experimental Section

6.2.1 Numerical modelling

Numerical calculations are performed using a commercial solver, Lumerical software. Refractive indices of Si_3N_4 and SiO_2 are set to 2.02 and 1.45, respectively. The parameters for silicon are taken from the software's build-in material database, Si (Silicon)–Palik. The structure comprises of a 180-nm Si_3N_4 CBGs, a 750-nm SiO_2 and a Si substrate. The CBG structure consists of a central disk with a radius of 325 nm and 16 concentric circular rings featuring a period of 450 nm and a trench of 90 nm. The simulation volume is 16.85 x 16.85 x 1.76 μm^3 with a non-uniform mesh of mesh accuracy 4. A dipole is placed 0.5 nm above the CBG as an exciting source with wavelengths ranging from 720 nm to 780 nm. A field monitor at the center of Si_3N_4 CBGs is set to record the near field and a power monitor 100 nm above the CBG is used to record up-going near field for performing near- to far-field projections. A transmission box consisting of 6 power monitors in 6 directions are used for calculating the total radiant power. The collection efficiency calculated based on a NA = 0.9 objective is obtained from the ratio of up-going power in 64 degree azimuthal angle to the total emitted power.

6.2.2 Design and fabrication of CBGs

750-nm SiO_2 and 180-nm Si_3N_4 are deposited on a silicon wafer at 300^oC in an inductively-coupled plasma chemical vapour deposition. The patterns of the CBGs are defined by E-beam lithography with a positive tone resist (ZEP 520A) in a 100-KeV writer (Vistec EBPG 5000+) and transferred into the Si3N4 layer using a CHF_3-O_2 based try etch process. Finally, the e-beam resist is removed by a 1165 remover solution in an ultrasonication bath.

6.2.3 Optical characterization

The optical characterizations of the structures were carried out with a lab-built scanning confocal microscope. A continuous wave (CW) 532-nm laser (Gem 532, Laser Quantum Ltd.) was used for excitation. The laser was directed through a Glan-Taylor polarizer (Model No. DGL10, Thorlabs Inc.) and a half-wave plate, and focused onto the sample using a high-numerical-aperture objective lens (NA = 0.9, TU Plan Flour 100x, Nikon). The laser was scanned across the sample using an x-y piezo scanning mirror (FSM-300, Newport). The collected light was filtered using a 532-nm dichroic mirror (532-nm laser BrightLine, Semrock) and an additional 568-nm long pass filter (LP Filter 568 nm, Semrock). The signal was then coupled into a graded-index fiber, where the fiber aperture served as a pinhole. A fiber splitter was used to direct the light to a spectrometer (Acton SpectraPro, Princeton Instrument Inc.) and to an avalanche photodiodes (SPCM-AQRH-14-FC, Excelitas Technologies) for time-resolved measurement. To avoid sample damage, the laser excitation was performed at low power (¡50 μW). Lifetime measurements were performed using a Fianium Whitelase Supercontinuum laser (NKT Photonics) coupled into a fibre. The laser was collimated and went through a short-pass filter (568 nm, Samrock) to filter the 532-nm light. The repetition rate was kept at 20 MHz for all the experiments. Samples for radiative lifetime measurement were all

measured at 77 K in vacuum. The data were fit by using a double exponential function. Temperature-dependant experiments were also performed using a closed-cycle refrigerating system cryostat cooled with liquid nitrogen.

6.3 Results and Discussions

A schematic illustration of the WSe_2 monolayer placed on top of the CBG is shown in Figure 1a. WSe_2 flakes were grown by chemical vapour deposition (CVD) [63]. The thickness of the flakes was measured to be ~ 0.7 nm using atomic force microscope (AFM), confirming it to be a monolayer (Fig. 1b) [186, 187]. The typical lateral length of the WSe_2 is ~ 50 μm. The monolayer was then transferred [186] onto a silicon nitride (Si_3N_4) substrate, which had been patterned with shallow CBG trenches. The large area of the WSe_2 allows for high precision in the positioning of the flake in the center of the CBG without requiring sophisticated alignment procedures. The emission from the flake is uniform across its entirety, which enables the easy and direct comparison of PL emission for the same WSe_2 monolayer from regions in the center of the CBG and completely away from it.

A false-colour scanning electron microscopy (SEM) image of the fabricated WSe_2-CBG structure is shown in Figure 6.1c. The yellow regions correspond to the WSe_2 monolayer, which a part completely covers the centre of the CBG marked by the red circle: this is essential for coupling the emission from the WSe_2 to the CBG photonic structure. Note that the flake also extends outside of the grating structure (marked by blue circle) which, as mentioned above, is ideal for direct comparison of photon emission rate and directionality for the on-center and out-of-center (off-grating) cases. Other marked areas with cyan and green will be discussed later.

We design the CBG to match the emission frequency of the WSe_2 by using a commercial software package (Lumerical Solutions, Inc.) and simulate the intrinsic optical properties of the CBG with an electric dipole source located on top of the

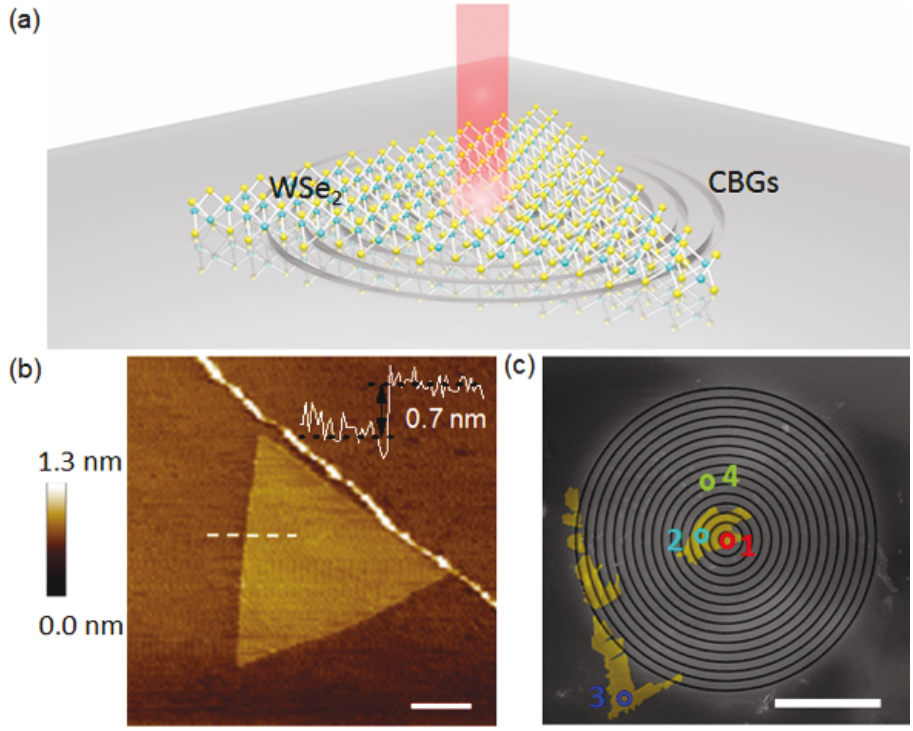

Figure 6.1 : a) Schematic of a monolayer WSe_2 on top of a circular Bragg grating (CBG) structure. b) Atomic force microscope (AFM) image of the WSe_2 monolayer. The height profile (inset) extract from the white dashed line shows the step at the substrate/WSe_2, corresponding to thickness of the flake, to be ∼0.7 nm. c) False-colour scanning electron microscope (SEM) image of the WSe_2-CBG structure with specified positions of WSe_2 on the center (1), near center (2), off the gratings (3) and on the gratings but not at center area (4). Scale bar in (b) and (c) is 5 μm.

center of the structure by 3D finite-difference time-domain (FDTD) method. The large index contrast at the Si_3N_4-air interface leads to strong reflections and out-of-slab-plane scattering, resulting in very high fields at the center (Fig. 6.2). The Purcell factor is obtained from the ratio of total radiant power of a dipole in CBG to that of a dipole in vacuum by summing the transmitted power from a small box encircling the dipole. A resonant peak is clearly observed at 750 nm with the maximum Purcell factor of ∼16 due to Bragg reflection and cavity resonant

enhancement. Other peaks at longer wavelengths are oscillations near the Bragg reflection band-edge (Fig. 6.2b).

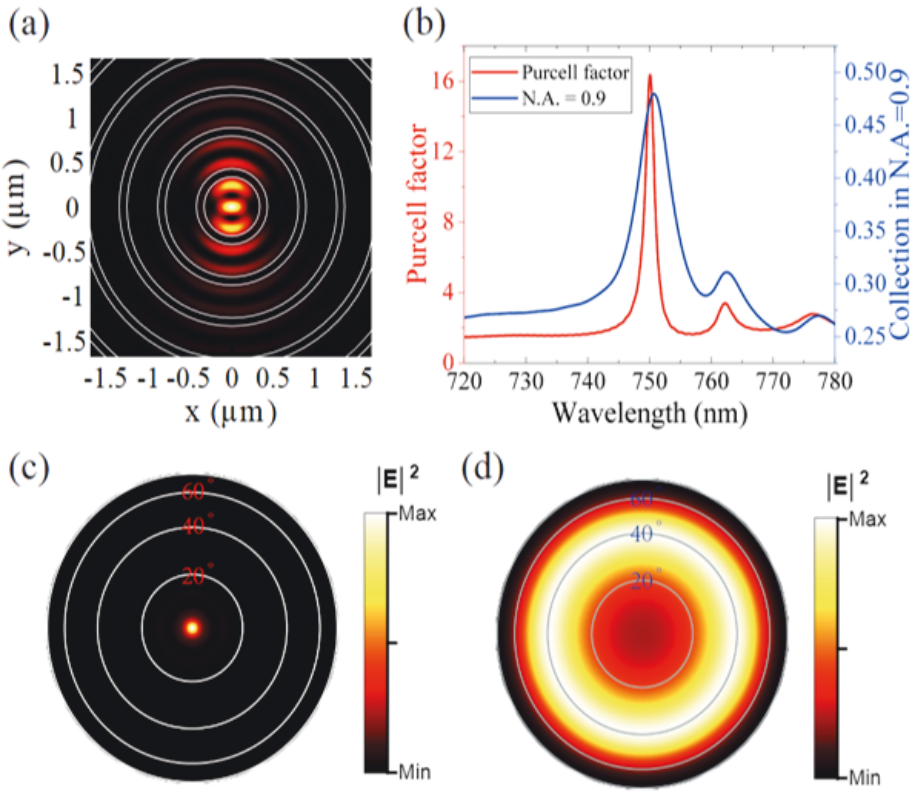

Figure 6.2 : a) Electric field intensity in the XY-plane superimposed to structure outlines. b) Purcell factor (left axis, red) and collection efficiency (right axis, blue) calculated using an objective with NA = 0.9 for a dipole locate in the center of the structure. The peak at ∼750 nm is a cavity resonant mode and the others at longer wavelength are oscillations near the Bragg reflection band-edge. c, d) Far-field polar plots at the cavity resonant wavelength, 750 nm, on (c) and off (d) the CBG.

The collection efficiency is calculated by the ratio of radiant power collected by the objective to the total power. The numerical aperture (NA) of our objective is 0.9 (corresponding to 64 degree azimuth angle in far-field). As shown in Fig. 6.2b, a collection efficiency up to 0.5 can be achieved near the resonant wavelength as the light propagating in the Si_3N_4 slab is efficiently scattered out of plane within

a relatively small divergence angle by CBGs. The slight offset of the wavelengths maxima for the Purcell factor and the collection efficiency is due to the asymmetric structure in the z-direction. Reflection at the SiO_2/Si interface significantly modifies the far-field pattern hence changing the enhancement in collection efficiency. Figures 6.2c and 6.2d display the far-field patterns of a dipole emitting on and away from the CBG structure, respectively. Most of the upward emitted photons are confined within an azimuthal angle of 20 degrees for the dipole on the CBG structure. On the contrary, the dipole away from the centre of CBG structure (also knowns as off-grating) shows a donut-shape, far-field emission with a divergent emission angle wider than 60 degrees.

To evaluate the coupling of the WSe_2 emission to the CBG, optical characterizations of the device were performed with a lab-built scanning confocal microscope (see methods)[165]. In brief a 532 nm, continuous-wave laser is used to excite the WSe_2 using an air-objective with high numerical aperture (NA=0.9) and 100x magnification. The photo-emission is collected via the same objective and filtered by a 568 nm long-pass filter (to remove the excitation laser) and is coupled into a spectrometer through a multimode optical fibre. An optimization of spectral overlapping is explored for optimal coupling and enhanced emission. A set of CBGs is fabricated with modes ranging from 728 to 755 nm, and the resonant wavelength is examined, as show in Fig 6.3.

We choose a specific CBG that matches the resonance of the WSe_2 emission, as shown in fig 3a. The resonant mode of the CBG is visible at $\sim$756 nm, consistent with the simulation results discussed above. The measured quality factor is Q $\sim$ 120, defined as $Q = \lambda/\Delta\lambda$, where λ is the cavity resonance wavelength and $\Delta\lambda$ is the full width at half maximum (FWHM) of the resonance peak.

Figure 6.4b shows the PL emission from the hybrid WSe_2-CBG device. We

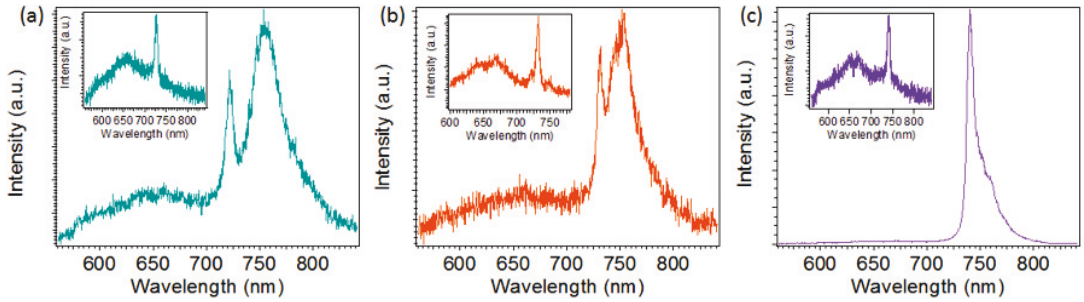

Figure 6.3 : PL emission from WSe_2 integrated with different CBG structures. Emission of WSe_2 on CBGs with different resonant mode at 728 nm (a), 732 nm (b) and 741 nm (c). The insets show the CBG's optical modes. All the measurements were performed in ambient conditions.

investigate the PL enhancement by measuring PL of WSe_2 in the center of the CBG compared with that from WSe_2 away from the center of the CBG and used as the reference value (see fig 6.1c). The emission from the WSe_2 area coupled to the cavity (red curve) is $\sim$ 4.5 times higher than that of the pristine uncoupled WSe_2 (blue curve). The circles in figure 1c indicate where the on- (red circle) and off-grating (blue circle) PL measurements were carried out. Notably, the spectral shape of the WSe_2 emission is different at the center of CBG due to the coupling of the WSe_2 PL emission to the CBG resonant mode.

The PL emission from the WSe_2 flake is temperature-dependent [50, 188] and has been shown to be higher at lower temperatures [62] owing to the suppression of the non-radiative decay components and the reduction in exposure to O_2 and H_2O—all resulting in lower radiative emission from WSe_2 [159]. Thus, we perform a low-temperature PL measurement on the WSe_2-CBG samples in vacuum to study the coupling between the WSe_2 and the CBG at 77K.

The PL emission from WSe_2 on-centre and off-grating is shown in Figure 6.4c. A higher, 7-fold enhancement is observed at cryogenic temperatures from the on-

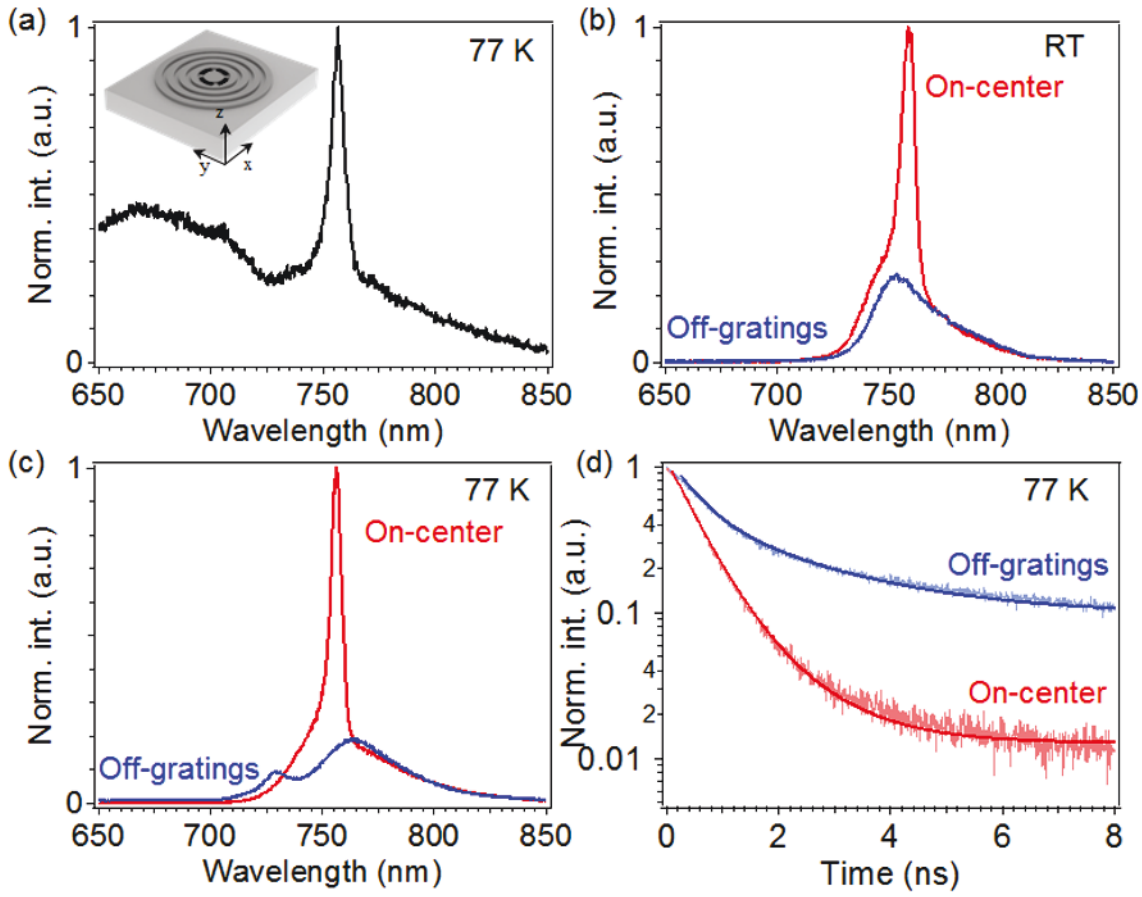

Figure 6.4 : Optical characterizations of the WSe_2-CBG hybrid structure. a) CBG mode measured from a bare CBG at 77K with 532 nm excitation. Inset: a schematic of the CBG structure with a black circle showing the place the resonance spectrum is collected. b, c) PL emission comparison for WSe_2 on-center (red line) and off-grating (blue line) measured at room temperature (b) and 77K (c). d) Time-resolved PL measurement from WSe_2 on center (red circle) and off-grating (blue circle) at 77 K.

center, coupled WSe_2. To further characterize the nature of the enhanced emission, time-resolved PL measurements were carried out for the on-centre and off-grating WSe_2 using a 532 nm, pulsed laser excitation (repetition rate 40 MHz, pulse width 4 ps) at 77K. The measured curves are shown in Figure 3d both for the on-center (red) and off- grating (blue), confirming the reduction in the WSe_2 lifetime after coupling

with the CBG's resonant mode. The curves are fitted with a double-exponential function, where the first exponential is fixed and determined directly by measuring the instrument response of our setup. The reduction in lifetime of WSe_2 is 4 times (i.e. Purcell enhancement of ~ 4), approximately 1.8 times lower than the overall emission enhancement. The difference is attributed to the increased absorption of light in the CBG, as well as a directional emission from the CBG that together contribute to the increased emission intensity. As expected, the room temperature lifetime reduction is lower (see fig. 6.5), resulting also in a lower overall enhancement.

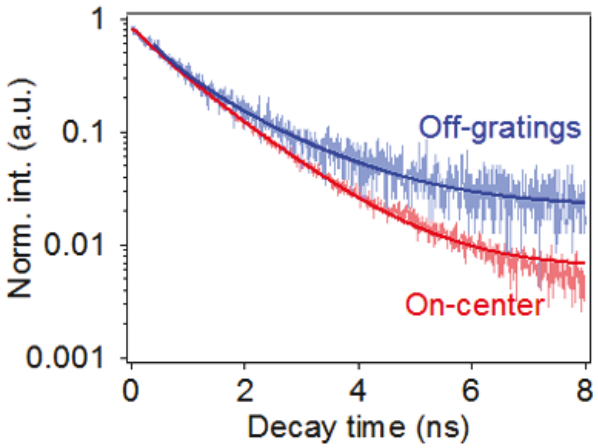

Figure 6.5 : Lifetime of WSe_2 coupled to the bullseye structure at Room temperature with on-center (red line) and off-gratings (blue line). A Purcell enhancement of $\sim$1.7 is calculated based on the lifetime extracted from the curves.

To further understand the temperature-dependent excitonic properties of WSe_2 coupled to the CBG, we systematically analysed temperature-resolved PL spectra of the WSe_2-CBG hybrid structure. Figure 6.6a and 6.6b show the PL spectra collected from WSe_2 on and off the CBG center at temperatures ranging from 77 to 300K. For the uncoupled WSe_2 monolayer, we observed spectral splitting at temperature below 120 K (Fig. 6.6b), as reported elsewhere [50, 188, 198]. The higher energy peak is the neutral exciton X^0 with a typical PL emission at $\sim$ 729 nm, whereas the

lower-energy peak is the trion peak, labelled X*, and emits at $\sim$ 763 nm. The trion X* emission peak is rather broad, it displays an exponential low-energy tail and it is thermally quenched for temperatures above 120 K. These features observed for the X* peak are usually considered evidence for disorder-related effects [62].

At 77 K, the trion peak dominates the PL emission spectrum (Fig. 4a). The emission spectrally matches the resonant mode of the CBG at $\sim$ 756 nm, hence resulting in the observed seven-fold enhancement in PL intensity. However, the trion's emission intensity steadily decreases and red-shifts from $\sim$765 nm to $\sim$783 nm at temperatures above 77 K (Fig. 4b) due to thermal activation or recombination into free exciton. We thus attribute the higher enhancement at 77 K to a combination of effects: the aforementioned increased WSe_2 PL and the better spectral matching between the WSe_2 trion and the CBG resonant mode. Figure 4c shows the overall enhancement at resonant wavelength from the coupled and the uncpoupled case as a function of temperature. as explained above, the enhancement at 77K is much stronger, due to preferential spectral match of the cavity mode and the trion emission.

Finally, we measure the optical spin valley contrast at room temperature. The detailed setup is described in Figure A.1. The degree of PL polarization with the helicity parameter is defined as:

$$\rho = \frac{I(\sigma^+) - I(\sigma^-)}{I(\sigma^+) + I(\sigma^-)} \tag{6.1}$$

where I(σ^+) and I(σ^-) are right and left circularly polarized emission, respectively. There is only a small ($\rho\sim$ 3.6%) contrast between the σ^+ and σ^- excitation for uncoupled WSe_2, as expected for WSe_2 [191] (Fig. 6.7a). Note that our measurement error due to non perfect circularly polarized beams due to various optical elements is estimated at $\sim$ 10%. A few micron away from the CBG center (Fig. 6.7b) the contrast is still within the measurement error range ($\rho \sim 8\%$). However,

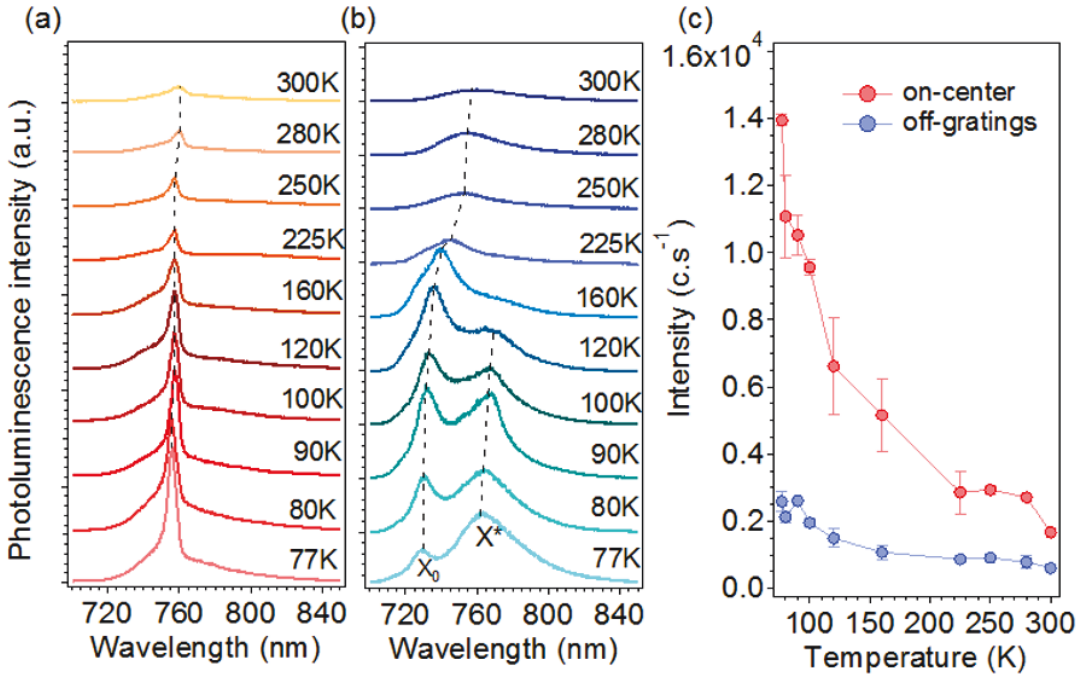

Figure 6.6 : Temperature-dependent emission characterization of WSe_2-CBG hybrid system. a) PL emission of WSe_2 on the center of the CBG structure and b) off-grating measured from 300K to 77K. The neutral exciton (X0) and the trion peak (X*) are labelled. c) Temperature-dependent PL intensity at resonant wavelength of CBG from WSe_2 on-center of the CBG (red circles) and off-gratings structure (blue circles).

when efficiently coupled to the CBG, the contrast changes dramatically. As the excitation is moved to ~ 1 μm away from the CBG center the contrast increase to $\rho\sim$ 17% (Fig. 6.7c), and then reaches extremely high $\rho \sim 43\%$ at the center of the CBG (Fig. 6.7d). to the best of our knowledge, this is the largest valley contrast that has been measured for WSe_2.

This significantly enhanced contrast may be explained by the way in which CBG structures affect polarization. Previous works studying reflection [124] and cathodo-luminescence (CL) [123] from CBGs have shown that ideal CBG excited exactly in the center has a fairly simple symmetrical output polarization distribution. The

picture however changes dramatically if the excitation is placed even slightly off-center. CL can be a good qualitative predictor of PL, and it shows that moving the excitation off-center within the first CBG ring leads to a very complex distribution of left-hand-side and right-hand-side circular polarizations with respect to emission angles [123]. Taking into account limited collection angle, this effect may be responsible for a strong enhancement of the contrast between the σ^+ and σ^- emission, when WSe_2 is excited slightly off-center of the CBG. This effect is also expected to diminish when moving several rings away from the CBG center, as the CBG modes are no longer efficiently excited, and the constructive interference from multiple CBG rings diminishes. This is exactly what we see in the experiment, as the contrast diminishes with the increasing distance from the CBG center.

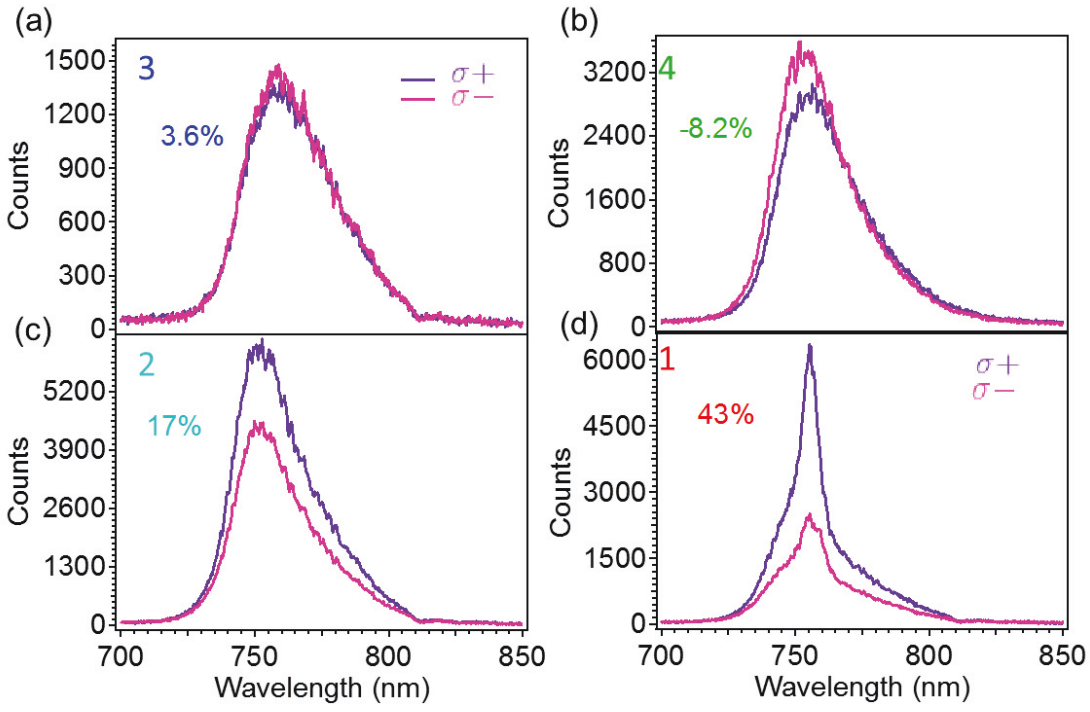

Figure 6.7 : a–d) Emission from WSe2 at different spots (same ones of figure 1c) under circularly-polarized excitation at 532 nm. The σ^+ and σ^- PL components are measured at each of the spots with the corresponding values for the contrast ρ listed on each graph.

WSe_2 also has a host of mechanisms such as excitation of trions [30] and up-conversion PL [44] that can lead to a drastic σ^+ / σ^- contrast increase. Although the wavelengths in these demonstrations differ somewhat from our experimental conditions, effects like these may also play a role in the contrast increase near the center of the CBG if any WSe_2 emission modes with a strong polarization dependence couple efficiently to the CBG modes. From the temperature resolved experiments shown above, we do have a preferential coupling of the trion emission to the CBG mode. While at this point it is too early to pinpoint the exact mechanism leading to the contrast increase on the CBG, our results indicate that CBGs is a very useful platform for the future development of valleytronics based on WSe_2 [104].

6.4 Conclusions

To conclude, we have demonstrated enhanced emission from monolayer WSe_2 integrated onto a circular Bragg grating structure. Approximately a three-fold enhancement at room temperature and a seven-fold enhancement at 77 K are observed. By measuring temperature- dependent emission of WSe_2, we have evaluated the enhancement mechanism of WSe_2/CBG hybrid system. Finally, we show that an optical readout of the spin valley is possible for the coupled WSe_2-CBG system, with a record contrast exceeding 40%. Our results will contribute to the development of integrated nanophotonics platforms involving 2D materials, optical cavities and valleytronics.

Chapter 7

Summary and Outlook

Here, the content of this thesis are reviewed chapter by chapter. After that, an outlook on future prospects and continuous experiments are given.

7.1 Summary

Chapter 2 overviewed fundamental aspects of 2D materials, including TMDCs and single photon emitters in hBN.

In Chapter 3, the generation of single photon emitters in hBN has been introduced. In this work, we found that MeV irradiation can significantly enhance the formation of SPEs in hBN, without the necessity for a further annealing step. Upon irradiation, SPEs are found to distribute in the flat areas of the flake where there is no clear grain boundaries or wrinkles. Our results are promising to develop a reliable procedure for engineering SPEs in hBN at the nanoscale. It also paves the way for deterministically creating SPEs in hBN flakes by using the combination of high energy electron irradiation and lithography mask on the samples.

In Chapter 4, we built a hybrid quantum system with hBN SPEs as the quantum light source. By precisely positioning an hBN nanoflake hosting a suitable quantum emitter onto an AlN waveguide, the quantum emission was coupled and guided through the waveguide at the designed wavelength. This experiment paves the way for using hBN emitter in integrated quantum networks. The collection efficiency is modest of 1.2 %; however, it is in line with the simulated coupling efficiency of 6.3 % estimated for the system (using FDTD). This result opens doors for

further optimization to improve the coupling efficiency, for instance, by engineering the immediate dielectric environment of the emitters through capping with a third material, engineering the spectral characteristics of the emitters on demand, or precise spatial positioning the light source on the waveguide.

In Chapter 5, the physical size of hBN flakes was reduced to the nanometer regime by employing the cryogenic mediated exfoliation. After centrifugation and filtration, we obtained nanoparticles with a significantly small size of below 5nm. Interestingly, these nanoparticles demonstrated desired optical properties that make them suitable for super-resolution imaging. The photodynamic properties of these nanoparticles were also analyzed by SMLM, which shows that hBN nanoparticles are indeed promising to use as fluorescent markers in bio-imaging applications.

In Chapter 6, we demonstrated the integration of monolayer WSe_2 in silicon-based circular Bragg's grating structure and realized enhanced and directional emission from monolayer WSe_2. We deterministically positioned monolayer WSe_2 on the center of the grating structure to obtain spatial matching. By aligning the resonant mode supported by the gratings with the emission from the charged excitons emission in WSe_2 at cryogenic temperature, we obtained the PL enhancement up to 7 folds and a narrow light emission from WSe_2 that coupled to the cavity. We also demonstrated that the CBG structure could effectively increase the spontaneous emission rate from coupled WSe_2, thus offering the feasibility for ultra-fast signal processing. Finally, we achieved a valley polarization of the hybrid system, with a record contrast of 40 %. This hybrid system is, therefore, appealing for optical spin valley readout applications.

7.2 Outlook

Based on the results found in this thesis, we envision future experiments in various directions. Two directions for continuous experiments are presented. These

directions are focussed on the research with stabilization of quantum emitters in hBN and the ambitious prospects of Integrated Photonic Circuits.

7.2.1 Stabilization of hBN quantum emitters

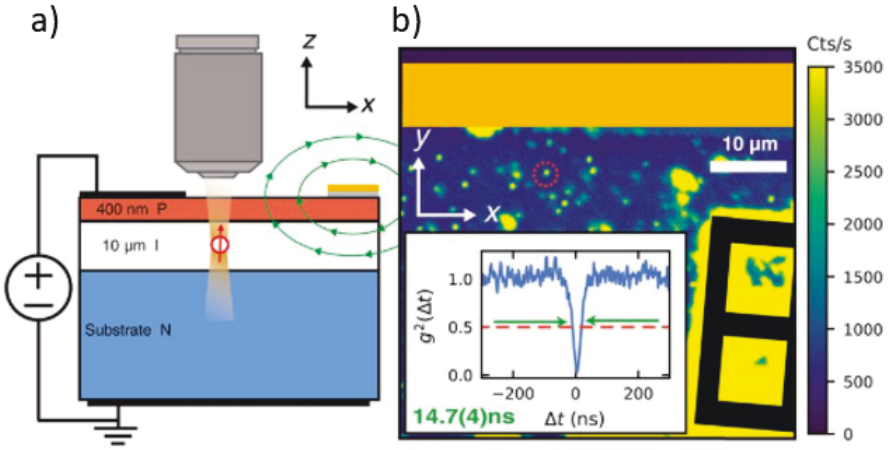

Figure 7.1 : (a)Schematic of the p-i-n device, (b) Confocal PL scan of an example device with isolated emitters sandwiched between two layers (example circled in red), confirmed by autocorrelation (inset) showing $g^{(2)}(0) < 0.5$ (red line) [9]. Adapted with permission from: (a) - [9], (b) - [9].

The presence of ultrafast spectral diffusion proves that phonon coupling is not the major cause of low cohenrent times of hBN quantum emitters [149]. The fast values indicate that fluctuation in defect energy level is caused by charging and discharging of the defect or charge traps in the environment, or photoionized of impurities in the lattice. The low coherent time and the spectral diffusion have seriously hindered the realization of two photon interference and entangled photons from hBN single photon emitters. Also due to hBN two-dimensional nature, the defect is highly exposed to the surrounding environment. Recent development of engineering hBN in large exfoliated flakes can potentially decrease the spectral diffusion by generating a clean environment [24, 42, 90]. However, these methods are impractical as they only focus

on surface modification of the host material. To address this shortage, we propose a method for alleviating the ubiquitous problem of spectral diffusion by engineering the electrical environment surrounding emitters using a classical semiconductor device - a p-i-n junction - as described in reference [9].

7.2.2 Integrated photonic circuits

Due to two-dimensional nature of 2D materials, it is viable to incorporate them into nanophotonic devices. In chapter 4, we presented the significant step to integrate quantum emitter in hBN into an optical waveguide. This is not only important to understand fundamental physics but also make a leap towards scalable on-chip devices. With that in mind, we propose the next step to couple quantum emitter in hBN in waveguide then enhance and purify the emitted light with optical resonators.

Appendix A

Appendix Title

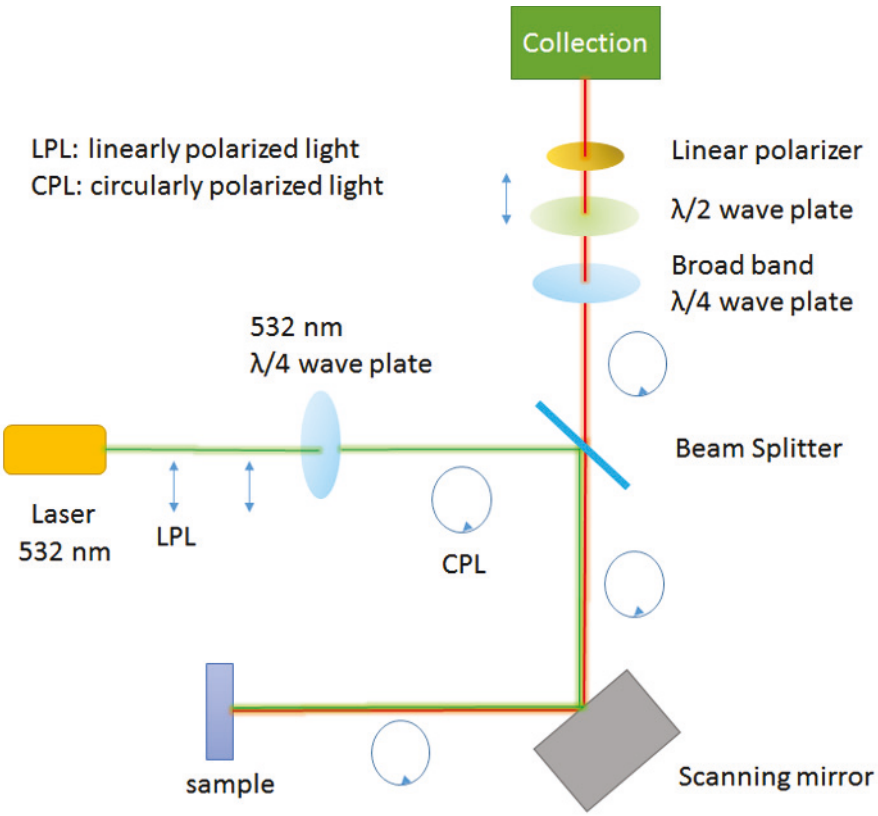

Figure A.1 : Schematic of the polarization-measurement experiment in Chapter 6 .

Bibliography

[1] M. Abdi, J.-P. Chou, A. Gali, and M. B. Plenio, "Color centers in hexagonal boron nitride monolayers: a group theory and ab initio analysis," *ACS Photonics*, vol. 5, no. 5, pp. 1967–1976, 2018.

[2] A. Acín, N. Brunner, N. Gisin, S. Massar, S. Pironio, and V. Scarani, "Device-independent security of quantum cryptography against collective attacks," *Physical Review Letters*, vol. 98, no. 23, p. 230501, 2007.

[3] I. Aharonovich, S. Castelletto, D. Simpson, C. Su, A. Greentree, and S. Prawer, "Diamond-based single-photon emitters," *Reports on progress in Physics*, vol. 74, no. 7, p. 076501, 2011.

[4] I. Aharonovich, D. Englund, and M. Toth, "Solid-state single-photon emitters," *Nature Photonics*, vol. 10, no. 10, p. 631, 2016.

[5] I. Aharonovich and E. Neu, "Diamond nanophotonics," *Advanced Optical Materials*, vol. 2, no. 10, pp. 911–928, 2014.

[6] N. Akopian, N. Lindner, E. Poem, Y. Berlatzky, J. Avron, D. Gershoni, B. Gerardot, and P. Petroff, "Entangled photon pairs from semiconductor quantum dots," *Physical review letters*, vol. 96, no. 13, p. 130501, 2006.

[7] G. M. Akselrod, T. Ming, C. Argyropoulos, T. B. Hoang, Y. Lin, X. Ling, D. R. Smith, J. Kong, and M. H. Mikkelsen, "Leveraging nanocavity harmonics for control of optical processes in 2d semiconductors," *Nano Letters*, vol. 15, no. 5, pp. 3578–3584, 2015.

[8] M. H. Alkahtani, F. Alghannam, L. Jiang, A. Almethen, A. A. Rampersaud, R. Brick, C. L. Gomes, M. O. Scully, and P. R. Hemmer, "Fluorescent nanodiamonds: past, present, and future," *Nanophotonics*, vol. 7, no. 8, pp. 1423–1453, 2018.

[9] C. P. Anderson, A. Bourassa, K. C. Miao, G. Wolfowicz, P. J. Mintun, A. L. Crook, H. Abe, J. U. Hassan, N. T. Son, T. Ohshima *et al.*, "Electrical and optical control of single spins integrated in scalable semiconductor devices," *Science*, vol. 366, no. 6470, pp. 1225–1230, 2019.

[10] M. Atatüre, D. Englund, N. Vamivakas, S.-Y. Lee, and J. Wrachtrup, "Material platforms for spin-based photonic quantum technologies," *Nature Reviews Materials*, vol. 3, no. 5, pp. 38–51, 2018.

[11] S. Barik, A. Karasahin, C. Flower, T. Cai, H. Miyake, W. DeGottardi, M. Hafezi, and E. Waks, "A topological quantum optics interface," *Science*, vol. 359, no. 6376, pp. 666–668, 2018.

[12] C. Bauer, H. Giessen, B. Schnabel, E.-B. Kley, C. Schmitt, U. Scherf, and R. Mahrt, "A surface-emitting circular grating polymer laser," *Advanced Materials*, vol. 13, no. 15, pp. 1161–1164, 2001.

[13] O. Benson, "Assembly of hybrid photonic architectures from nanophotonic constituents," *Nature*, vol. 480, no. 7376, pp. 193–199, 2011.

[14] A. M. Berhane, K.-Y. Jeong, Z. Bodrog, S. Fiedler, T. Schröder, N. V. Triviño, T. Palacios, A. Gali, M. Toth, D. Englund *et al.*, "Bright room-temperature single-photon emission from defects in gallium nitride," *Advanced Materials*, vol. 29, no. 12, p. 1605092, 2017.

[15] S. Bogdanov, M. Shalaginov, A. Boltasseva, and V. M. Shalaev, "Material

platforms for integrated quantum photonics," *Optical Materials Express*, vol. 7, no. 1, pp. 111–132, 2017.

[16] R. Bourrellier, S. Meuret, A. Tararan, O. Stéphan, M. Kociak, L. H. Tizei, and A. Zobelli, "Bright uv single photon emission at point defects in h-bn," *Nano letters*, vol. 16, no. 7, pp. 4317–4321, 2016.

[17] R. H. Brown and R. Q. Twiss, "A test of a new type of stellar interferometer on sirius," *Nature*, vol. 178, no. 4541, pp. 1046–1048, 1956.

[18] S. Butun, S. Tongay, and K. Aydin, "Enhanced light emission from large-area monolayer mos2 using plasmonic nanodisc arrays," *Nano letters*, vol. 15, no. 4, pp. 2700–2704, 2015.

[19] T. Cao, G. Wang, W. Han, H. Ye, C. Zhu, J. Shi, Q. Niu, P. Tan, E. Wang, B. Liu *et al.*, "Valley-selective circular dichroism of monolayer molybdenum disulphide," *Nature communications*, vol. 3, no. 1, pp. 1–5, 2012.

[20] S. Castelletto, B. Johnson, V. Ivády, N. Stavrias, T. Umeda, A. Gali, and T. Ohshima, "A silicon carbide room-temperature single-photon source," *Nature materials*, vol. 13, no. 2, pp. 151–156, 2014.

[21] Y.-R. Chang, H.-Y. Lee, K. Chen, C.-C. Chang, D.-S. Tsai, C.-C. Fu, T.-S. Lim, Y.-K. Tzeng, C.-Y. Fang, C.-C. Han *et al.*, "Mass production and dynamic imaging of fluorescent nanodiamonds," *Nature nanotechnology*, vol. 3, no. 5, pp. 284–288, 2008.

[22] N. Chejanovsky, Y. Kim, A. Zappe, B. Stuhlhofer, T. Taniguchi, K. Watanabe, D. Dasari, A. Finkler, J. H. Smet, and J. Wrachtrup, "Quantum light in curved low dimensional hexagonal boron nitride systems," *Scientific reports*, vol. 7, no. 1, pp. 1–14, 2017.

[23] N. Chejanovsky, A. Mukherjee, Y. Kim, A. Denisenko, A. Finkler, T. Taniguchi, K. Watanabe, D. B. R. Dasari, J. H. Smet, and J. Wrachtrup, "Single spin resonance in a van der waals embedded paramagnetic defect," *arXiv preprint arXiv:1906.05903*, 2019.

[24] N. Chejanovsky, M. Rezai, F. Paolucci, Y. Kim, T. Rendler, W. Rouabeh, F. Favaro de Oliveira, P. Herlinger, A. Denisenko, S. Yang *et al.*, "Structural attributes and photodynamics of visible spectrum quantum emitters in hexagonal boron nitride," *Nano letters*, vol. 16, no. 11, pp. 7037–7045, 2016.

[25] H. Chen, S. Nanz, A. Abass, J. Yan, T. Gao, D.-Y. Choi, Y. S. Kivshar, C. Rockstuhl, and D. N. Neshev, "Enhanced directional emission from monolayer wse2 integrated onto a multiresonant silicon-based photonic structure," *ACS Photonics*, vol. 4, no. 12, pp. 3031–3038, 2017.

[26] G. Cheng, Y. Zhang, L. Yan, H. Huang, Q. Huang, Y. Song, Y. Chen, and Z. Tang, "A paramagnetic neutral cbvn center in hexagonal boron nitride monolayer for spin qubit application," *Computational Materials Science*, vol. 129, pp. 247–251, 2017.

[27] S. Choi, T. T. Tran, C. Elbadawi, C. Lobo, X. Wang, S. Juodkazis, G. Seniutinas, M. Toth, and I. Aharonovich, "Engineering and localization of quantum emitters in large hexagonal boron nitride layers," *ACS applied materials & interfaces*, vol. 8, no. 43, pp. 29 642–29 648, 2016.

[28] J. Comtet, E. Glushkov, V. Navikas, J. Feng, V. Babenko, S. Hofmann, K. Watanabe, T. Taniguchi, and A. Radenovic, "Wide-field spectral super-resolution mapping of optically active defects in hexagonal boron nitride," *Nano letters*, vol. 19, no. 4, pp. 2516–2523, 2019.

[29] J. Comtet, B. Grosjean, E. Glushkov, A. Avsar, K. Watanabe, T. Taniguchi,

R. Vuilleumier, M.-L. Bocquet, and A. Radenovic, "Direct observation of water mediated single proton transport between hbn surface defects," *arXiv preprint arXiv:1906.09019*, 2019.

[30] E. Courtade, M. Semina, M. Manca, M. Glazov, C. Robert, F. Cadiz, G. Wang, T. Taniguchi, K. Watanabe, M. Pierre *et al.*, "Charged excitons in monolayer wse 2: experiment and theory," *Physical Review B*, vol. 96, no. 8, p. 085302, 2017.

[31] M. Davanco, J. Liu, L. Sapienza, C.-Z. Zhang, J. V. D. M. Cardoso, V. Verma, R. Mirin, S. W. Nam, L. Liu, and K. Srinivasan, "Heterogeneous integration for on-chip quantum photonic circuits with single quantum dot devices," *Nature communications*, vol. 8, no. 1, pp. 1–12, 2017.

[32] P. Debye, "Interferenz von röntgenstrahlen und wärmebewegung," *Annalen der Physik*, vol. 348, no. 1, pp. 49–92, 1913.

[33] A. Dietrich, K. D. Jahnke, J. M. Binder, T. Teraji, J. Isoya, L. J. Rogers, and F. Jelezko, "Isotopically varying spectral features of silicon-vacancy in diamond," *New Journal of Physics*, vol. 16, no. 11, p. 113019, 2014.

[34] A. Dousse, J. Suffczyński, A. Beveratos, O. Krebs, A. Lemaître, I. Sagnes, J. Bloch, P. Voisin, and P. Senellart, "Ultrabright source of entangled photon pairs," *Nature*, vol. 466, no. 7303, pp. 217–220, 2010.

[35] S. Dufferwiel, S. Schwarz, F. Withers, A. Trichet, F. Li, M. Sich, O. Del Pozo-Zamudio, C. Clark, A. Nalitov, D. Solnyshkov *et al.*, "Exciton–polaritons in van der waals heterostructures embedded in tunable microcavities," *Nature communications*, vol. 6, no. 1, pp. 1–7, 2015.

[36] N. M. H. Duong, E. Glushkov, A. Chernev, V. Navikas, J. Comtet, M. A. P. Nguyen, M. Toth, A. Radenovic, T. T. Tran, and I. Aharonovich, "Facile

production of hexagonal boron nitride nanoparticles by cryogenic exfoliation," *Nano letters*, vol. 19, no. 8, pp. 5417–5422, 2019.

[37] N. M. H. Duong, Z.-Q. Xu, M. Kianinia, R. Su, Z. Liu, S. Kim, C. Bradac, T. T. Tran, Y. Wan, L.-J. Li *et al.*, "Enhanced emission from wse2 monolayers coupled to circular bragg gratings," *ACS Photonics*, vol. 5, no. 10, pp. 3950–3955, 2018.

[38] A. W. Elshaari, E. Buyukozer, I. E. Zadeh, T. Lettner, P. Zhao, E. Scholl, S. Gyger, M. E. Reimer, D. Dalacu, P. J. Poole *et al.*, "Strain-tunable quantum integrated photonics," *Nano letters*, vol. 18, no. 12, pp. 7969–7976, 2018.

[39] A. W. Elshaari, I. E. Zadeh, A. Fognini, M. E. Reimer, D. Dalacu, P. J. Poole, V. Zwiller, and K. D. Jöns, "On-chip single photon filtering and multiplexing in hybrid quantum photonic circuits," *Nature communications*, vol. 8, no. 1, pp. 1–8, 2017.

[40] R. E. Evans, M. K. Bhaskar, D. D. Sukachev, C. T. Nguyen, A. Sipahigil, M. J. Burek, B. Machielse, G. H. Zhang, A. S. Zibrov, E. Bielejec *et al.*, "Photon-mediated interactions between quantum emitters in a diamond nanocavity," *Science*, vol. 362, no. 6415, pp. 662–665, 2018.

[41] A. L. Exarhos, D. A. Hopper, R. R. Grote, A. Alkauskas, and L. C. Bassett, "Optical signatures of quantum emitters in suspended hexagonal boron nitride," *ACS nano*, vol. 11, no. 3, pp. 3328–3336, 2017.

[42] A. L. Exarhos, D. A. Hopper, R. N. Patel, M. W. Doherty, and L. C. Bassett, "Magnetic-field-dependent quantum emission in hexagonal boron nitride at room temperature," *Nature communications*, vol. 10, no. 1, pp. 1–8, 2019.

[43] J. Feng, H. Deschout, S. Caneva, S. Hofmann, I. Loncaric, P. Lazic, and A. Radenovic, "Imaging of optically active defects with nanometer resolution," *Nano letters*, vol. 18, no. 3, pp. 1739–1744, 2018.

[44] G. Fiori, F. Bonaccorso, G. Iannaccone, T. Palacios, D. Neumaier, A. Seabaugh, S. K. Banerjee, and L. Colombo, "Electronics based on two-dimensional materials," *Nature nanotechnology*, vol. 9, no. 10, p. 768, 2014.

[45] F. Flamini, N. Spagnolo, and F. Sciarrino, "Photonic quantum information processing: a review," *Reports on Progress in Physics*, vol. 82, no. 1, p. 016001, 2018.

[46] R. Frisenda, E. Navarro-Moratalla, P. Gant, D. P. De Lara, P. Jarillo-Herrero, R. V. Gorbachev, and A. Castellanos-Gomez, "Recent progress in the assembly of nanodevices and van der waals heterostructures by deterministic placement of 2d materials," *Chemical Society Reviews*, vol. 47, no. 1, pp. 53–68, 2018.

[47] X. Gan, Y. Gao, K. Fai Mak, X. Yao, R.-J. Shiue, A. Van Der Zande, M. E. Trusheim, F. Hatami, T. F. Heinz, J. Hone *et al.*, "Controlling the spontaneous emission rate of monolayer mos2 in a photonic crystal nanocavity," *Applied physics letters*, vol. 103, no. 18, p. 181119, 2013.

[48] A. K. Geim and I. V. Grigorieva, "Van der waals heterostructures," *Nature*, vol. 499, no. 7459, p. 419, 2013.

[49] C. Gerry, P. Knight, and P. Knight, *Introductory Quantum Optics*. Cambridge University Press, 2005. [Online]. Available: https://books.google.com.au/books?id=CgByyoBJJwgC

[50] T. Godde, D. Schmidt, J. Schmutzler, M. Aßmann, J. Debus, F. Withers, E. Alexeev, O. Del Pozo-Zamudio, O. Skrypka, K. Novoselov *et al.*, "Exciton and trion dynamics in atomically thin mose 2 and wse 2: Effect of localization," *Physical Review B*, vol. 94, no. 16, p. 165301, 2016.

[51] P. Gold, A. Thoma, S. Maier, S. Reitzenstein, C. Schneider, S. Höfling, and M. Kamp, "Two-photon interference from remote quantum dots with inhomogeneously broadened linewidths," *Physical Review B*, vol. 89, no. 3, p. 035313, 2014.

[52] A. Gottscholl, M. Kianinia, V. Soltamov, S. Orlinskii, G. Mamin, C. Bradac, C. Kasper, K. Krambrock, A. Sperlich, M. Toth *et al.*, "Initialization and read-out of intrinsic spin defects in a van der waals crystal at room temperature," *Nature Materials*, pp. 1–6, 2020.

[53] J. B. Grimm, A. K. Muthusamy, Y. Liang, T. A. Brown, W. C. Lemon, R. Patel, R. Lu, J. J. Macklin, P. J. Keller, N. Ji *et al.*, "A general method to fine-tune fluorophores for live-cell and in vivo imaging," *Nature methods*, vol. 14, no. 10, p. 987, 2017.

[54] G. Grosso, H. Moon, B. Lienhard, S. Ali, D. K. Efetov, M. M. Furchi, P. Jarillo-Herrero, M. J. Ford, I. Aharonovich, and D. Englund, "Tunable and high-purity room temperature single-photon emission from atomic defects in hexagonal boron nitride," *Nature communications*, vol. 8, no. 1, pp. 1–8, 2017.

[55] C. Han and J. Ye, "Polarized resonant emission of monolayer ws 2 coupled with plasmonic sawtooth nanoslit array," *Nature communications*, vol. 11, no. 1, pp. 1–9, 2020.

[56] D. A. Hanifi, N. D. Bronstein, B. A. Koscher, Z. Nett, J. K. Swabeck,

K. Takano, A. M. Schwartzberg, L. Maserati, K. Vandewal, Y. van de Burgt *et al.*, "Redefining near-unity luminescence in quantum dots with photothermal threshold quantum yield," *Science*, vol. 363, no. 6432, pp. 1199–1202, 2019.

[57] B. J. Hausmann, B. Shields, Q. Quan, P. Maletinsky, M. McCutcheon, J. T. Choy, T. M. Babinec, A. Kubanek, A. Yacoby, M. D. Lukin *et al.*, "Integrated diamond networks for quantum nanophotonics," *Nano letters*, vol. 12, no. 3, pp. 1578–1582, 2012.

[58] K. He, N. Kumar, L. Zhao, Z. Wang, K. F. Mak, H. Zhao, and J. Shan, "Tightly bound excitons in monolayer wse 2," *Physical review letters*, vol. 113, no. 2, p. 026803, 2014.

[59] Y.-M. He, G. Clark, J. R. Schaibley, Y. He, M.-C. Chen, Y.-J. Wei, X. Ding, Q. Zhang, W. Yao, X. Xu *et al.*, "Single quantum emitters in monolayer semiconductors," *Nature nanotechnology*, vol. 10, no. 6, p. 497, 2015.

[60] D. Ho, C.-H. K. Wang, and E. K.-H. Chow, "Nanodiamonds: The intersection of nanotechnology, drug development, and personalized medicine," *Science Advances*, vol. 1, no. 7, p. e1500439, 2015.

[61] L. Horvath, A. Magrez, D. Golberg, C. Zhi, Y. Bando, R. Smajda, E. Horvath, L. Forro, and B. Schwaller, "In vitro investigation of the cellular toxicity of boron nitride nanotubes," *ACS nano*, vol. 5, no. 5, pp. 3800–3810, 2011.

[62] J. Huang, T. B. Hoang, and M. H. Mikkelsen, "Probing the origin of excitonic states in monolayer wse 2," *Scientific reports*, vol. 6, p. 22414, 2016.

[63] J.-K. Huang, J. Pu, C.-L. Hsu, M.-H. Chiu, Z.-Y. Juang, Y.-H. Chang, W.-H. Chang, Y. Iwasa, T. Takenobu, and L.-J. Li, "Large-area synthesis of

highly crystalline wse2 monolayers and device applications," *ACS nano*, vol. 8, no. 1, pp. 923–930, 2014.

[64] K. Huang and A. Rhys, "Theory of light absorption and non-radiative transitions in f-centres," in *Selected Papers Of Kun Huang: (With Commentary)*. World Scientific, 2000, pp. 74–92.

[65] T. Iwasaki, Y. Miyamoto, T. Taniguchi, P. Siyushev, M. H. Metsch, F. Jelezko, and M. Hatano, "Tin-vacancy quantum emitters in diamond," *Physical review letters*, vol. 119, no. 25, p. 253601, 2017.

[66] F. Jelezko and J. Wrachtrup, "Read-out of single spins by optical spectroscopy," *Journal of Physics: Condensed Matter*, vol. 16, no. 30, p. R1089, 2004.

[67] P. K. Jha, N. Shitrit, X. Ren, Y. Wang, and X. Zhang, "Spontaneous exciton valley coherence in transition metal dichalcogenide monolayers interfaced with an anisotropic metasurface," *Physical review letters*, vol. 121, no. 11, p. 116102, 2018.

[68] A. M. Jones, H. Yu, N. J. Ghimire, S. Wu, G. Aivazian, J. S. Ross, B. Zhao, J. Yan, D. G. Mandrus, D. Xiao *et al.*, "Optical generation of excitonic valley coherence in monolayer wse 2," *Nature nanotechnology*, vol. 8, no. 9, p. 634, 2013.

[69] N. R. Jungwirth, B. Calderon, Y. Ji, M. G. Spencer, M. E. Flatté, and G. D. Fuchs, "Temperature dependence of wavelength selectable zero-phonon emission from single defects in hexagonal boron nitride," *Nano letters*, vol. 16, no. 10, pp. 6052–6057, 2016.

[70] R. Katsumi, Y. Ota, A. Osada, T. Yamaguchi, T. Tajiri, M. Kakuda, S. Iwamoto, H. Akiyama, and Y. Arakawa, "Quantum-dot single-photon

source on a cmos silicon photonic chip integrated using transfer printing," *APL Photonics*, vol. 4, no. 3, p. 036105, 2019.

[71] A. Kawasuso, H. Itoh, T. Ohshima, K. Abe, and S. Okada, "Vacancy production by 3 mev electron irradiation in 6h-sic studied by positron lifetime spectroscopy," *Journal of applied physics*, vol. 82, no. 7, pp. 3232–3238, 1997.

[72] J. Kern, I. Niehues, P. Tonndorf, R. Schmidt, D. Wigger, R. Schneider, T. Stiehm, S. Michaelis de Vasconcellos, D. E. Reiter, T. Kuhn *et al.*, "Nanoscale positioning of single-photon emitters in atomically thin wse2," *Advanced materials*, vol. 28, no. 33, pp. 7101–7105, 2016.

[73] J. Kern, A. Trugler, I. Niehues, J. Ewering, R. Schmidt, R. Schneider, S. Najmaei, A. George, J. Zhang, J. Lou *et al.*, "Nanoantenna-enhanced light–matter interaction in atomically thin ws2," *Acs Photonics*, vol. 2, no. 9, pp. 1260–1265, 2015.

[74] S. Khasminskaya, F. Pyatkov, K. Slowik, S. Ferrari, O. Kahl, V. Kovalyuk, P. Rath, A. Vetter, F. Hennrich, M. M. Kappes *et al.*, "Fully integrated quantum photonic circuit with an electrically driven light source," *Nature Photonics*, vol. 10, no. 11, p. 727, 2016.

[75] J. B. Khurgin, "How to deal with the loss in plasmonics and metamaterials," *Nature nanotechnology*, vol. 10, no. 1, pp. 2–6, 2015.

[76] M. Kianinia, C. Bradac, B. Sontheimer, F. Wang, T. T. Tran, M. Nguyen, S. Kim, Z.-Q. Xu, D. Jin, A. W. Schell *et al.*, "All-optical control and super-resolution imaging of quantum emitters in layered materials," *Nature communications*, vol. 9, no. 1, pp. 1–8, 2018.

[77] M. Kianinia, B. Regan, S. A. Tawfik, T. T. Tran, M. J. Ford, I. Aharonovich, and M. Toth, "Robust solid-state quantum system operating at 800 k," *Acs Photonics*, vol. 4, no. 4, pp. 768–773, 2017.

[78] H. Kim, R. Bose, T. C. Shen, G. S. Solomon, and E. Waks, "A quantum logic gate between a solid-state quantum bit and a photon," *Nature Photonics*, vol. 7, no. 5, p. 373, 2013.

[79] J.-H. Kim, S. Aghaeimeibodi, C. J. Richardson, R. P. Leavitt, D. Englund, and E. Waks, "Hybrid integration of solid-state quantum emitters on a silicon photonic chip," *Nano letters*, vol. 17, no. 12, pp. 7394–7400, 2017.

[80] S. Kim, N. M. H. Duong, M. Nguyen, T.-J. Lu, M. Kianinia, N. Mendelson, A. Solntsev, C. Bradac, D. R. Englund, and I. Aharonovich, "Integrated on chip platform with quantum emitters in layered materials," *Advanced Optical Materials*, vol. 7, no. 23, p. 1901132, 2019.

[81] S. Kim, J. E. Fröch, J. Christian, M. Straw, J. Bishop, D. Totonjian, K. Watanabe, T. Taniguchi, M. Toth, and I. Aharonovich, "Photonic crystal cavities from hexagonal boron nitride," *Nature communications*, vol. 9, no. 1, p. 2623, 2018.

[82] M. Koperski, K. Nogajewski, A. Arora, V. Cherkez, P. Mallet, J.-Y. Veuillen, J. Marcus, P. Kossacki, and M. Potemski, "Single photon emitters in exfoliated wse 2 structures," *Nature nanotechnology*, vol. 10, no. 6, p. 503, 2015.

[83] M. Koperski, K. Nogajewski, and M. Potemski, "Single photon emitters in boron nitride: more than a supplementary material," *Optics Communications*, vol. 411, pp. 158–165, 2018.

[84] A. Kormanyos, V. Zolyomi, N. D. Drummond, P. Rakyta, G. Burkard, and V. I. Falko, "Monolayer mos 2: Trigonal warping, the γ valley, and spin-orbit coupling effects," *Physical review b*, vol. 88, no. 4, p. 045416, 2013.

[85] N. Kostoglou, K. Polychronopoulou, and C. Rebholz, "Thermal and chemical stability of hexagonal boron nitride (h-bn) nanoplatelets," *Vacuum*, vol. 112, pp. 42–45, 2015.

[86] C. Kurtsiefer, S. Mayer, P. Zarda, and H. Weinfurter, "Stable solid-state source of single photons," *Physical review letters*, vol. 85, no. 2, p. 290, 2000.

[87] B. Lee, J. Park, G. H. Han, H.-S. Ee, C. H. Naylor, W. Liu, A. C. Johnson, and R. Agarwal, "Fano resonance and spectrally modified photoluminescence enhancement in monolayer mos2 integrated with plasmonic nanoantenna array," *Nano letters*, vol. 15, no. 5, pp. 3646–3653, 2015.

[88] S.-Y. Lee, T.-Y. Jeong, S. Jung, and K.-J. Yee, "Refractive index dispersion of hexagonal boron nitride in the visible and near-infrared," *physica status solidi (b)*, vol. 256, no. 6, p. 1800417, 2019.

[89] G. N. Lewis, "The conservation of photons," *Nature*, vol. 118, no. 2981, p. 874, 1926.

[90] C. Li, Z.-Q. Xu, N. Mendelson, M. Kianinia, M. Toth, and I. Aharonovich, "Purification of single-photon emission from hbn using post-processing treatments," *Nanophotonics*, vol. 8, no. 11, pp. 2049–2055, 2019.

[91] X. Li, G. D. Shepard, A. Cupo, N. Camporeale, K. Shayan, Y. Luo, V. Meunier, and S. Strauf, "Nonmagnetic quantum emitters in boron nitride with ultranarrow and sideband-free emission spectra," *ACS nano*, vol. 11, no. 7, pp. 6652–6660, 2017.

[92] Y. Li, J. Zhang, D. Huang, H. Sun, F. Fan, J. Feng, Z. Wang, and C.-Z. Ning, "Room-temperature continuous-wave lasing from monolayer molybdenum ditelluride integrated with a silicon nanobeam cavity," *Nature nanotechnology*, vol. 12, no. 10, p. 987, 2017.

[93] J.-H. Liu, L. Cao, G. E. LeCroy, P. Wang, M. J. Meziani, Y. Dong, Y. Liu, P. G. Luo, and Y.-P. Sun, "Carbon "quantum" dots for fluorescence labeling of cells," *ACS applied materials & interfaces*, vol. 7, no. 34, pp. 19 439–19 445, 2015.

[94] X. Liu, C. Sun, B. Xiong, L. Wang, J. Wang, Y. Han, Z. Hao, H. Li, Y. Luo, J. Yan *et al.*, "Aluminum nitride-on-sapphire platform for integrated high-q microresonators," *Optics express*, vol. 25, no. 2, pp. 587–594, 2017.

[95] X. Liu, T. Galfsky, Z. Sun, F. Xia, E.-c. Lin, Y.-H. Lee, S. Kéna-Cohen, and V. M. Menon, "Strong light–matter coupling in two-dimensional atomic crystals," *Nature Photonics*, vol. 9, no. 1, p. 30, 2015.

[96] T.-J. Lu, M. Fanto, H. Choi, P. Thomas, J. Steidle, S. Mouradian, W. Kong, D. Zhu, H. Moon, K. Berggren *et al.*, "Aluminum nitride integrated photonics platform for the ultraviolet to visible spectrum," *Optics express*, vol. 26, no. 9, pp. 11 147–11 160, 2018.

[97] Y. Luo, G. D. Shepard, J. V. Ardelean, D. A. Rhodes, B. Kim, K. Barmak, J. C. Hone, and S. Strauf, "Deterministic coupling of site-controlled quantum emitters in monolayer wse 2 to plasmonic nanocavities," *Nature nanotechnology*, vol. 13, no. 12, pp. 1137–1142, 2018.

[98] K. F. Mak, K. He, C. Lee, G. H. Lee, J. Hone, T. F. Heinz, and J. Shan, "Tightly bound trions in monolayer mos 2," *Nature materials*, vol. 12, no. 3, pp. 207–211, 2013.

[99] K. F. Mak, C. Lee, J. Hone, J. Shan, and T. F. Heinz, "Atomically thin mos 2: a new direct-gap semiconductor," *Physical review letters*, vol. 105, no. 13, p. 136805, 2010.

[100] K. F. Mak, K. L. McGill, J. Park, and P. L. McEuen, "The valley hall effect in mos2 transistors," *Science*, vol. 344, no. 6191, pp. 1489–1492, 2014.

[101] K. F. Mak and J. Shan, "Photonics and optoelectronics of 2d semiconductor transition metal dichalcogenides," *Nature Photonics*, vol. 10, no. 4, p. 216, 2016.

[102] L. Martínez, T. Pelini, V. Waselowski, J. Maze, B. Gil, G. Cassabois, and V. Jacques, "Efficient single photon emission from a high-purity hexagonal boron nitride crystal," *Physical Review B*, vol. 94, no. 12, p. 121405, 2016.

[103] L. Mattheiss, "Band structures of transition-metal-dichalcogenide layer compounds," *Physical Review B*, vol. 8, no. 8, p. 3719, 1973.

[104] K. M. McCreary, M. Currie, A. T. Hanbicki, H.-J. Chuang, and B. T. Jonker, "Understanding variations in circularly polarized photoluminescence in monolayer transition metal dichalcogenides," *ACS nano*, vol. 11, no. 8, pp. 7988–7994, 2017.

[105] N. Mendelson, M. Toth, I. Aharonovich, and T. T. Tran, "Strain engineering of quantum emitters in hexagonal boron nitride," *arXiv preprint arXiv:1911.08072*, 2019.

[106] N. Mendelson, Z.-Q. Xu, T. T. Tran, M. Kianinia, J. Scott, C. Bradac, I. Aharonovich, and M. Toth, "Engineering and tuning of quantum emitters in few-layer hexagonal boron nitride," *ACS nano*, vol. 13, no. 3, pp. 3132–3140, 2019.

[107] A. Merlo, V. R. S. S. Mokkapati, S. Pandit, and I. Mijakovic, "Boron nitride nanomaterials: biocompatibility and bio-applications," *Biomaterials science*, vol. 6, no. 9, pp. 2298–2311, 2018.

[108] P. Meystre and M. Sargent, *Elements of quantum optics*. Springer Science & Business Media, 2007.

[109] P. Michler, A. Kiraz, C. Becher, W. Schoenfeld, P. Petroff, L. Zhang, E. Hu, and A. Imamoglu, "A quantum dot single-photon turnstile device," *science*, vol. 290, no. 5500, pp. 2282–2285, 2000.

[110] N. Mizuochi, P. Neumann, F. Rempp, J. Beck, V. Jacques, P. Siyushev, K. Nakamura, D. Twitchen, H. Watanabe, S. Yamasaki *et al.*, "Coherence of single spins coupled to a nuclear spin bath of varying density," *Physical review B*, vol. 80, no. 4, p. 041201, 2009.

[111] S. Molesky, Z. Lin, A. Y. Piggott, W. Jin, J. Vucković, and A. W. Rodriguez, "Inverse design in nanophotonics," *Nature Photonics*, vol. 12, no. 11, pp. 659–670, 2018.

[112] A. Molina-Sánchez, D. Sangalli, L. Wirtz, and A. Marini, "Ab initio calculations of ultrashort carrier dynamics in two-dimensional materials: valley depolarization in single-layer wse2," *Nano letters*, vol. 17, no. 8, pp. 4549–4555, 2017.

[113] E. Moreau, I. Robert, J. Gérard, I. Abram, L. Manin, and V. Thierry-Mieg, "Single-mode solid-state single photon source based on isolated quantum dots in pillar microcavities," *Applied Physics Letters*, vol. 79, no. 18, pp. 2865–2867, 2001.

[114] P. Mrowinski, P. Schnauber, P. Gutsche, A. Kaganskiy, J. Schall, S. Burger, S. Rodt, and S. Reitzenstein, "Directional emission of a deterministically

fabricated quantum dot–bragg reflection multimode waveguide system," *ACS Photonics*, vol. 6, no. 9, pp. 2231–2237, 2019.

[115] L. Museur, E. Feldbach, and A. Kanaev, "Defect-related photoluminescence of hexagonal boron nitride," *Physical Review B*, vol. 78, no. 15, p. 155204, 2008.

[116] R. Nagy, M. Widmann, M. Niethammer, D. B. Dasari, I. Gerhardt, Ö. O. Soykal, M. Radulaski, T. Ohshima, J. Vučković, N. T. Son *et al.*, "Quantum properties of dichroic silicon vacancies in silicon carbide," *Physical Review Applied*, vol. 9, no. 3, p. 034022, 2018.

[117] E. Neu, D. Steinmetz, J. Riedrich-Möller, S. Gsell, M. Fischer, M. Schreck, and C. Becher, "Single photon emission from silicon-vacancy colour centres in chemical vapour deposition nano-diamonds on iridium," *New Journal of Physics*, vol. 13, no. 2, p. 025012, 2011.

[118] H. Ngoc My Duong, M. A. P. Nguyen, M. Kianinia, T. Ohshima, H. Abe, K. Watanabe, T. Taniguchi, J. H. Edgar, I. Aharonovich, and M. Toth, "Effects of high-energy electron irradiation on quantum emitters in hexagonal boron nitride," *ACS applied materials & interfaces*, vol. 10, no. 29, pp. 24 886–24 891, 2018.

[119] N. Nikolay, N. Mendelson, N. Sadzak, F. Böhm, T. T. Tran, B. Sontheimer, I. Aharonovich, and O. Benson, "Very large and reversible stark-shift tuning of single emitters in layered hexagonal boron nitride," *Physical Review Applied*, vol. 11, no. 4, p. 041001, 2019.

[120] G. Noh, D. Choi, J.-H. Kim, D.-G. Im, Y.-H. Kim, H. Seo, and J. Lee, "Stark tuning of single-photon emitters in hexagonal boron nitride," *Nano letters*, vol. 18, no. 8, pp. 4710–4715, 2018.

[121] K. S. Novoselov, A. K. Geim, S. Morozov, D. Jiang, M. I. Katsnelson, I. Grigorieva, S. Dubonos, Firsov, and AA, "Two-dimensional gas of massless dirac fermions in graphene," *nature*, vol. 438, no. 7065, pp. 197–200, 2005.

[122] A. Osada, Y. Ota, R. Katsumi, M. Kakuda, S. Iwamoto, and Y. Arakawa, "Strongly coupled single-quantum-dot–cavity system integrated on a cmos-processed silicon photonic chip," *Physical Review Applied*, vol. 11, no. 2, p. 024071, 2019.

[123] C. I. Osorio, T. Coenen, B. J. Brenny, A. Polman, and A. F. Koenderink, "Angle-resolved cathodoluminescence imaging polarimetry," *ACS Photonics*, vol. 3, no. 1, pp. 147–154, 2016.

[124] C. I. Osorio, A. Mohtashami, and A. F. Koenderink, "K-space polarimetry of bullseye plasmon antennas," *Scientific reports*, vol. 5, p. 9966, 2015.

[125] E. Palacios, S. Park, S. Butun, L. Lauhon, and K. Aydin, "Enhanced radiative emission from monolayer mos2 films using a single plasmonic dimer nanoantenna," *Applied Physics Letters*, vol. 111, no. 3, p. 031101, 2017.

[126] Y. E. Panfil, M. Oded, and U. Banin, "Colloidal quantum nanostructures: emerging materials for display applications," *Angewandte Chemie International Edition*, vol. 57, no. 16, pp. 4274–4295, 2018.

[127] Paszkowicz, "Lattice parameters and anisotropic thermal expansion of hexagonal boron nitride in the 10–297.5 k temperature range," *Applied Physics A*, vol. 75, no. 3, pp. 431–435, 2002.

[128] F. Peyskens, C. Chakraborty, M. Muneeb, D. Van Thourhout, and D. Englund, "Integration of single photon emitters in 2d layered materials with a silicon nitride photonic chip," *Nature communications*, vol. 10, no. 1, pp. 1–7, 2019.

[129] N. V. Proscia, Z. Shotan, H. Jayakumar, P. Reddy, C. Cohen, M. Dollar, A. Alkauskas, M. Doherty, C. A. Meriles, and V. M. Menon, "Near-deterministic activation of room-temperature quantum emitters in hexagonal boron nitride," *Optica*, vol. 5, no. 9, pp. 1128–1134, 2018.

[130] E. M. Purcell, "Spontaneous emission probabilities at radio frequencies," in *Confined Electrons and Photons*. Springer, 1995, pp. 839–839.

[131] Y. Rah, Y. Jin, S. Kim, and K. Yu, "Optical analysis of the refractive index and birefringence of hexagonal boron nitride from the visible to near-infrared," *Optics letters*, vol. 44, no. 15, pp. 3797–3800, 2019.

[132] M. Reed, J. Randall, R. Aggarwal, R. Matyi, T. Moore, and A. Wetsel, "Observation of discrete electronic states in a zero-dimensional semiconductor nanostructure," *Physical Review Letters*, vol. 60, no. 6, p. 535, 1988.

[133] J. R. Reimers, A. Sajid, R. Kobayashi, and M. J. Ford, "Understanding and calibrating density-functional-theory calculations describing the energy and spectroscopy of defect sites in hexagonal boron nitride," *Journal of chemical theory and computation*, vol. 14, no. 3, pp. 1602–1613, 2018.

[134] L. J. Rogers, K. D. Jahnke, M. H. Metsch, A. Sipahigil, J. M. Binder, T. Teraji, H. Sumiya, J. Isoya, M. D. Lukin, P. Hemmer *et al.*, "All-optical initialization, readout, and coherent preparation of single silicon-vacancy spins in diamond," *Physical review letters*, vol. 113, no. 26, p. 263602, 2014.

[135] J. S. Ross, P. Klement, A. M. Jones, N. J. Ghimire, J. Yan, D. Mandrus, T. Taniguchi, K. Watanabe, K. Kitamura, W. Yao *et al.*, "Electrically tunable excitonic light-emitting diodes based on monolayer wse 2 p–n junctions," *Nature nanotechnology*, vol. 9, no. 4, p. 268, 2014.

[136] J. S. Ross, S. Wu, H. Yu, N. J. Ghimire, A. M. Jones, G. Aivazian, J. Yan, D. G. Mandrus, D. Xiao, W. Yao *et al.*, "Electrical control of neutral and charged excitons in a monolayer semiconductor," *Nature communications*, vol. 4, no. 1, pp. 1–6, 2013.

[137] J. Sakurai, "Modern quantum mechanics; tuan, sf, ed," 1985.

[138] O. Salehzadeh, M. Djavid, N. H. Tran, I. Shih, and Z. Mi, "Optically pumped two-dimensional mos2 lasers operating at room-temperature," *Nano letters*, vol. 15, no. 8, pp. 5302–5306, 2015.

[139] C. Santori, D. Fattal, M. Pelton, G. S. Solomon, and Y. Yamamoto, "Polarization-correlated photon pairs from a single quantum dot," *Physical Review B*, vol. 66, no. 4, p. 045308, 2002.

[140] C. Santori, D. Fattal, J. Vučković, G. S. Solomon, and Y. Yamamoto, "Indistinguishable photons from a single-photon device," *nature*, vol. 419, no. 6907, pp. 594–597, 2002.

[141] J. R. Schaibley, H. Yu, G. Clark, P. Rivera, J. S. Ross, K. L. Seyler, W. Yao, and X. Xu, "Valleytronics in 2d materials," *Nature Reviews Materials*, vol. 1, no. 11, pp. 1–15, 2016.

[142] A. W. Schell, H. Takashima, T. T. Tran, I. Aharonovich, and S. Takeuchi, "Coupling quantum emitters in 2d materials with tapered fibers," *ACS Photonics*, vol. 4, no. 4, pp. 761–767, 2017.

[143] M. L. Schipper, G. Iyer, A. L. Koh, Z. Cheng, Y. Ebenstein, A. Aharoni, S. Keren, L. A. Bentolila, J. Li, J. Rao *et al.*, "Particle size, surface coating, and pegylation influence the biodistribution of quantum dots in living mice," *Small*, vol. 5, no. 1, pp. 126–134, 2009.

[144] P. Senellart, G. Solomon, and A. White, "High-performance semiconductor quantum-dot single-photon sources," *Nature nanotechnology*, vol. 12, no. 11, p. 1026, 2017.

[145] Z. Shotan, H. Jayakumar, C. R. Considine, M. Mackoit, H. Fedder, J. Wrachtrup, A. Alkauskas, M. W. Doherty, V. M. Menon, and C. A. Meriles, "Photoinduced modification of single-photon emitters in hexagonal boron nitride," *ACS Photonics*, vol. 3, no. 12, pp. 2490–2496, 2016.

[146] C. Simon, H. De Riedmatten, M. Afzelius, N. Sangouard, H. Zbinden, and N. Gisin, "Quantum repeaters with photon pair sources and multimode memories," *Physical review letters*, vol. 98, no. 19, p. 190503, 2007.

[147] A. Singh, Q. Li, S. Liu, Y. Yu, X. Lu, C. Schneider, S. Höfling, J. Lawall, V. Verma, R. Mirin *et al.*, "Quantum frequency conversion of a quantum dot single-photon source on a nanophotonic chip," *Optica*, vol. 6, no. 5, pp. 563–569, 2019.

[148] A. Sipahigil, R. E. Evans, D. D. Sukachev, M. J. Burek, J. Borregaard, M. K. Bhaskar, C. T. Nguyen, J. L. Pacheco, H. A. Atikian, C. Meuwly *et al.*, "An integrated diamond nanophotonics platform for quantum-optical networks," *Science*, vol. 354, no. 6314, pp. 847–850, 2016.

[149] B. Sontheimer, M. Braun, N. Nikolay, N. Sadzak, I. Aharonovich, and O. Benson, "Photodynamics of quantum emitters in hexagonal boron nitride revealed by low-temperature spectroscopy," *Physical Review B*, vol. 96, no. 12, p. 121202, 2017.

[150] A. Splendiani, L. Sun, Y. Zhang, T. Li, J. Kim, C.-Y. Chim, G. Galli, and F. Wang, "Emerging photoluminescence in monolayer mos2," *Nano letters*, vol. 10, no. 4, pp. 1271–1275, 2010.

[151] N. Srocka, A. Musiał, P.-I. Schneider, P. Mrowiński, P. Holewa, S. Burger, D. Quandt, A. Strittmatter, S. Rodt, S. Reitzenstein *et al.*, "Enhanced photon-extraction efficiency from ingaas/gaas quantum dots in deterministic photonic structures at 1.3 μ m fabricated by in-situ electron-beam lithography," *AIP Advances*, vol. 8, no. 8, p. 085205, 2018.

[152] P. Steinleitner, P. Merkl, P. Nagler, J. Mornhinweg, C. Schuller, T. Korn, A. Chernikov, and R. Huber, "Direct observation of ultrafast exciton formation in a monolayer of wse2," *Nano Letters*, vol. 17, no. 3, pp. 1455–1460, 2017.

[153] H. L. Stern, R. Wang, Y. Fan, R. Mizuta, J. C. Stewart, L.-M. Needham, T. D. Roberts, R. Wai, N. S. Ginsberg, D. Klenerman *et al.*, "Spectrally resolved photodynamics of individual emitters in large-area monolayers of hexagonal boron nitride," *ACS nano*, vol. 13, no. 4, pp. 4538–4547, 2019.

[154] M. Y. Su and R. P. Mirin, "Enhanced light extraction from circular bragg grating coupled microcavities," *Applied physics letters*, vol. 89, no. 3, p. 033105, 2006.

[155] P. Tamarat, T. Gaebel, J. Rabeau, M. Khan, A. Greentree, H. Wilson, L. Hollenberg, S. Prawer, P. Hemmer, F. Jelezko *et al.*, "Stark shift control of single optical centers in diamond," *Physical review letters*, vol. 97, no. 8, p. 083002, 2006.

[156] S. A. Tawfik, S. Ali, M. Fronzi, M. Kianinia, T. T. Tran, C. Stampfl, I. Aharonovich, M. Toth, and M. J. Ford, "First-principles investigation of quantum emission from hbn defects," *Nanoscale*, vol. 9, no. 36, pp. 13 575–13 582, 2017.

[157] S. D. Tchernij, T. Herzig, J. Forneris, J. Kupper, S. Pezzagna, P. Traina,

E. Moreva, I. Degiovanni, G. Brida, N. Skukan *et al.*, "Single-photon-emitting optical centers in diamond fabricated upon sn implantation," *ACS photonics*, vol. 4, no. 10, pp. 2580–2586, 2017.

[158] J. Toledo, D. De Jesus, M. Kianinia, A. Leal, C. Fantini, L. Cury, G. Sáfar, I. Aharonovich, and K. Krambrock, "Electron paramagnetic resonance signature of point defects in neutron-irradiated hexagonal boron nitride," *Physical Review B*, vol. 98, no. 15, p. 155203, 2018.

[159] S. Tongay, J. Zhou, C. Ataca, J. Liu, J. S. Kang, T. S. Matthews, L. You, J. Li, J. C. Grossman, and J. Wu, "Broad-range modulation of light emission in two-dimensional semiconductors by molecular physisorption gating," *Nano letters*, vol. 13, no. 6, pp. 2831–2836, 2013.

[160] P. Tonndorf, O. Del Pozo-Zamudio, N. Gruhler, J. Kern, R. Schmidt, A. I. Dmitriev, A. P. Bakhtinov, A. I. Tartakovskii, W. Pernice, S. Michaelis de Vasconcellos *et al.*, "On-chip waveguide coupling of a layered semiconductor single-photon source," *Nano letters*, vol. 17, no. 9, pp. 5446–5451, 2017.

[161] P. Tonndorf, S. Schwarz, J. Kern, I. Niehues, O. Del Pozo-Zamudio, A. I. Dmitriev, A. P. Bakhtinov, D. N. Borisenko, N. N. Kolesnikov, A. I. Tartakovskii *et al.*, "Single-photon emitters in gase," *2D Materials*, vol. 4, no. 2, p. 021010, 2017.

[162] M. Toth and I. Aharonovich, "Single photon sources in atomically thin materials," *Annual review of physical chemistry*, vol. 70, pp. 123–142, 2019.

[163] T. T. Tran, K. Bray, M. J. Ford, M. Toth, and I. Aharonovich, "Quantum emission from hexagonal boron nitride monolayers," *Nature nanotechnology*, vol. 11, no. 1, p. 37, 2016.

[164] T. T. Tran, C. Elbadawi, D. Totonjian, C. J. Lobo, G. Grosso, H. Moon, D. R. Englund, M. J. Ford, I. Aharonovich, and M. Toth, "Robust multicolor single photon emission from point defects in hexagonal boron nitride," *ACS nano*, vol. 10, no. 8, p. 73317338, 2016.

[165] T. T. Tran, D. Wang, Z.-Q. Xu, A. Yang, M. Toth, T. W. Odom, and I. Aharonovich, "Deterministic coupling of quantum emitters in 2d materials to plasmonic nanocavity arrays," *Nano letters*, vol. 17, no. 4, pp. 2634–2639, 2017.

[166] T. T. Tran, C. Zachreson, A. M. Berhane, K. Bray, R. G. Sandstrom, L. H. Li, T. Taniguchi, K. Watanabe, I. Aharonovich, and M. Toth, "Quantum emission from defects in single-crystalline hexagonal boron nitride," *Physical review applied*, vol. 5, no. 3, p. 034005, 2016.

[167] P. Turschmann, N. Rotenberg, J. Renger, I. Harder, O. Lohse, T. Utikal, S. Gotzinger, and V. Sandoghdar, "Chip-based all-optical control of single molecules coherently coupled to a nanoguide," *Nano letters*, vol. 17, no. 8, pp. 4941–4945, 2017.

[168] M. M. Ugeda, A. J. Bradley, S.-F. Shi, H. Felipe, Y. Zhang, D. Y. Qiu, W. Ruan, S.-K. Mo, Z. Hussain, Z.-X. Shen *et al.*, "Giant bandgap renormalization and excitonic effects in a monolayer transition metal dichalcogenide semiconductor," *Nature materials*, vol. 13, no. 12, pp. 1091–1095, 2014.

[169] A. Valizadeh, H. Mikaeili, M. Samiei, S. M. Farkhani, N. Zarghami, A. Akbarzadeh, S. Davaran *et al.*, "Quantum dots: synthesis, bioapplications, and toxicity," *Nanoscale research letters*, vol. 7, no. 1, p. 480, 2012.

[170] E. van Oort, N. Manson, and M. Glasbeek, "Optically detected spin

coherence of the diamond nv centre in its triplet ground state," *Journal of Physics C: Solid State Physics*, vol. 21, no. 23, p. 4385, 1988.

[171] I. I. Vlasov, A. A. Shiryaev, T. Rendler, S. Steinert, S.-Y. Lee, D. Antonov, M. Vörös, F. Jelezko, A. V. Fisenko, L. F. Semjonova *et al.*, "Molecular-sized fluorescent nanodiamonds," *Nature nanotechnology*, vol. 9, no. 1, pp. 54–58, 2014.

[172] T. Vogl, M. W. Doherty, B. C. Buchler, Y. Lu, and P. K. Lam, "Atomic localization of quantum emitters in multilayer hexagonal boron nitride," *arXiv preprint arXiv:1904.06852*, 2019.

[173] D. F. Walls and G. J. Milburn, *Quantum optics*. Springer Science & Business Media, 2007.

[174] J. Wang, S. Paesani, Y. Ding, R. Santagati, P. Skrzypczyk, A. Salavrakos, J. Tura, R. Augusiak, L. Mančinska, D. Bacco *et al.*, "Multidimensional quantum entanglement with large-scale integrated optics," *Science*, vol. 360, no. 6386, pp. 285–291, 2018.

[175] Q. Wang, Q. Zhang, X. Zhao, X. Luo, C. P. Y. Wong, J. Wang, D. Wan, T. Venkatesan, S. J. Pennycook, K. P. Loh *et al.*, "Photoluminescence upconversion by defects in hexagonal boron nitride," *Nano letters*, vol. 18, no. 11, pp. 6898–6905, 2018.

[176] Y. Wang, Y. Liu, J. Zhang, J. Wu, H. Xu, X. Wen, X. Zhang, C. S. Tiwary, W. Yang, R. Vajtai *et al.*, "Cryo-mediated exfoliation and fracturing of layered materials into 2d quantum dots," *Science advances*, vol. 3, no. 12, p. e1701500, 2017.

[177] K. Watanabe, T. Taniguchi, and H. Kanda, "Direct-bandgap properties and

evidence for ultraviolet lasing of hexagonal boron nitride single crystal," *Nature materials*, vol. 3, no. 6, p. 404, 2004.

[178] S. Wehner, D. Elkouss, and R. Hanson, "Quantum internet: A vision for the road ahead," *Science*, vol. 362, no. 6412, p. eaam9288, 2018.

[179] D. White, A. Branny, R. J. Chapman, R. Picard, M. Brotons-Gisbert, A. Boes, A. Peruzzo, C. Bonato, and B. D. Gerardot, "Atomically-thin quantum dots integrated with lithium niobate photonic chips," *Optical Materials Express*, vol. 9, no. 2, pp. 441–448, 2019.

[180] O. S. Wolfbeis, "An overview of nanoparticles commonly used in fluorescent bioimaging," *Chemical Society Reviews*, vol. 44, no. 14, pp. 4743–4768, 2015.

[181] S. Wu, S. Buckley, A. M. Jones, J. S. Ross, N. J. Ghimire, J. Yan, D. G. Mandrus, W. Yao, F. Hatami, J. Vučković *et al.*, "Control of two-dimensional excitonic light emission via photonic crystal," *2D Materials*, vol. 1, no. 1, p. 011001, 2014.

[182] S. Wu, S. Buckley, J. R. Schaibley, L. Feng, J. Yan, D. G. Mandrus, F. Hatami, W. Yao, J. Vučković, A. Majumdar *et al.*, "Monolayer semiconductor nanocavity lasers with ultralow thresholds," *Nature*, vol. 520, no. 7545, pp. 69–72, 2015.

[183] S. Wu, J. S. Ross, G.-B. Liu, G. Aivazian, A. Jones, Z. Fei, W. Zhu, D. Xiao, W. Yao, D. Cobden *et al.*, "Electrical tuning of valley magnetic moment through symmetry control in bilayer mos 2," *Nature Physics*, vol. 9, no. 3, pp. 149–153, 2013.

[184] Y. Xia, Q. Li, J. Kim, W. Bao, C. Gong, S. Yang, Y. Wang, and X. Zhang, "Room-temperature giant stark effect of single photon emitter in van der waals material," *Nano letters*, vol. 19, no. 10, pp. 7100–7105, 2019.

[185] Z.-Q. Xu, C. Elbadawi, T. T. Tran, M. Kianinia, X. Li, D. Liu, T. B. Hoffman, M. Nguyen, S. Kim, J. H. Edgar *et al.*, "Single photon emission from plasma treated 2d hexagonal boron nitride," *Nanoscale*, vol. 10, no. 17, pp. 7957–7965, 2018.

[186] Z.-Q. Xu, Y. Zhang, S. Lin, C. Zheng, Y. L. Zhong, X. Xia, Z. Li, P. J. Sophia, M. S. Fuhrer, Y.-B. Cheng *et al.*, "Synthesis and transfer of large-area monolayer ws2 crystals: moving toward the recyclable use of sapphire substrates," *ACS nano*, vol. 9, no. 6, pp. 6178–6187, 2015.

[187] Z.-Q. Xu, Y. Zhang, Z. Wang, Y. Shen, W. Huang, X. Xia, W. Yu, Y. Xue, L. Sun, C. Zheng *et al.*, "Atomically thin lateral p–n junction photodetector with large effective detection area," *2D Materials*, vol. 3, no. 4, p. 041001, 2016.

[188] T. Yan, X. Qiao, X. Liu, P. Tan, and X. Zhang, "Photoluminescence properties and exciton dynamics in monolayer wse2," *Applied Physics Letters*, vol. 105, no. 10, p. 101901, 2014.

[189] Y. Ye, Z. J. Wong, X. Lu, X. Ni, H. Zhu, X. Chen, Y. Wang, and X. Zhang, "Monolayer excitonic laser," *Nature Photonics*, vol. 9, no. 11, pp. 733–737, 2015.

[190] H. Yuan, M. S. Bahramy, K. Morimoto, S. Wu, K. Nomura, B.-J. Yang, H. Shimotani, R. Suzuki, M. Toh, C. Kloc *et al.*, "Zeeman-type spin splitting controlled by an electric field," *Nature Physics*, vol. 9, no. 9, pp. 563–569, 2013.

[191] H. Zeng, J. Dai, W. Yao, D. Xiao, and X. Cui, "Valley polarization in mos 2 monolayers by optical pumping," *Nature nanotechnology*, vol. 7, no. 8, pp. 490–493, 2012.

[192] C. Zhang, H. Yuan, N. Zhang, L. Xu, B. Li, G. Cheng, Y. Wang, Q. Gui, and J. Fang, "Dependence of high density nitrogen-vacancy center ensemble coherence on electron irradiation doses and annealing time," *Journal of Physics D: Applied Physics*, vol. 50, no. 50, p. 505104, 2017.

[193] J. Zhang, F. Cheng, J. Li, J.-J. Zhu, and Y. Lu, "Fluorescent nanoprobes for sensing and imaging of metal ions: Recent advances and future perspectives," *Nano today*, vol. 11, no. 3, pp. 309–329, 2016.

[194] Y. Zhang, T.-R. Chang, B. Zhou, Y.-T. Cui, H. Yan, Z. Liu, F. Schmitt, J. Lee, R. Moore, Y. Chen *et al.*, "Direct observation of the transition from indirect to direct bandgap in atomically thin epitaxial mose 2," *Nature nanotechnology*, vol. 9, no. 2, p. 111, 2014.

[195] Y. Zhang, T. Oka, R. Suzuki, J. Ye, and Y. Iwasa, "Electrically switchable chiral light-emitting transistor," *Science*, vol. 344, no. 6185, pp. 725–728, 2014.

[196] Y. Zhang, Y.-W. Tan, H. L. Stormer, and P. Kim, "Experimental observation of the quantum hall effect and berry's phase in graphene," *nature*, vol. 438, no. 7065, pp. 201–204, 2005.

[197] W. Zhao, Z. Ghorannevis, L. Chu, M. Toh, C. Kloc, P.-H. Tan, and G. Eda, "Evolution of electronic structure in atomically thin sheets of ws2 and wse2," *ACS nano*, vol. 7, no. 1, pp. 791–797, 2013.

[198] W. Zhao, R. M. Ribeiro, M. Toh, A. Carvalho, C. Kloc, A. Castro Neto, and G. Eda, "Origin of indirect optical transitions in few-layer mos2, ws2, and wse2," *Nano Letters*, vol. 13, no. 11, pp. 5627–5634, 2013.

[199] Z. Zhu, Y. Cheng, and U. Schwingenschlögl, "Giant spin-orbit-induced spin

splitting in two-dimensional transition-metal dichalcogenide semiconductors," *Physical Review B*, vol. 84, no. 15, p. 153402, 2011.

[200] J. Ziegler, A. Blaikie, A. Fathalizadeh, D. Miller, F. S. Yasin, K. Williams, J. Mohrhardt, B. J. McMorran, A. Zettl, and B. Aleman, "Single-photon emitters in boron nitride nanococoons," *Nano letters*, vol. 18, no. 4, pp. 2683–2688, 2018.